EVALUATION OF A PROTOTYPE SERIES-COMPLIENT HOPPING LEG FOR BIPED ROBOT APPLICATIONS

Undergraduate Honors Thesis

By

Brian Thomas Knox

* * * * *

The Ohio State University
Department of Mechanical Engineering
2007

Undergraduate Honors Research
Examination Committee Approval:

James P. Schmiedeler

Dr. James P. Schmiedeler, Advisor

ABSTRACT

Biped robots have the potential to revolutionize and enhance the lives of humans. However, to function effectively in a realistic environment, biped robots must be able to perform complex, high-speed dynamic maneuvers. No biped robot to date has been capable of performing truly fluid and lifelike dynamic maneuvers, primarily because there is no comprehensive understanding of the design and control necessary to accomplish dynamic maneuvers. The proposed research project seeks to understand the mechanical design requirements necessary to achieve complex dynamic maneuvers through evaluating the design of a prototype series-compliant hopping leg. Design modifications will be made to enhance the reliability and controllability of the leg for high-speed jumping based on experimental observation. Also, a simplified analytical model of the leg will be developed to gain a fundamental understanding of the leg's operation and to improve the hardware's performance. The results of this research are intended to aid in the future development of a full biped robot.

ACKNOWLEDGEMENTS

First of all, I would like to thank my advisor, Dr. Jim Schmiedeler, for taking a chance with me on this research project. This work would not have come about without all of his support and guidance. Also, my co-advisor, Dr. David Orin provided much thoughtful insight and direction throughout the project. I would like to thank all the current and past members of my multidisciplinary research team, including Simon Curran, Po-Kai Huang, Paul Birkmeyer, and Darren Krasny. Their hard work throughout the past two years truly made this project possible. Also, I would like to thank the ME department machinist, Gary Gardner, for his expert machining knowledge and effort on the project as well as Ryan Bockbrader for taking the time to share his mechanical design knowledge with me. Finally, I would like to thank my family and friends for their understanding and support throughout the project.

TABLE OF CONTENTS

ABSTRACT ii
ACKNOWLEDGEMENTS iii
TABLE OF CONTENTS iv
LIST OF FIGURES vi
LIST OF TABLES viii

Chapters:

CHAPTER 1: Introduction 1

1.1 Motivation 1
1.2 Dynamic Maneuvers 2
1.3 Background 3
1.4 Objectives 4
1.5 Existing Hardware 5
1.6 Organization 7

CHAPTER 2: Hardware Improvements to the Prototype Leg 9

2.1 Introduction 9
2.2 Cable Slipping Issues 9
2.3 Potentiometer Bracket 12
2.4 Knee Spring Hard Stop 14
2.4.1 Initial Concepts 16
2.4.2 Final Design 18
2.5 Cable Tensioning System 21
2.6 Carbon Fiber Replacement 25
2.7 Hip Motor Replacement 29
2.8 Results 31
2.9 Summary 33

CHAPTER 3: Prototype Leg Jumping Analysis 35

3.1 Introduction 35
3.2 Kinematic Model 37
3.2.1 Inverse Kinematics 39
3.2.2 Jacobian Determination 40
3.3 Input Torque Determination 41
3.3.1 Saturated Motor Torque 42

3.3.2 Torque/Leg-Length Model 43
3.3.3 Gravitational Torque Penalty 45
3.4 Ground Reaction Force Determination 46
3.4.1 Maximum Torque 47
3.4.2 Manipulating Force Ellipse 47
3.4.3 Vertical – Only Force 51
3.5 Takeoff Determination 52
3.5.1 Constant Force Takeoff 53
3.5.2 Simulation Comparison 53
3.6 Jumping Height Analysis 57
3.6.1 Jumping Loop 57
3.6.2 Foot Offset Loop 58
3.7 Summary 60

CHAPTER 4: Analytical Model Results 62

4.1 Introduction 62
4.2 Motor Model Validation 62
4.3 Simulation Comparison 65
4.3.1 Constant Initial Height 65
4.3.2 Constant Initial Virtual Leg-Length 67
4.4 Comparison of Force Determination Methods 69
4.4.1 Constant Initial Height 69
4.4.2 Constant Initial Virtual Leg-Length 71
4.5 Calculated Joint Torque Profiles 72
4.6 Summary 74

CHAPTER 5: Summary and Future Work 76

5.1 Summary 76
5.2 Future Work 79

APPENDIX A: Mechanical Drawings 82
APPENDIX B: MATLAB Code for Analytical Model 100

BIBLIOGRAPHY 116

LIST OF FIGURES

Figure 1.1: Biped in a Running Jump 3
Figure 1.2: Existing Prototype Leg 6
Figure 1.3: Prototype Leg Experimental Setup 7
Figure 2.1: Original Pulley Design 10
Figure 2.2: Comparison of Original and Longer Set Screw in Pulley 11
Figure 2.3: Crimp Inserted Into Pulley 12
Figure 2.4: Original Gurley Encoder 13
Figure 2.5: Potentiometer Bracket and Shaft Coupler 14
Figure 2.6: Original Knee Design 15
Figure 2.7: Knee Pulley Spring Retainer Deformation 16
Figure 2.8: Knee Spring Hard Stop Concept 1 17
Figure 2.9: Knee Spring Hard Stop Concept 2 17
Figure 2.10: Knee Spring Hard Stop Concept 3 18
Figure 2.11: Knee Spring Hard Stop Final Design 20
Figure 2.12: Moveable Hard Stop Sliding Cutout 20
Figure 2.13: Original Motor Mounts 21
Figure 2.14: Knee Motor Cable Tensioning System 23
Figure 2.15: Tensioning System Assembly 23
Figure 2.16: Body Plate Profile Comparison 24
Figure 2.17: Carbon Fiber Failure 1 26
Figure 2.18: Carbon Fiber Failure 2 26
Figure 2.19: Carbon Fiber Failure 3 27
Figure 2.20: Carbon Fiber Longitudinal Fracture 27
Figure 2.21: Poor Epoxy Coverage on Connector Plug 28
Figure 2.22: Bent Hip Motor Shaft 29
Figure 2.23: Hip Motor Disassembled 30
Figure 2.24: Four Consecutive Jumps 32
Figure 2.25: 15 Consecutive Jumps 33
Figure 2.26: Highest Jump Achieved 33
Figure 3.1: Slider-Crank Overlay on Hardware 37
Figure 3.2: Slider-Crank Model Used in Analysis 38
Figure 3.3: Generic Torque/Leg-Length Curve 44
Figure 3.4: Free Body Diagram of Leg Links 46
Figure 3.5: Manipulating Force Ellipse on the Leg 48
Figure 3.6: Force Determination from Manipulating Force Ellipse 51
Figure 3.7: Physical Limitations for Leg Orientation 59
Figure 3.8: Initial Height Calculation Leg Spans 60
Figure 4.1: Jumping Height Profile Simulation Comparison 1 63

Figure 4.2: Jumping Height Profile Simulation Comparison 2 64
Figure 4.3: Jumping Height Profile Simulation Comparison 3 65
Figure 4.4: Jumping Height Profile Simulation Comparison 4 66
Figure 4.5: Jumping Height Profile Simulation Comparison 5 66
Figure 4.6: Initial starting height profiles. 67
Figure 4.7: Jumping Height Profile Simulation Comparison 6 68
Figure 4.8: Jumping Height Profile Simulation Comparison 7 68
Figure 4.9: Jumping Height Profile Analytical Results 1 70
Figure 4.10: Jumping Height Profile Analytical Results 2 70
Figure 4.11: Jumping Height Profile Analytical Results 3 71
Figure 4.12: Jumping Height Profile Analytical Results 4 72
Figure 4.13: Joint Torque Profile Comparison 1 73
Figure 4.14: Joint Torque Profile Comparison 2 74

LIST OF TABLES

Table 3.1: Motor Torque Parameters 42
Table 3.2: Gravitational Torque Parameters 46
Table 3.3: Body Velocity Takeoff Parameter 55
Table 3.4: Ground Reaction Force Takeoff Parameter 55
Table 3.5: Virtual Leg Length Takeoff Parameter 55
Table 3.6: Updated Simulation Takeoff Parameters 56

CHAPTER 1

INTRODUCTION

1.1 Motivation

The interest in legged locomotion is founded in observation of the biological world. Even a quick survey of land-based animals shows that legs are the overwhelming choice of locomotion, all the way from the numerous legs of a millipede down to a bipedal human. Studying legged machines can enhance our understanding of legged locomotion in humans and animals as well as the underlying biological principles that control legged movement [1]. Conversely, the biological world can be looked to for valuable inspiration in the design of legged vehicles, despite the inherent differences between animals and mechanical systems [2].

One of the leading motivations for investigating legged locomotion in robotics is to gain the advantage that legged machines offer in mobility. Wheeled and tracked machines currently dominate the mechanized vehicular landscape because of their simplistic and well-understood rolling locomotion methods. However, these vehicles require a continuous path of motion, and their advantages break down when faced with obstacle-ridden terrain. Legged vehicles can provide superior mobility through rough and uneven terrain because only discrete footholds are required for traction and support [1]. By effectively selecting footholds, a legged machine could negotiate obstacles that would stop a similar sized wheeled or tracked vehicle without changing speed or direction.

Biped locomotion is of particular interest because humans themselves are bipeds. A bipedal, humanoid-type robot would be advantageous over higher-legged machines, such as quadrupeds or hexapods, when assisting and interacting with humans in an environment designed around humans. Additionally, biped robots offer a simpler structural design and control scheme than their higher-legged counterparts. The potential applications for biped robots extend from domestic assistance to search-and-rescue missions in a debris field. Bipeds can also be used for scientific exploration of inhospitable environments such as extraterrestrial locations [3] as well as for military surveillance or reconnaissance [4].

1.2 Dynamic Maneuvers

Biped robots must be capable of complex dynamic maneuvers to function effectively in a realistic environment. Dynamic maneuvers would allow a biped robot to interact naturally and adapt to continually changing surroundings. To date, no robotic system is capable of performing the truly fluid dynamic maneuvers that humans and animals can. Honda's ASIMO [5] and Sony's QRIO [6] are capable of dynamic running, but their running gait is a repetitive motion based on their quasi-static walking gait. ASIMO and QRIO require large feet to remain stable, and they lack the ability to swiftly change their motion.

A non-repetitive dynamic maneuver can generally be defined as a sudden change in speed or trajectory involving a significant acceleration that interrupts dynamic locomotion, such as running [7]. Additionally, to successfully execute a dynamic maneuver, the system must remain dynamically stable throughout the motion. One good

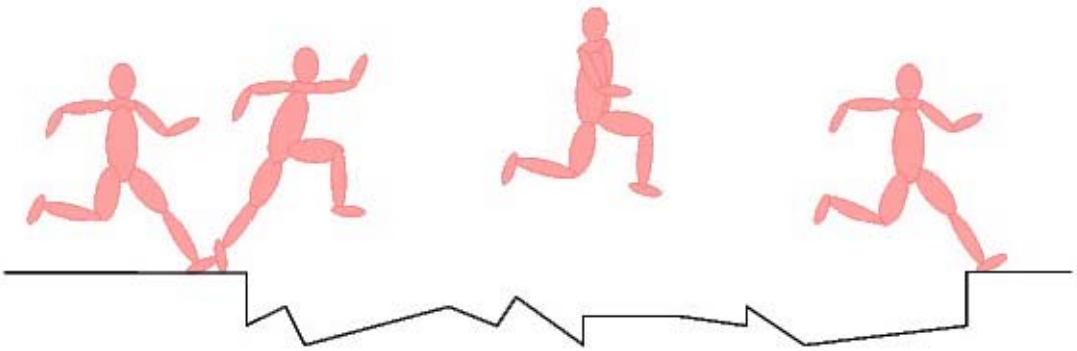

Figure 1.1: Biped in a Running Jump (Courtesy of Dr. David Orin)

example of a non-repetitive dynamic maneuver is a running jump, shown in Figure 1.1. A running biped transitions into a ballistic trajectory and back, requiring asymmetrical limb control to takeoff and land stably. Other typical dynamic maneuvers include turning, dodging, and rapid starts and stops. Biped robots can take full advantage of their legged mobility by executing these dynamic maneuvers for obstacle avoidance without sacrificing speed and stability.

1.3 Background

The study of mechanized legged locomotion began in the 1850s with Chebyshev's walking machine [8]. The quadruped machine used mechanical linkages to generate a fixed stepping motion. Nearly 100 years later, the focus shifted to developing articulated limbs that used logic controls to generate walking motions. The "Phony Pony", a quadruped created by Frank [9] and McGhee [10], was the first digitally controlled robot capable of walking, despite being bulky and slow moving.

The first biped robots capable of statically stable walking, the WAP-1 and WAP-3, were developed by Kato in the late 1960s. Kato's efforts culminated in the WABOT-1 [11], which was a 10-degree-of-freedom (DOF), hydraulically actuated biped that could perform a 3-D walking gait. In 1984, the hydraulically actuated WL-9DR [12] achieved

quasi-dynamic walking in that the transfer of static support from one foot to the other was a dynamic movement. Since then, numerous humanoid biped robots, such as BLR-G2 [13] and PINO [14], have effectively used electrical actuation for quasi-dynamic walking.

A parallel path in the development of dynamic maneuvers in robots has been to dramatically simplify the mechanical design. In 1980, Matsuoka's [15] monopod achieved a fully dynamic hopping gait, complete with periods of flight. Biper-3 [16] achieved a dynamic walking gait, but the robot had only 2-DOF hip joints, with no knee or ankle joints. Then in 2001, the Spring Flamingo, developed by Pratt [17], achieved dynamic walking in excess of 1 m/s and had single DOF, electrically-actuated hip, knee, and ankle joints.

Recent work in dynamic maneuvers has seen a convergence of the two paths with the continued development of more complex biped robots. In 2003, Sony's humanoid biped QRIO achieved running and the ability to jump small heights [6]. In 2004, Honda caught up with their humanoid biped ASIMO, demonstrating its ability to run [5]. However, both robots' running gaits were not true dynamic motion, but a sped up version of their quasi-static walking gate. The only robot to date capable of stable dynamic running is RABBIT, a planar biped robot that took six running steps in 2004 [18].

1.4 Objectives

The overall objective of this research work is to investigate dynamic maneuvers in biped robots. The method used to achieve this objective is actually two-fold. The first goal is to develop a novel control approach based on evolutionary algorithms capable of generating dynamic maneuvers. The second goal is to develop supporting hardware that

will be used to test and validate the control approach. The immediate focus of the research is to investigate dynamic maneuvers using a single prototype robotic leg. Eventually, the knowledge gained from studying this smaller system will be incorporated into the development of a full biped robot.

This thesis focuses on analyzing and evaluating the design of the existing prototype robotic leg. The goal was to learn what design features are important in accomplishing dynamic maneuvers with the leg and ultimately with a biped robot. Fast limb cycling and high jumping were set as performance goals for the leg, so the hardware had to be robust and reliable enough to handle high-speed operation. Mechanical design support was provided to improve the existing hardware system. Additionally, an analytical model of the leg was developed to characterize the hardware's operation and aid in improving the leg's overall performance. Finally, the leg's design and control were validated through experimentation.

1.5 Existing Hardware

This section provides a brief overview of the prototype robotic leg exclusively used in this thesis work. The prototype leg, shown in Figure 1.2, was designed and built by Joseph Remic for his Master's thesis in 2005 [19]. The leg is a series-compliant, articulated hopping leg with 2-DOFs, one each at the hip and knee joints. Each joint is individually actuated by a brushless DC motor from Maxon Motors, and the joints are connected to the actuators through a pulley and steel cabling system. The knee joint power train is series compliant because the knee motor is connected to the shank through a torsion spring. The hip joint, however, is not series compliant because it lacks the

compliant spring element. The knee motor is more powerful than the hip motor, producing a maximum of 20Nm compared to 7Nm for the hip.

Aluminum makes up the majority of the structural components of the leg. However, the hip and knee axles are steel, and the thigh and shank are carbon fiber tubes. Each axle is supported by radial ball bearings to decrease rotational friction. The distance between the hip and knee axes, as well as between the hip and the tip of the foot is 5.5in. The foot is a hemispherical shell with a switch inside to sense contact with the ground.

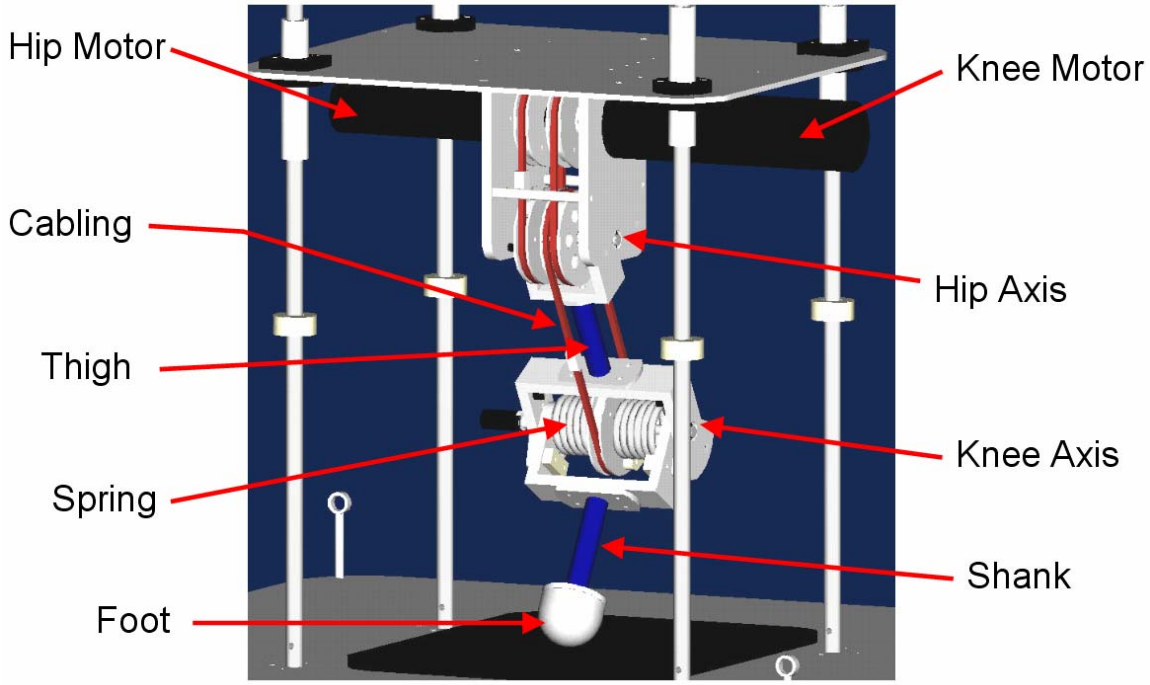

Figure 1.2: Existing Prototype Leg

The entire leg system, which weighs around 9 lbs, is constrained to only vertical motion. Figure 1.3 shows the experimental setup for the prototype leg. The body of the leg rides on four vertical rails using linear bearings to reduce the friction. The top and bottom of the rails are held in place with aluminum plates and steel cabling. The control electronics are mounted directly on the body of the leg and controlled wirelessly from a

nearby computer. The leg is powered by an off-board power supply that supplies the leg through an umbilical cable. There are two handles on the leg for easy handling, and a rubber pad beneath the foot provides a non-slip jumping surface.

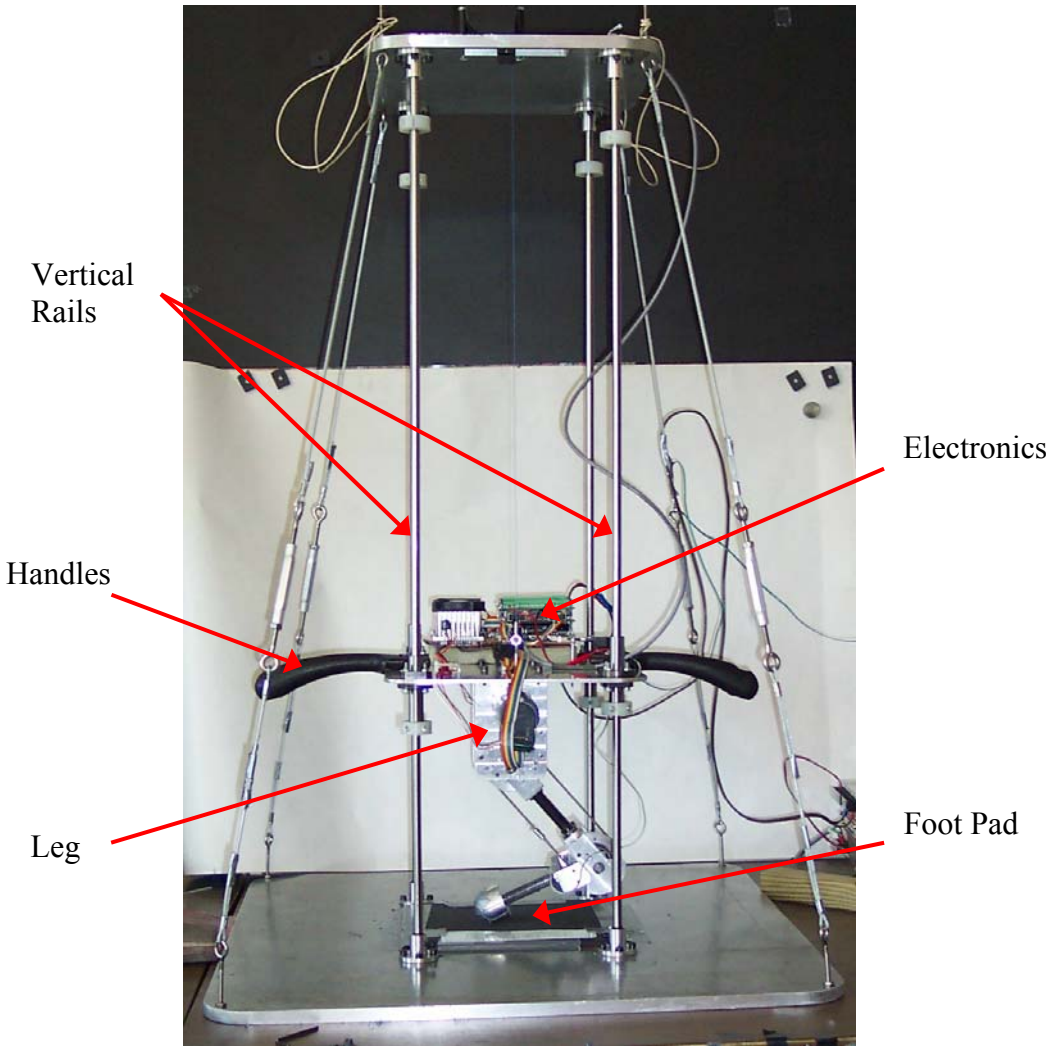

Figure 1.3: Prototype Leg Experimental Setup

1.6 Organization

Chapter 2 details the improvements made to the existing prototype leg. Several of the modifications were made to improve the leg's controllability, while the remaining modifications were made in response to mechanical failure. The chapter also presents a

brief section of experimental results validating the hardware's function. Chapter 3 develops the analytical model that characterizes the leg's performance. The model's assumptions and formulation are described, and references are given to its implementation in a MATLAB script. Chapter 4 presents results from the analytical model and compares them to results from a dynamic simulation. Finally, Chapter 5 summarizes the entire work and provides recommendations for future research.

CHAPTER 2

HARDWARE IMPROVEMENTS TO THE PROTOTYPE LEG

2.1 Introduction

One of the primary efforts of this research work was to provide mechanical design support for the prototype hopping leg introduced in the previous chapter. The intended goal was to improve the operating performance and reliability of the existing system. Mechanical design improvements to the leg hardware were made based on evaluation of the leg's performance during experiments. Several of the design improvements were made to improve the mechanical system's controllability. These included a solution to cable slipping, the addition of a knee potentiometer, and the design of a knee spring hard stop. The remainder of the design improvements were made because a component of the existing hardware experienced a mechanical failure. These changes included the addition of a cable tensioning system, the replacement of the carbon fiber tubing, and the replacement of the hip motor. This chapter details the design improvements made to the prototype leg in the order outlined above. The final sections present some preliminary experimental results from the prototype leg and provide a summary.

2.2 Cable Slipping Issues

The problem of cable slipping was a significant control issue for the prototype hopping leg. As stated in the previous chapter, the leg's motors were connected to the hip and knee joints with steel cabling. For each joint, a cable was wrapped around one

pulley attached to the motor output shaft and one pulley attached to the joint axis. A cylindrical compression fitting was used to secure the cable to each pulley, which is shown in Figure 2.1 [19]. The cable fit inside a channel cut into the interior of the pulley, and a set screw compressed an aluminum cylinder against the cable inside the channel. The cable was held in place by the compression force of the cylinder and the sharp angles of the channel.

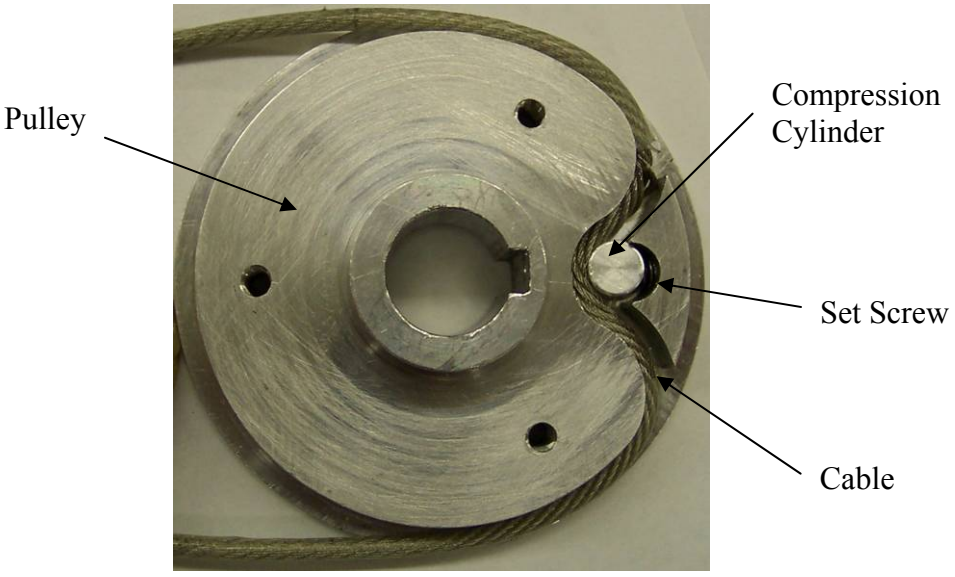

Figure 2.1: Original Pulley Design [19]

The integrity of the compression fittings were critical to the leg's performance, since all torque transmitted from the motors to the joint axes was delivered through the pulleys. The forces exerted on the compression fittings during jumping experiments were high enough to cause the cable to slip relative to the pulley. The slipping was observed by comparing the position encoder values on the motor before and after a jump in an initialization position. A discrepancy indicated slipping had occurred. If the slipping had occurred during the power stroke phase of a jump, it would result in reduced power transmitted to the joint axis. This slipping also caused an error in the leg's position

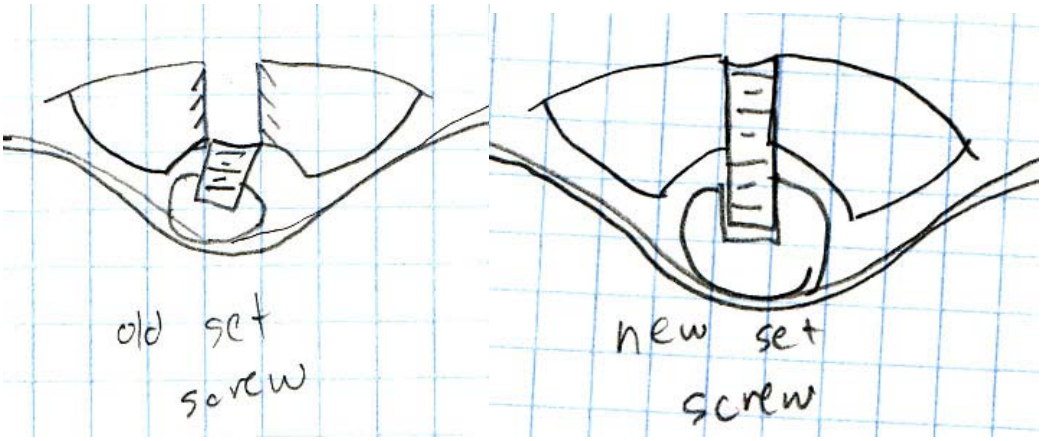

Figure 2.2: Comparison of Original and Longer Set Screw in Pulley

control because the angular position of the joint relative to the motor encoder had changed. The problem was first seen in the knee axis pulley, but it was eventually observed in all four pulleys.

The first attempted solution to prevent cable slipping was to stabilize the aluminum cylinder inside the compression fitting. Inspection of a compression fitting that was slipping showed that the cylinder and set screw had rotated inside the channel relative to the cable, as seen in Figure 2.2. The original 0.25in-long set screw was replaced by a longer 0.375in set screw to provide more thread engagement and horizontal holding force. Also, the cylinder was shorter than the depth of the channel. A metal shim was used to stabilize the cylinder inside the channel in an attempt to provide additional holding force between the pulley and the pulley cover. This method was attempted on the knee and hip axis pulleys with success.

The stabilization method failed, however, on the hip and knee motor pulleys, likely because the shocks seen by the compression fittings were higher due to the direct connection to the motors. To solve this slipping problem, an aluminum crimp was placed on the cable and inserted into the channel in the pulley, as shown in Figure 2.3. The crimp was shaped with a Dremel and press fit into the channel's opening in place of the

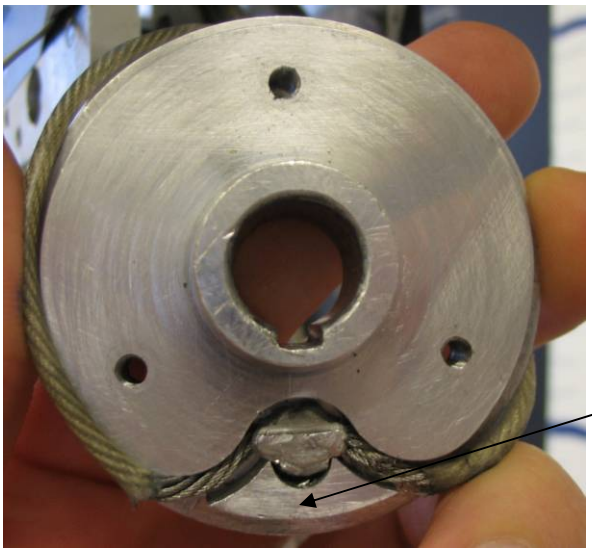

Figure 2.3: Crimp Inserted Into Pulley

aluminum cylinder and set screw. The compression fit between the crimp and the cable provided a much higher holding force than the aluminum cylinder and prevented slipping between the cable and the motor pulleys. Also, the press fit between the crimp and the channel prevented any backlash in the cabling system, which would cause positioning control problems. This crimp solution was applied only to the hip and knee motor pulleys.

2.3 Potentiometer Bracket

Reliable position measurements of the leg's joint angles were required to enable accurate position control during jumping. The hip and knee motors used integrated optical encoders to measure their position, which allowed for absolute measurement of the thigh angle, but not the shank angle. The torsion spring between the knee axis pulley and the knee axis prevented the absolute measurement of the shank angle because the spring's deflection at any given instance was unknown. Originally, an optical encoder manufactured by Gurley, shown in Figure 2.4, was attached to the knee shaft between the

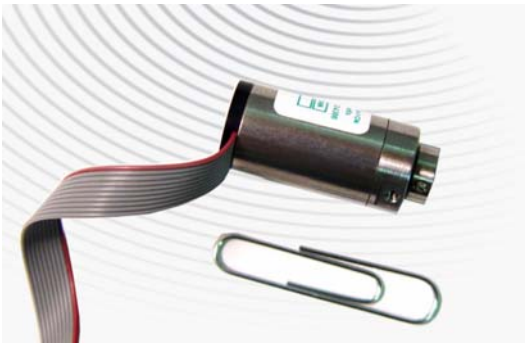

Figure 2.4: Original Gurley Encoder [19]

shank and the thigh to measure the relative angle [19]. The absolute shank angle could be computed from the Gurley encoder's angular measurement and the thigh angle.

The Gurley encoder proved to be electrically unreliable for use on the leg. There were severe problems with electrical noise, preventing any useable information to be obtained from the encoder. This problem was known to the manufacturer, who suggested electrically isolating the encoder from the aluminum hardware to eliminate noise. During the summer of 2006, a fellow undergraduate researcher, Jeff Wensink, designed an electrical isolation mount for the Gurley encoder. The solution used a plastic mounting bracket and a plastic connecting shaft in an attempt to isolate the encoder and prevent interfering ground loops in the electrical connections. However, the electrical noise issues with the encoder continued even with the increased isolation.

The Gurley encoder was replaced by a precision potentiometer in an effort to eliminate any electrical noise issues. The potentiometer selected was identical to the one used successfully for the same application on ERNIE, a biped robot built by Dr. Jim Schmiedeler's lab at The Ohio State University. A mounting bracket was designed to hold the potentiometer and secure it to the thigh fork using the existing mounting holes from the Gurley encoder bracket. Figure 2.5 shows the bracket design with the potentiometer mounted on the leg. The bracket was fabricated out of 0.050in-thick sheet

aluminum as opposed to solid aluminum to reduce machining costs. An aluminum shaft coupler was designed to connect the potentiometer shaft to the knee axis shaft. Two 0.25in-long, #4-40 set screws offset by 120° were used to secure each shaft to the shaft coupler. Detailed drawings of the potentiometer bracket and the shaft coupler can be found in Appendix A.

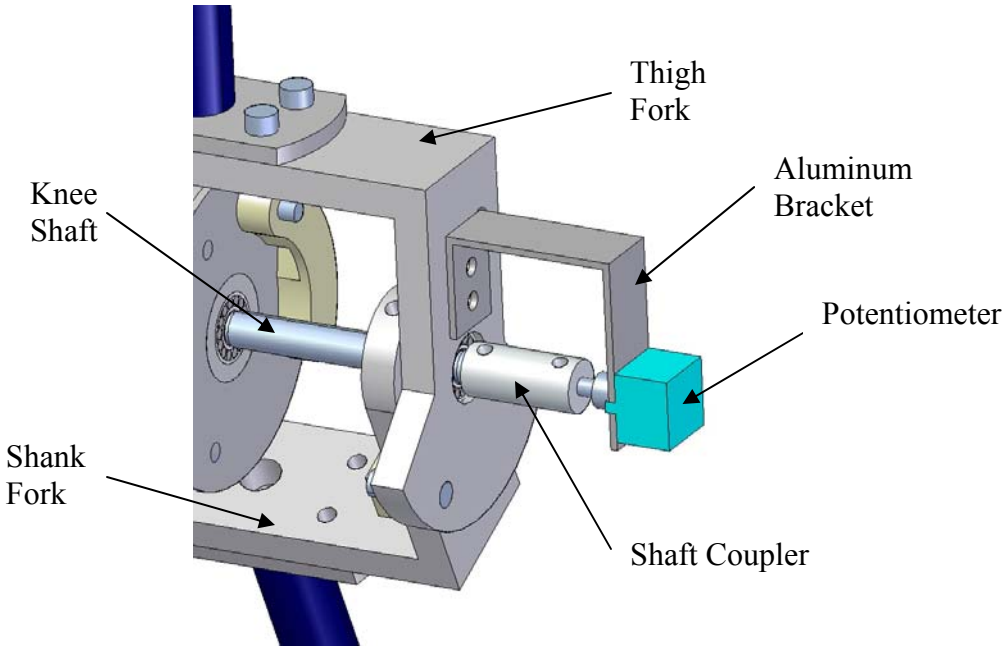

Figure 2.5: Potentiometer Bracket and Shaft Coupler

2.4 Knee Spring Hard Stop

The knee spring hard stop system was added to the leg in an effort to improve the position control of the knee joint. As detailed in Chapter 1, the knee joint was driven by a series compliant drive train. The knee motor attached to the shank through a cabling system in series with a torsion spring. A secure connection between the shank and the torsion spring and between the torsion spring and the knee pulley was required to ensure accurate and reliable position control of the shank. In the original design, which is shown

in Figure 2.6, the spring attached to the shank and the knee pulley with simple slotted brackets called spring retainers to hold the spring ends [19].

The original design proved to be problematic for accurate position control in several ways. First, the dimensions of the spring retainer slots were noticeably larger than the diameter of the spring. Also, the spring retainers were machined out of aluminum and subject to deformation under the high spring loads. Figure 2.7 shows an example of the deformation that occurred in the knee spring retainer from the force of the spring during jumping. These problems combined to create slop in the knee joint that allowed the shank to rotate up to approximately 10° relative to the knee spring. The unpredictable rotation caused positioning problems with the shank because its precise location was never known. Also, the original design allowed the torsion spring to be back driven beyond its uncompressed state, which could lead to mechanical failure in the spring.

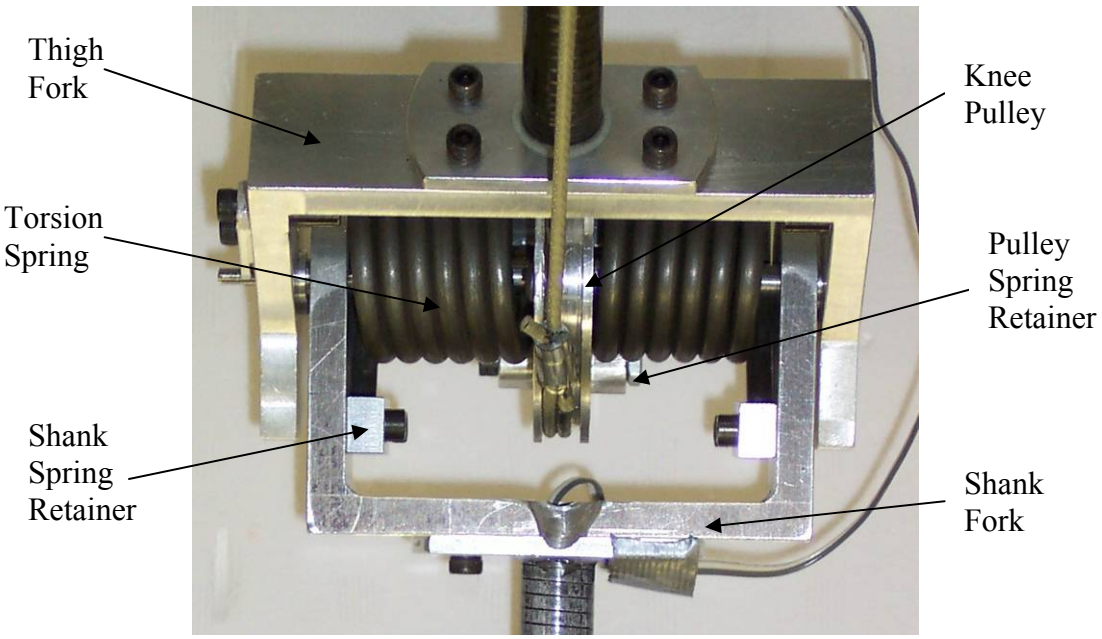

Figure 2.6: Original Knee Design [19]

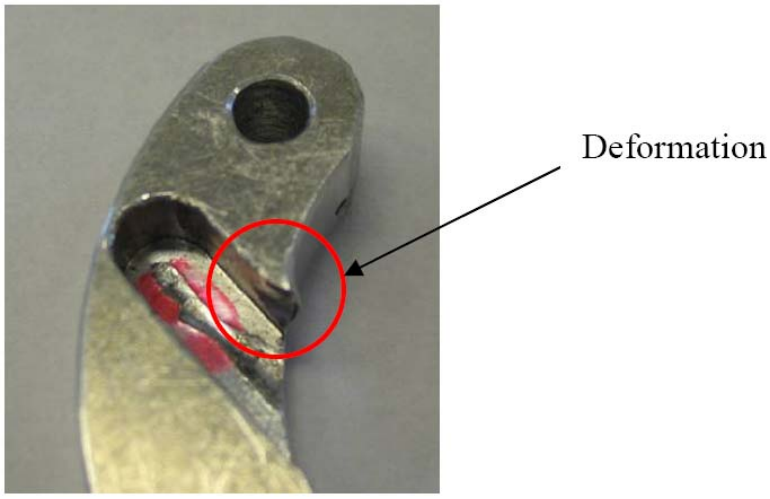

Figure 2.7: Knee Pulley Spring Retainer Deformation

2.4.1 Initial Concepts

The general design requirements of the knee spring hard stop were aimed at solving the position control problems present in the original knee design. The first goal was to eliminate all slop in the spring connections. The second goal was to prevent the spring from being driven in the opposite direction beyond its uncompressed state. Several initial concepts were devised to satisfy these two design requirements.

All three initial concepts used a similar mechanical hard stop method to prevent the spring from rotating beyond a certain point. The first concept is shown in Figure 2.8. The design had two concentric shafts with the first one attached to the thigh fork for stability. The secondary shaft rotated with the knee pulley and engaged the hard stops on the outside of the shank fork when the spring reached its uncompressed state. Power was transmitted through the spring in the forward direction and through the secondary shaft and hard stops in the reverse direction. This concept was rejected because it required a costly and time-consuming redesign of all the knee components including the forks, shafts, and bearings.

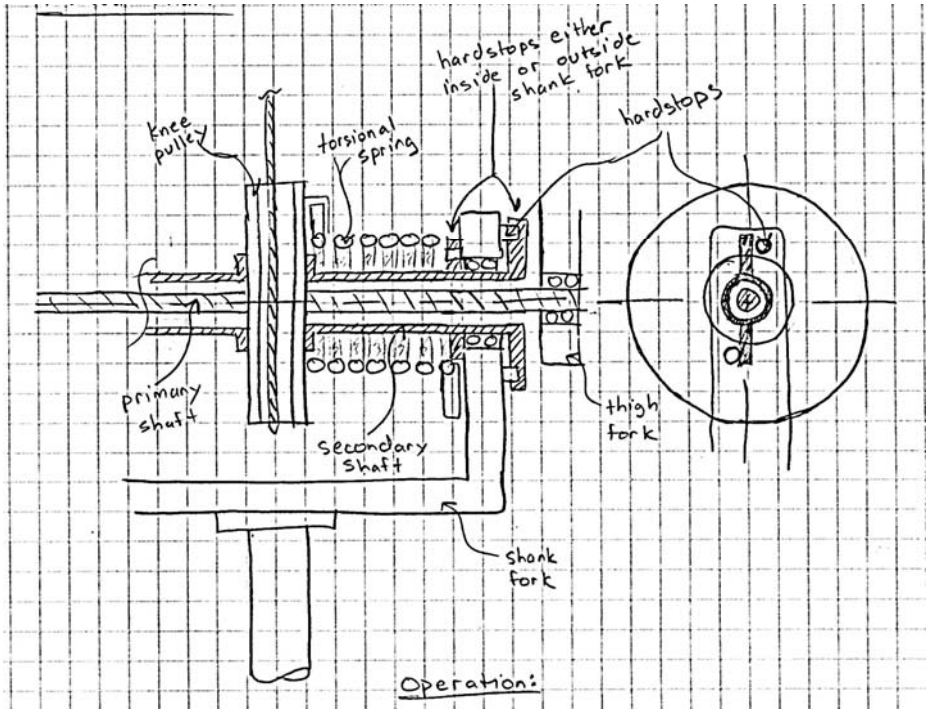

Figure 2.8: Knee Spring Hard Stop Concept 1

The second concept is shown in Figure 2.9. It used a similar hard stop method as the first concept, except that the hard stop location was moved to the knee pulley. A bolt attached to the knee shaft passed through a circular arc slot in the knee pulley. In the reverse direction, power was transferred from the pulley through the bolt to the knee shaft

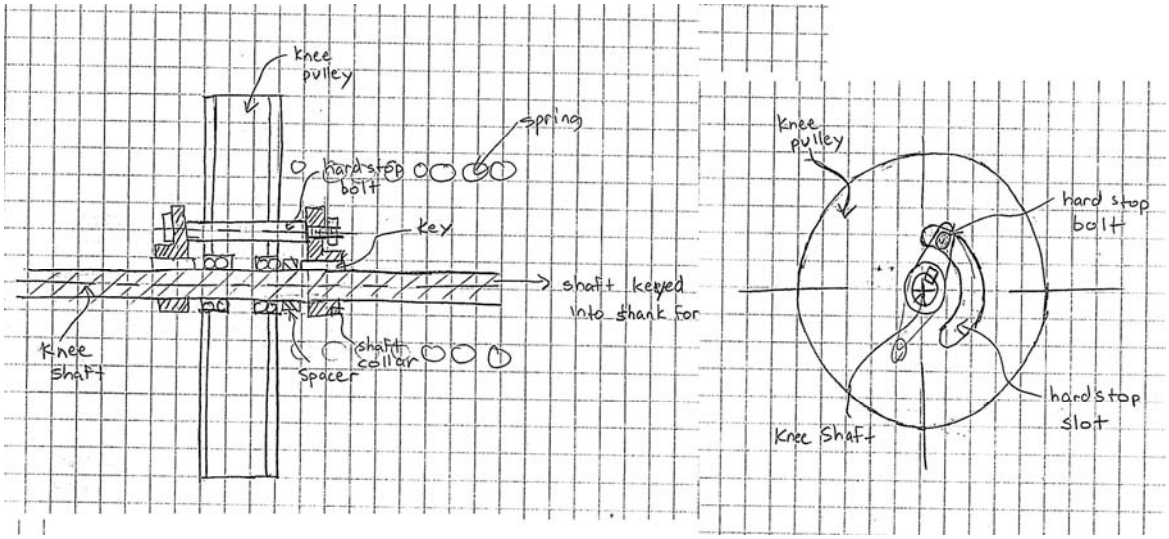

Figure 2.9: Knee Spring Hard Stop Concept 2

and shank. The second concept was considerably simpler than the first, but the concern over available space for the bolt and the integrity of the pulley with a cutout ultimately led to its rejection.

The third concept is shown in Figure 2.10. The hard stop was moved from the inside of the spring on the knee shaft to the outside of the spring on the shank fork. A rod pressed into the pulley would engage a hard stop mounted on the shank fork and allow the pulley to rotate relative to the shank fork in only one direction. This location would have more space to accommodate the additional hardware and minimize the extent of the changes to the existing hardware. The third concept was chosen as the basis for the final design of the knee spring hard stop.

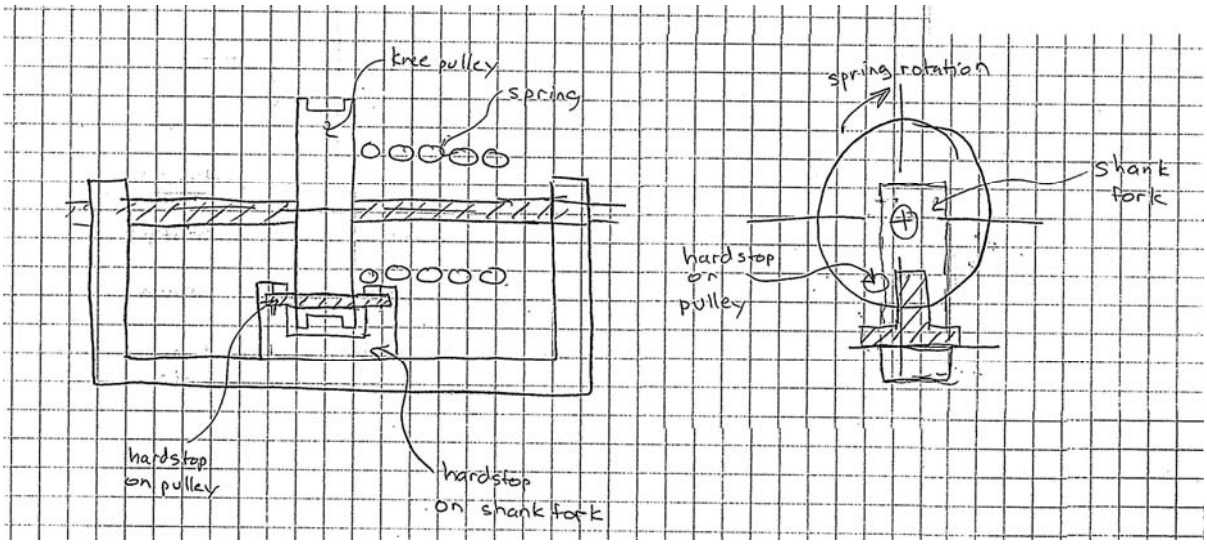

Figure 2.10: Knee Spring Hard Stop Concept 3

2.4.2 Final Design

Figure 2.11 shows the final design of the knee spring hard stop on the shank of the leg. It included two knee pulley hard stops, a shank fork movable hard stop, and a hard stop holder. The knee pulley hard stops engage the shank fork hard stop to prevent the pulley from rotating relative to the shank in the reverse direction and back driving the

torsion spring. The moveable hard stop and the hard stop holder were designed to work together as an adjustable shank fork hard stop. The U-shaped design allows the moveable hard stop to engage either side of the knee pulley, and the moveable hard stop slides perpendicular to the knee shaft in a slot cutout in the hard stop holder, which is shown in Figure 2.12. The exact location of the movable hard stop is adjustable by a #6-32 tensioning screw that threads into the hard stop holder. This adjustment allows the spring to be preloaded and eliminates any slop in the spring connections.

The hard stop holder was secured with four countersunk #6-32 machine screws to the shank fork. A slight interference fit between the holder and the hard stop kept the moveable hard stop securely in place after tightening the four connecting bolts. Both parts were machined out of aluminum in an effort to reduce the overall weight of the new parts. Detailed drawings for the knee spring hard stop are available in Appendix A.

The final design for the knee spring hard stop was adopted from the third initial concept developed in the previous section with several changes. The knee pulley hard stop was changed from a rod pressed through the knee pulley to an extension of the knee pulley spring retainers. These spring retainers were redesigned with a longer arc length and machined out of steel to reduce the deformation seen in the original aluminum parts. The shank fork spring retainers were also re-machined out of steel to the specifications of the original part.

The first set of new knee pulley spring retainers did not have a long enough arc length to engage the moveable hard stop before it was adjusted to its limit position. The error was the result of inability to create an accurate CAD model of the spring, around

which all the parts were designed. The knee pulley spring retainers were redesigned with a longer arc length to allow proper engagement with the moveable hard stop.

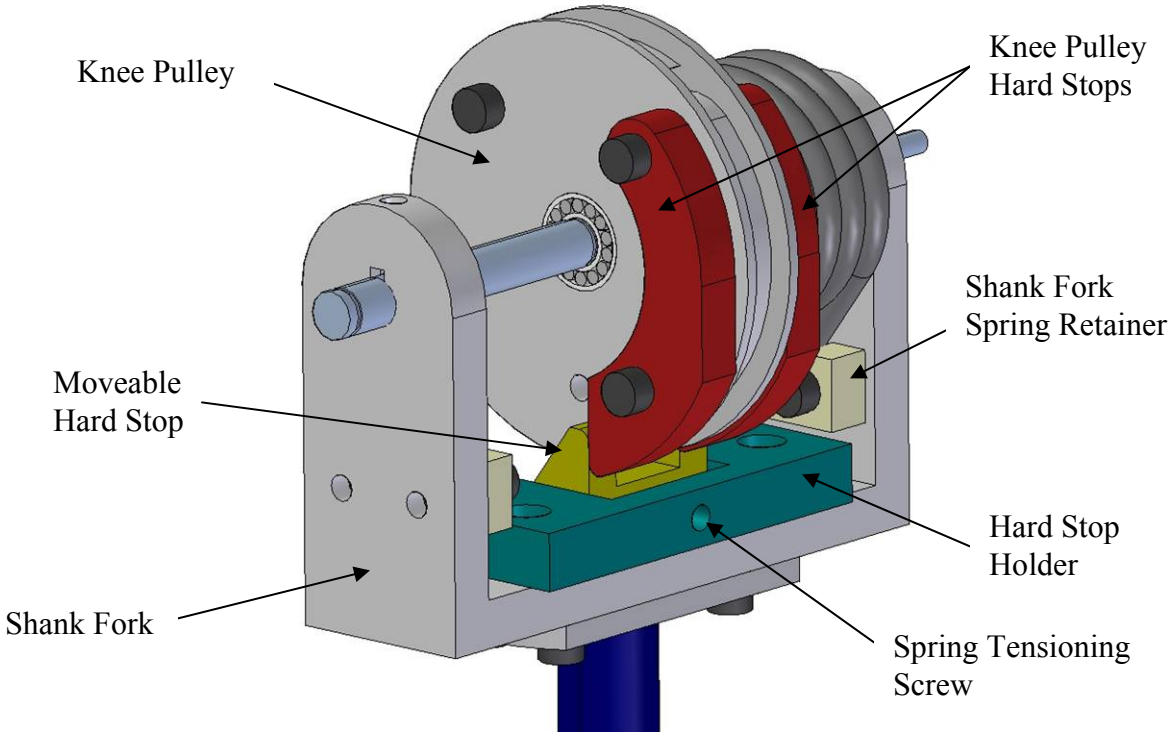

Figure 2.11: Knee Spring Hard Stop Final Design

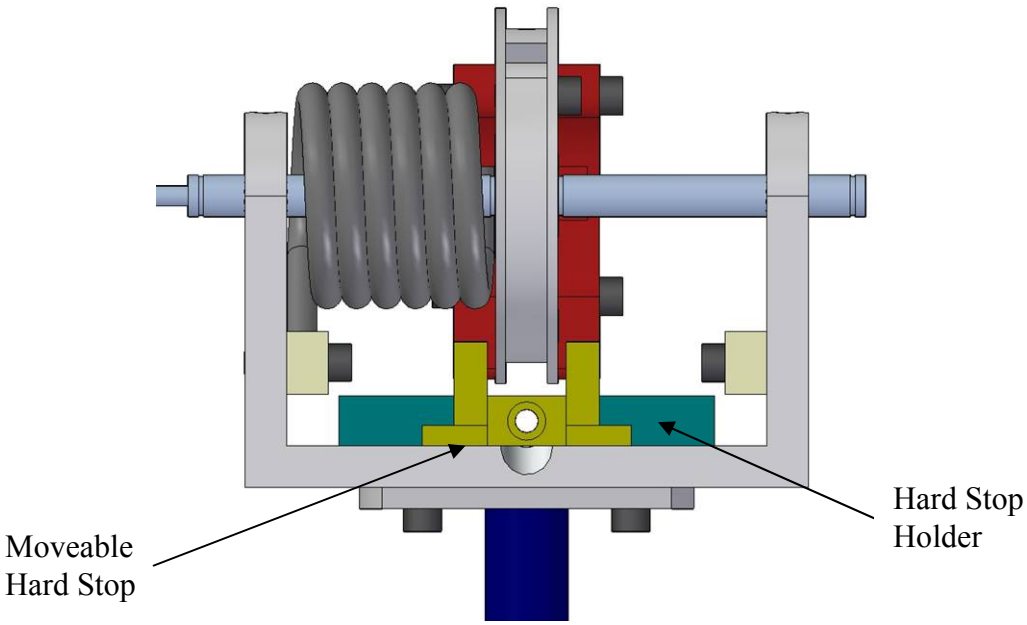

Figure 2.12: Moveable Hard Stop Sliding Cutout

2.5 Cable Tensioning System

The addition of a cable tensioning system was one of the major hardware redesigns aimed at correcting mechanical failure issues. The original design of the leg provided no means to adjust the tension of the cables that connected the motors to their respective driving joints. Figure 2.13 shows the original design of the body plates and the motor mounts for the leg. The knee and hip motors were bolted directly to the body plates, creating a fixed distance between all the axes of the leg and a constant cable tension.

This lack of adjustment resulted in several component failures, as well as general difficulty in servicing the leg hardware. The process of assembling the cabling system required that the cable length be cut and crimped to size off the hardware and then forced onto the pulleys [19]. In order to reduce cable compliance and transmit power more efficiently, the cable tension needed to be relatively high. This high tension resulted in large forces during assembly that the leg hardware was not designed to handle. Particularly, the hip axis was subject to large lateral forces that damaged the ball bearings

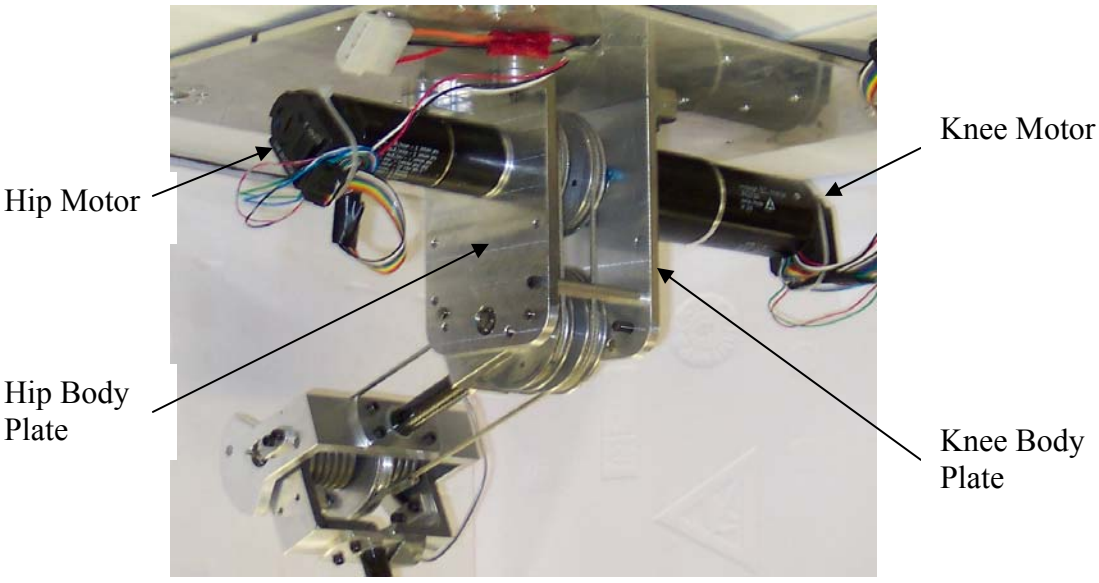

Figure 2.13: Original Motor Mounts

connecting the hip shaft to the body plate. The high tension also created large forces that damaged the hip motor output shaft, which will be discussed in more detail in Section 2.7. In addition, the only way to correct any cable tension errors with the original system was to cut an entire new length of cable.

A cable tensioning system was designed to eliminate these assembly difficulties and failures with the leg hardware. The basic operation was to allow for the distance between axes to be adjusted, resulting in a variable tension in the connecting cables. Adjusting the motor shaft position relative to the joint axis and the body was the most convenient method of implementing a tensioning system because it required the simplest hardware changes. The tensioning system design only required four new parts per motor and utilized the same basic geometry of the previous design with only minor adjustments.

The cable tensioning assembly for the knee motor is shown in Figure 2.14. It includes a new body plate, a motor tensioning plate, and two clamping plates. The knee motor bolts to the tensioning plate in the same manner as it bolted to the original body plate. The tensioning plate fits into the cutout in the new body plate and is capable of sliding up and down. The cutout in the body plate is longer than the tensioning plate, allowing for 0.25in of travel. A 2in-long piece of ¼-28 steel all-thread passes through the body plate into the tensioning plate and is used to adjust the position of the tensioning plate. After the body plate is assembled onto the entire leg, an adjustment nut threads onto the top of the all-thread, which can be seen in Figure 2.15. Turning the nut raises or lowers the tensioning plate relative to the body plate, thereby altering the tension in the knee axis cable.

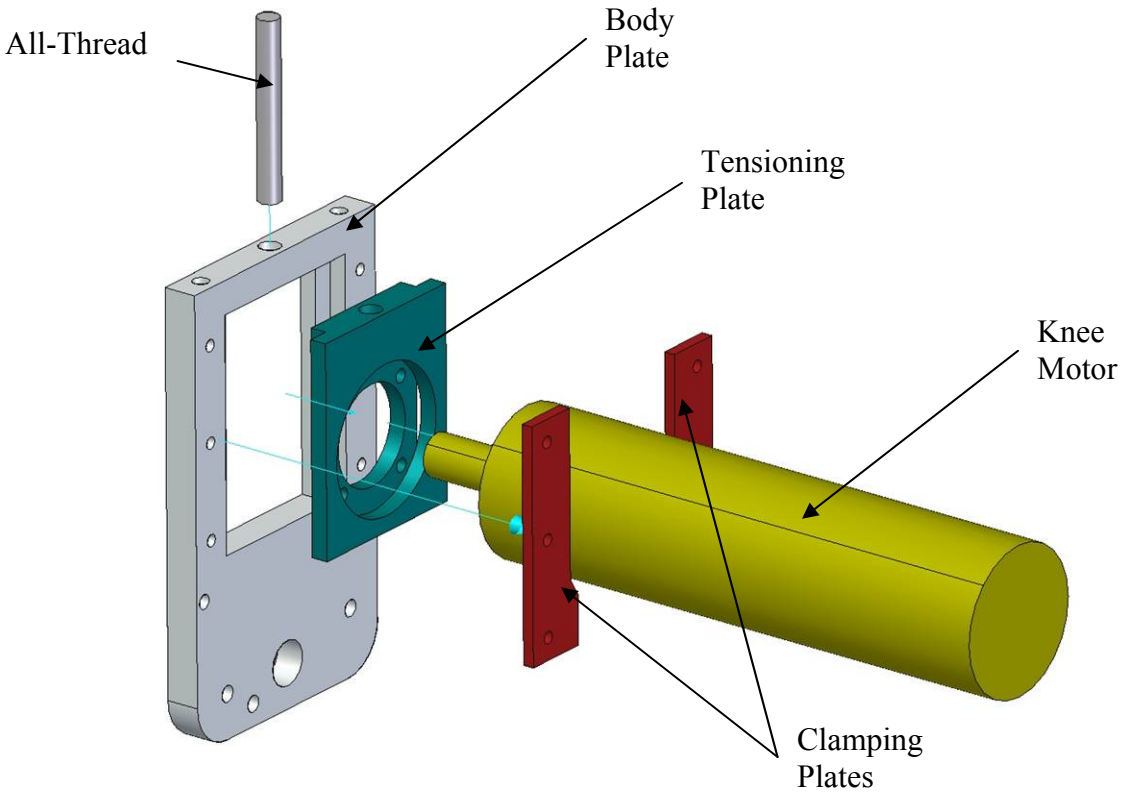

Figure 2.14: Knee Motor Cable Tensioning System

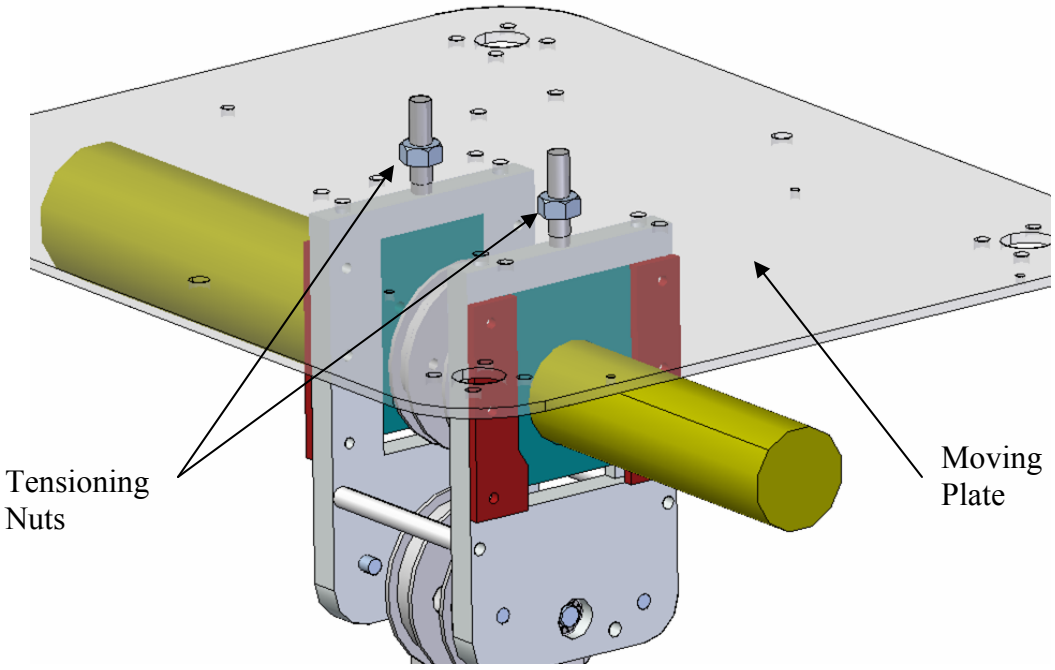

Figure 2.15: Tensioning System Assembly

The new body plate and tensioning plate were machined out of 0.375in-thick aluminum. Initially, the body plate was to use the same L-shaped design as the original body plate. However, Keith Rogers, former Ohio State University ME Department Machinist, suggested eliminated the L-shaped tabs and increasing the plate thickness enough to allow the all-thread and mounting bolts to pass directly through the thickness of the plate. This design change saved a considerable amount of machining time and material. Figure 2.16 shows a profile comparison of the original body plate with the new body plate.

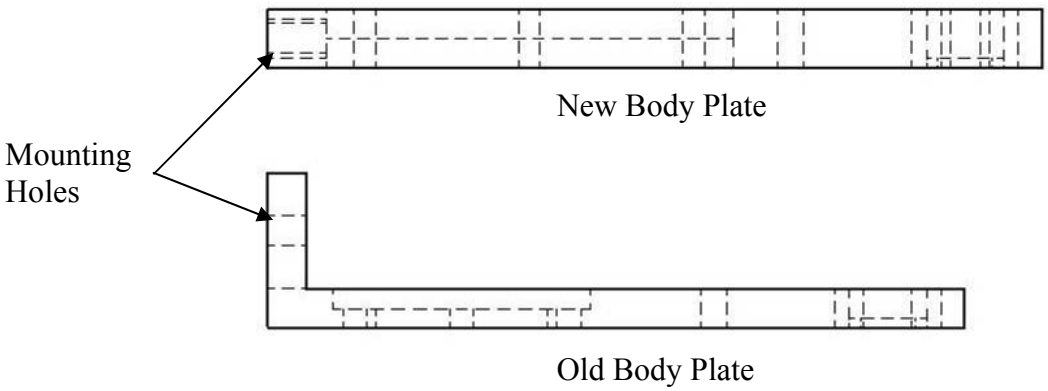

Figure 2.16: Body Plate Profile Comparison

The clamping plates were used to secure the tensioning plate in the body plate. Each clamping plate was held in place with three #6-32 socket head cap screws. The tensioning plate was machined to protrude slightly outward, around 0.003 in, from the body plate when resting in the sliding cutout. This created an interference fit when the clamping plates were bolted onto the body plate. The interference fit provided an additional holding force on the tensioning plate to prevent it from slipping during

jumping. Any slippage would cause the cable tension to decrease, and the leg's performance would suffer.

The cable tensioning system for the hip motor was identical in design and operation to the knee motor's cable tension system except for the hip motor tensioning plate. Since the hip motor was smaller than the knee motor, the bolt pattern and motor mounting hole were adjusted on the hip motor tensioning plate accordingly. Detailed mechanical drawings for the knee and hip motor tensioning systems can be found in Appendix A.

2.6 Carbon Fiber Replacement

The carbon fiber tubing on the thigh experienced three failures over the course of experimentation. The first failure occurred when the knee motor continued driving the thigh into the forward hard stops on the body. The motion between the hip axis and knee axis is coupled, so the knee motor has the ability to drive the hip joint. The impact of the hip fork with the hard stops caused the carbon fiber to fracture longitudinally down the tube and separate from the hip fork connector plug. Figure 2.17 shows a still-frame of the failure moments after impact. The separation of the carbon fiber and connector plug can clearly be seen.

A new carbon fiber tube length was cut to replace the failed section. The residual epoxy and remaining carbon fiber fragments were removed from the aluminum connector plugs using a Dremel sanding wheel. The surface of the connector plugs and the inside of the tubes were lightly abraded with 80 grit sandpaper and cleaned with isopropyl alcohol. Hysol 9460 epoxy was used to adhere the new carbon fiber tube with the aluminum plugs, and the assembly was laid to dry horizontally for 72 hours. The epoxy

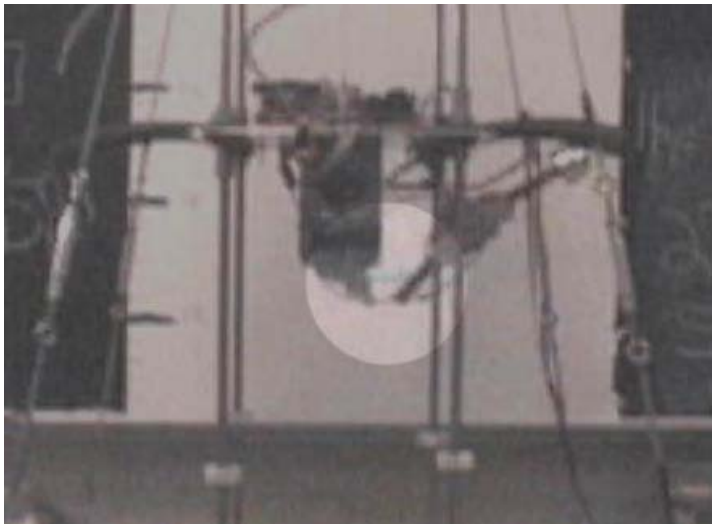

Figure 2.17: Carbon Fiber Failure 1

procedure was recommended by the Hysol 9460 datasheet [20] and was similar to the epoxy procedure used on the biped robot ERNIE.

The new assembly failed on the first test run in an almost identical situation as the first carbon fiber failure. In this failure, the carbon fiber tube separated from the thigh fork connector plug instead of the hip fork connector plug. Figure 2.18 shows a still-frame moments after the failure occurred. The carbon fiber tube was replaced using the same method stated above. However, the residual epoxy and carbon fiber were removed using acetone instead of sanding.

Figure 2.18: Carbon Fiber Failure 2

This third assembly also failed in a similar manner as the previous two. The carbon fiber split longitudinally down the tube and separated from the thigh fork connector plug. However, the failure occurred during the power stroke of a jump, and the thigh did not impact the body hard stops. Figure 2.19 shows a still-frame moments after failure, and Figure 2.20 shows the longitudinal fracture in the carbon fiber tube.

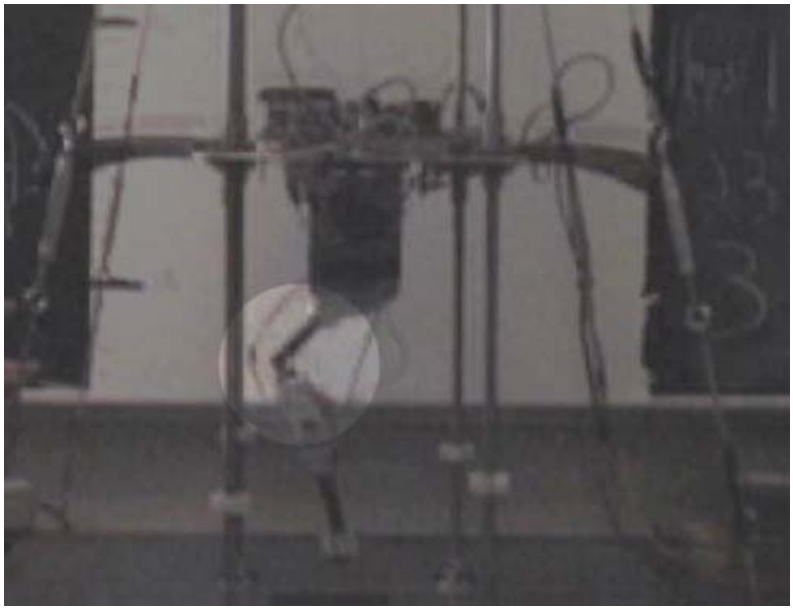

Figure 2.19: Carbon Fiber Failure 3

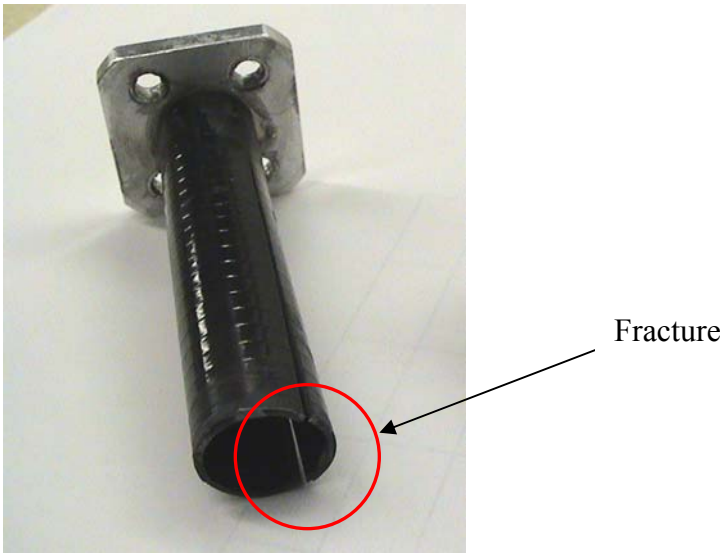

Figure 2.20: Carbon Fiber Longitudinal Fracture

The root cause of the repeated carbon fiber tube failures was investigated. The outside diameter of the aluminum connector plug was measured to determine if sanding had decreased the diameter. A decrease in diameter would increase the gap between the inside of the carbon fiber tube and the epoxy, resulting in a decrease in bond strength. The original connector plug design diameter was 0.427in to create a recommended 0.05in gap between the 0.437in diameter carbon fiber tube [20]. The measured diameter was between 0.428in and 0.430in, so an increased gap size was not the failure cause.

Upon initial inspection of the connector plug, the epoxy coverage around the plug was observed to be non-uniform. One side had a heavy layer of epoxy, while the opposite side had almost no coverage. An example of this coverage problem can be seen in Figure 2.21. This non-uniform coverage was likely the result of application errors and the horizontal drying method used. Over the drying period, the epoxy likely settled onto one side due to gravity, causing the opposite side to have little coverage and bond strength. A new carbon fiber tube was adhered to the connector plug using the same epoxy procedure; however, the tube was dried in a vertical orientation to avoid the non-uniform coverage problems. Also, a generous fillet of epoxy was applied to the base of the tube to prevent cracks from forming at the tube ends. The final assembly was tested multiple times on the leg without incident.

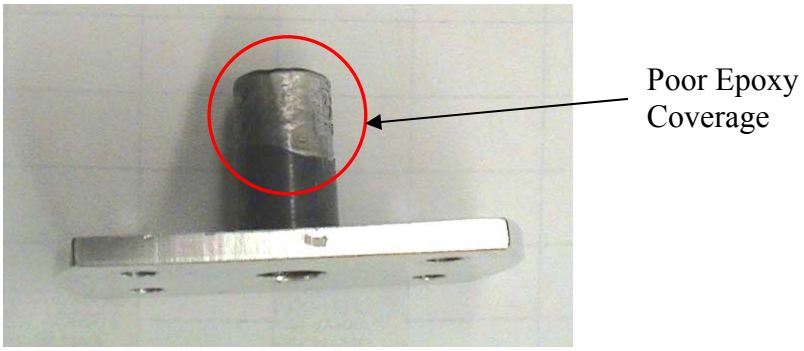

Figure 2.21: Poor Epoxy Coverage on Connector Plug

2.7 Hip Motor Replacement

The hip motor on the prototype leg experienced two distinct mechanical failures over the course of experimentation. The first incident was a bending failure of the output shaft on the hip motor assembly, which is shown in Figure 2.22. This failure occurred because of the high forces on the shaft from the hip motor pulley and the high cable tension. In addition, the location of the hip axis cable crimp contributed to an increased load on the output shaft. The cable crimp would ride up onto the pulley at extreme thigh positions, causing a spike in the cable tension and a spike in the force on the output shaft. These forces acted as a point load on the relatively small diameter shaft causing the output shaft to bend significantly. The hip motor pulley rotation was unbalanced due to the bent shaft.

The hip motor and gear box were replaced with the same model. The hip axis cable was shifted to ensure that the cable crimp did not ride on the pulley throughout the hip joint's range of motion. Also, the addition of the cable tensioning system, detailed in Section 2.5, allowed the hip axis cable tension to be adjusted and ensured that the new motor shaft would not be bent due to high cable tension.

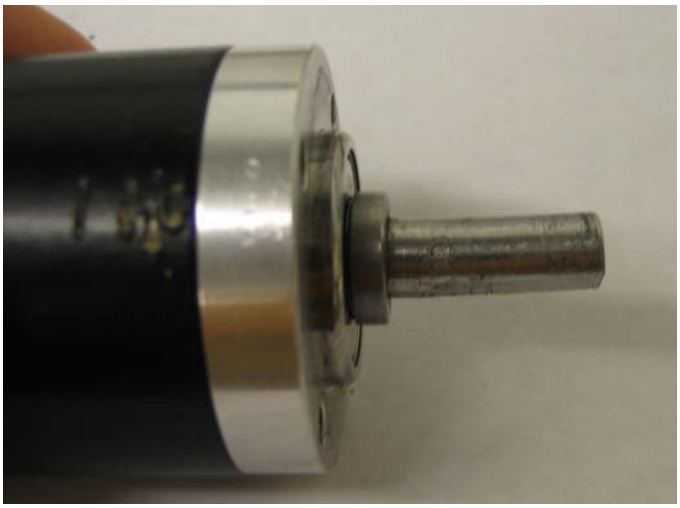

Figure 2.22: Bent Hip Motor Shaft

The second incident resulted in a failure of the motor component of the new hip motor assembly. After a series of jump tests, the thigh was unable to rotate freely and required an uncharacteristically large force to move. In an effort to troubleshoot the problem, the hip motor was removed from the leg and determined to be the source of failure. The output shaft on the motor assembly was unable to rotate while the thigh assembly on the leg hardware was able to swing freely.

The motor was disassembled from the adjoining gear box in an effort to isolate the problem further, which can be seen in Figure 2.23. Once removed from the motor, the gear box was able to rotate freely while the motor remained locked. The motor winding resistances were measured to be 3.8Ω, 3.8Ω, and 0.2Ω for windings 1, 2, and 3, respectively. Each winding should have the same resistance of 5.6Ω, indicating that at least one of the windings had failed. The winding may have overheated due to a faulty motor amplifier and expanded onto the motor's rotor, preventing it from rotating.

The original hip motor still functioned despite the bent shaft on the gear box, so this motor and gear box were also disassembled. The intact gear box was placed on the

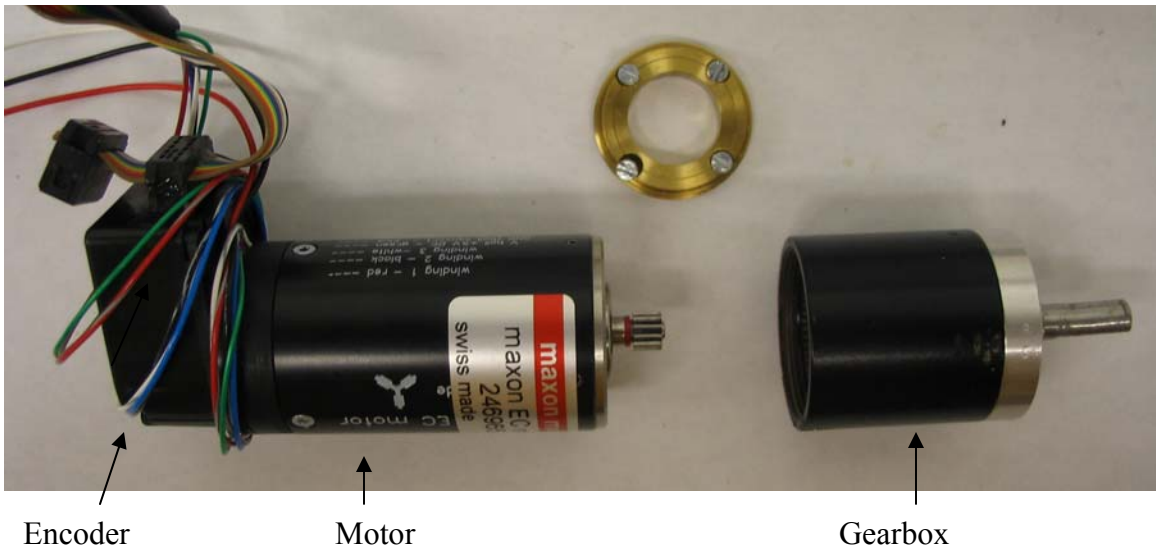

Figure 2.23: Hip Motor Disassembled

functioning motor and assembled back onto the leg. Initially, friction problems were again observed in the newly replaced hip motor, accompanied by a noticeable scraping sound, although the friction in the motor was less pronounced than previously. The source was traced back to the motor encoder on the end of the motor, shown in Figure 2.23. The encoder disk had likely become off center and was rubbing on the inside of the encoder housing. The whole encoder was replaced, and the new encoder disk was readjusted on the motor shaft to avoid the scraping issues. The hip motor was again reassembled onto the leg, this time without incident.

2.8 Results

Experimental jump testing was used to determine the problem areas of the leg's mechanical design and provide a measure of performance improvement. Repeated jump tests were used to quantify the robustness and reliability of the leg hardware. A reliable hardware design would enable the leg to jump continually without failure, and more consecutive jumps correspond to a more robust system. Prior to the hardware improvements, four consecutive jumps were the most the leg achieved. Figure 2.24 shows a plot of the leg's height over the four jumps, measured from the hip axis to the ground. The minimum and maximum height values were inconsistent over the four jumps, indicating control problems with the leg. While some of the problems stemmed from the control algorithms used, much of the error was compounded by the unreliable hardware.

Following the mechanical design improvements, the leg's performance changed dramatically. Figure 2.25 shows a plot of the height data for 15 consecutive jumps. The

maximum height for each jump did not vary considerably, and the body returned to nearly the same position at the bottom of each jump. The uniformity of the jumps indicates that the controllability of the leg had been greatly improved, leading to reliable performance. The resolution of the cable slipping issues, the addition of the knee potentiometer, and the new knee spring hard stop all contributed to improving the controllability of the leg. Additionally, Figure 2.26 shows the highest jump to date, indicating that the leg can jump to greater heights than before without mechanical failure. The highest jump was achieved on the second consecutive jump, and the hip axis reached a maximum height of 16.75in.

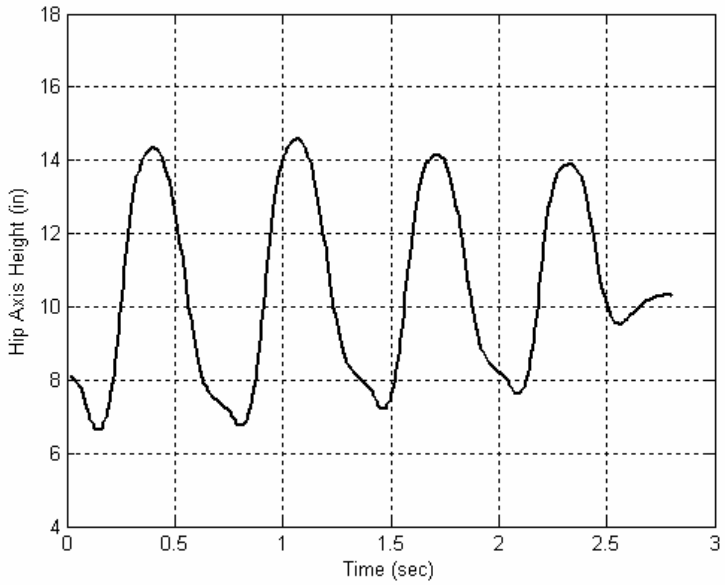

Figure 2.24: Four Consecutive Jumps Prior to Mechanical Improvements

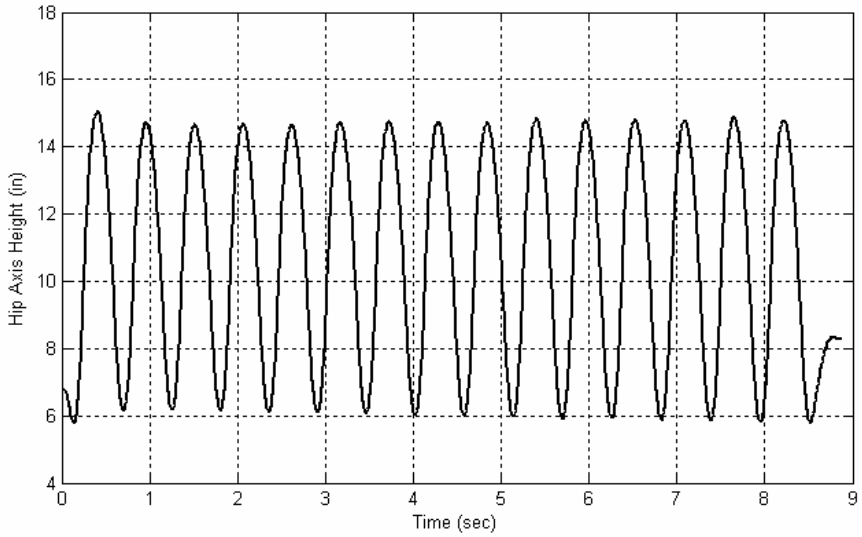

Figure 2.25: 15 Consecutive Jumps After Mechanical Improvements

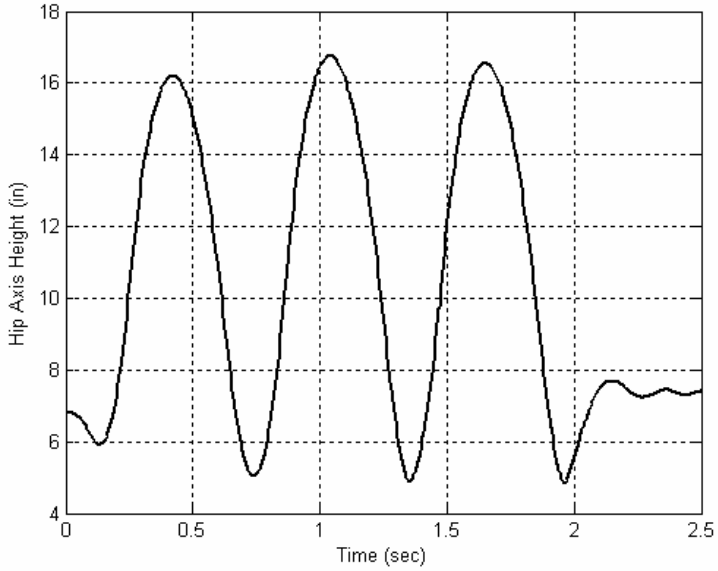

Figure 2.26: Highest Jump Achieved After Mechanical Improvements

2.9 Summary

This chapter details the mechanical design modifications made to the leg hardware to improve the leg's reliability and performance. Three design modifications addressed issues with the leg hardware that prevented reliable and accurate position control. The addition of cable crimps in the pulleys eliminated cable slippage. The

addition of a knee potentiometer allowed the exact angular position of the shank to be known, and the knee spring hard stop system eliminated unwanted slop in the knee joint. Three other design modifications addressed mechanical failures and improved the robustness of the design. The addition of a cable tensioning system greatly improved assembly of the leg and eliminated bearing failures during assembly. The carbon fiber tube in the thigh and the hip motor were both replaced upon failure. The contributions of these mechanical modifications to the leg's performance were quantified through experimentation with an increase in the number of consecutive jumps the leg could achieve.

CHAPTER 3

PROTOTYPE LEG JUMPING ANALYSIS

3.1 Introduction

A detailed analysis of the prototype leg's electrical and mechanical systems would provide insight and understanding into the leg's operation and help improve the hardware's performance. Several jumping models of the prototype leg had already been developed, of which Simon Curran's dynamic simulation was the most notable. The simulation was based on the analytical dynamic equations describing the electrical actuators and the mechanical hardware. However, because of the complexity of the entire system, time-based numerical integration methods were used to determine solutions to the dynamic equations instead of an analytical solution. This method was convenient for solving a complex dynamic system, but the fundamental understanding of the system's operation that an analytical solution method could provide was lost in the process.

A portion of this research work was dedicated to developing a simplified analytical model of the prototype leg hardware that could be used to characterize the system's jumping performance. Specifically, the analytical model was used to investigate how the foot position of the leg affects the leg's total jumping height. An analytical model would require less computational power because no time-based numeric integration would be needed. This model could be particularly advantageous in simplifying a genetic optimization algorithm because of the reduced computational load.

Also, the analytical solution to this model would provide an intuitive understanding of the leg's operation over a range of operating conditions, which could be helpful in creating fuzzy control algorithms.

The analysis focused primarily on modeling the leg during the power stroke of a jump. The power stroke is defined as the thrust phase of a jump from the initiation of upward motion until takeoff, over which the motors input power into the system. A static force analysis was incrementally performed over the leg's power stroke and used to determine the ground reaction forces on the foot that contributed to vertical motion. The reaction forces were used to calculate the total energy input into the leg and the corresponding maximum jumping height that the leg would reach for a specific jump. The jumping height was measured from the ground to the hip axis. The starting foot position was varied to find an optimal location that would yield the highest jump.

The following chapter details the structure of the analytical model and presents some results generated from the model. The basic kinematic model of the leg is presented in Section 3.2. Sections 3.3 and 3.4 detail the input torque determination and ground reaction force determination, respectively. The takeoff criterion is presented in Section 3.5, and the jumping height analysis is presented in Section 3.6. Finally, a summary is presented in Section 3.7. The model was formulated into a MATLAB script that can be found in Appendix B under the name LegAnyl.m. The following discussion of the model closely follows the MATLAB code, and a table of variable comparisons can also be found in Appendix B.

3.2 Kinematic Model

The basis of the analytical model was a kinematic model developed to represent the actual leg hardware. During the power stroke, the leg can be modeled as a simple slider-crank mechanism if the foot is assumed not to slip and the foot radius is neglected. Figure 3.1 shows an overlay of a slider-crank model on a photograph of the hardware system. Since the body is constrained to a linear motion with the rails, the body is the slider, and the vertical rails are the sliding path. The thigh and shank would then be the coupler and crank, respectively. The foot contact would be considered a revolute joint between the crank and the frame, or the ground.

However, the actual kinematic model used in the analysis was an inversion of this slider-crank model, shown in Figure 3.2. The reference frame was placed on the moving body at the hip axis instead of on the ground at the foot. In this case, the body of the leg

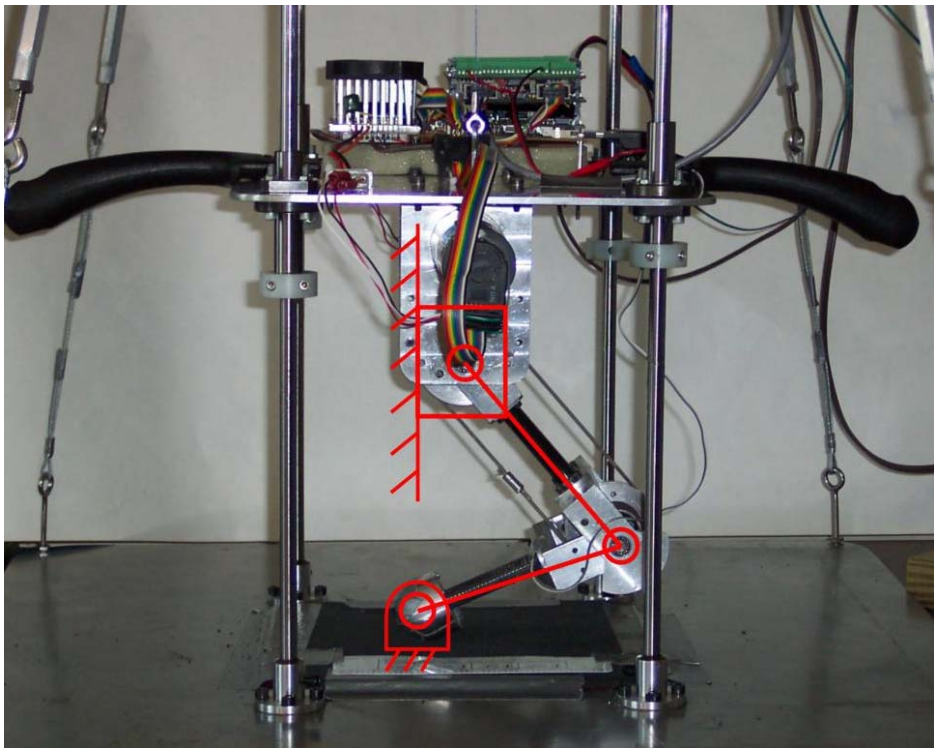

Figure 3.1: Slider-Crank Overlay on Hardware

was considered the frame with the thigh attached at the hip axis with a revolute joint. The thigh was then considered the crank, and the shank was considered the coupler. The foot slid along the vertical sliding path in the same manner that the body moved in the previous model. The ground reaction forces at the foot could be more easily determined by making the foot the end-effecter of the mechanism instead of the body, as in the previous kinematic model. For the analysis, the vertical foot position would be incremented away from the hip to represent the power stroke of a jump.

Development of this kinematic model was important because almost every component of the analytical model used the geometric parameters described in the kinematic model. The knee and hip joint angles at any given position of the power stroke were calculated from the model using inverse kinematics. The joint angles and the

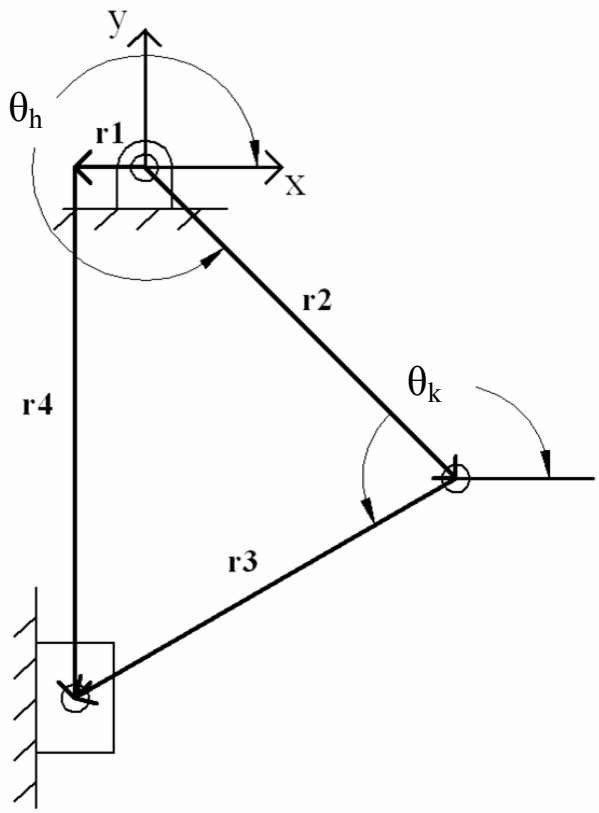

Figure 3.2: Slider-Crank Model Used in Analysis

kinematic model were also used in determining the Jacobian matrix, which was fundamental for developing the static force analysis for the leg.

3.2.1 Inverse Kinematics

The inverse kinematics of the slider-crank model was used to calculate the joint angles of the leg at each position of the power stroke. The inverse kinematics was formulated based on a method to analyze slider-crank mechanisms [21]. To begin the derivation of the analytical equations, a vector loop is set up on the slider-crank model as shown in Figure 3.2. The vector loop equation for the slider-crank is

$$\mathbf{r}_2 + \mathbf{r}_3 = \mathbf{r}_1 + \mathbf{r}_4. \tag{3.1}$$

The vector equation is expanded into component equations. The hip and knee angles are measured from the horizontal and are denoted by θ_h and θ_k, respectively. The magnitude of the vectors $\mathbf{r}_2$ and $\mathbf{r}_3$ represent the length of the thigh and shank, respectively. The vector $\mathbf{r}_1$ is simply the x coordinate of the foot, and $\mathbf{r}_4$ is the y coordinate of the foot. Expanding and simplifying Equation 3.1 yields

$$r_2 \cos\theta_h + r_3 \cos\theta_k = x \tag{3.2}$$

and

$$r_2 \sin\theta_h + r_3 \sin\theta_k = y. \tag{3.3}$$

Equations 3.2 and 3.3 are combined, rearranged to eliminate θ_k, and simplified as

$$A\cos\theta_h - B\sin\theta_h + C = 0 \tag{3.4}$$

where,

$$\begin{aligned} A &= -2xr_2 \\ B &= -2yr_2 \\ C &= x^2 + y^2 + r_2^2 - r_3^2. \end{aligned} \tag{3.5}$$

Using trigonometric half-identities to solve Equation 3.4, the hip angle is

$$\theta_h = 2\tan^{-1}\left[\frac{-B+\sqrt{B^2-C^2+A^2}}{2(C-A)}\right]. \tag{3.6}$$

The addition sign is chosen for the quadratic component of Equation 3.6 so that θ_h will result in an angle greater than 180°. Substituting θ_h into Equations 3.2 and 3.3, the knee angle is calculated by

$$\theta_k = \tan^{-1}\left[\frac{y-r_2\sin\theta_h}{x-r_2\cos\theta_h}\right]. \tag{3.7}$$

The inputs to the inverse kinematic equations are the *x* and *y* coordinates of the foot. In the MATLAB function, these values are passed to the equations from the jumping loop and the foot offset loop, which is discussed in Section 3.6.

3.2.2 Jacobian Determination

The Jacobian matrix was necessary for performing the static force analysis on the leg at each increment of the power stroke. The Jacobian is the basis for determining the manipulability ellipse, which was one method used as a static force analysis detailed in Section 3.4. More importantly, the ground reaction forces $\mathbf{F}_g$ on the foot are related to the joint torques $\boldsymbol{\tau}$ by

$$\boldsymbol{\tau} = J^T\mathbf{F}_g, \tag{3.8}$$

where *J* denotes the Jacobian matrix.

An expression for the Jacobian was determined using the fundamental relationship that the Jacobian relates the velocity of the end-effecter, or foot, to the joint velocities by

$$\begin{bmatrix} \dot{x} \\ \dot{y} \end{bmatrix} = J \begin{bmatrix} \dot{\theta}_h \\ \dot{\theta}_k \end{bmatrix}. \tag{3.9}$$

The relationship between the joint velocities and foot velocity can be found from the vector loop equations derived in Section 3.2.1. Differentiating Equations 3.2 and 3.3 with respect to time yields

$$-r_2\dot{\theta}_h \sin\theta_h - r_3\dot{\theta}_k \sin\theta_k = \dot{x} \tag{3.10}$$

and

$$r_2\dot{\theta}_h \cos\theta_h + r_3\dot{\theta}_k \cos\theta_k = \dot{y}. \tag{3.11}$$

After writing Equations 3.10 and 3.11 in matrix form, the Jacobian matrix can be extracted as

$$J = \begin{bmatrix} -r_2 \sin\theta_h & -r_3 \sin\theta_k \\ r_2 \cos\theta_h & r_3 \cos\theta_k \end{bmatrix}. \tag{3.12}$$

The inverse kinematics for the slider-crank model was necessary to develop because Equation 3.12 shows that the Jacobian is a function of the hip and knee angles.

3.3 Input Torque Determination

The input torques had to be determined for use in the static force analysis of the leg. According to Equation 3.8, the ground reaction forces on the foot are directly related to the input torques, or joint torques, through the Jacobian matrix. The hip and knee motors provide the input torques to the leg at their respective joints. This section describes two simplified methods used in the analysis to model the motor torques produced during the power stroke of a jump. The first method is a saturated motor torque model that assumes the motor torque is constant over the entire power stroke. The

second method builds upon the saturated motor torque model using a torque/leg-length curve in an attempt to more accurately model the dynamics of the motors in a simple analytical fashion. Also, a gravitational torque penalty was used to address the mass of the thigh and shank.

3.3.1 Saturated Motor Torque

The saturated motor torque model is a simplified motor model used to determine the input torques at the hip and knee joints. The model assumes that the torques available from the motors are constant over the entire power stroke. The maximum torque τ_{sat} produced by the hip or knee motor at the respective joint is given by

$$\tau_{sat} = I_m k_T n_g e_g. \tag{3.13}$$

Equation 3.13 was derived from the standard DC motor torque equation, where k_T is the motor torque constant, n_g is the ratio of the integrated gear box, and e_g is the gear box efficiency. The motor current I_m is assumed to be at the maximum allowable operating level for each motor as specified in the product datasheets. Table 3.1 shows the values used for each parameter and motor in the analysis. On the hardware system, the motors are commanded the maximum allowable current during the power stroke of a jump. However, because the motors and the leg are a dynamic system, the actual output torque for each motor is not necessarily the maximum, or steady state, torque τ_{sat}.

Table 3.1: Motor Torque Parameters

Parameter	Hip Motor	Knee Motor
I_m	7.5 A	10 A
k_T	0.04 N-m/A	0.043 N-m/A
n_g	33	66
e_g	0.75	0.72
τ_{sat}	7.43 N-m	20.4 N-m

3.3.2 Torque/Leg-Length Model

The assumption that the motor produces a constant torque over the entire power stroke is unrepresentative of the physical system. As the body of the leg accelerates through the power stroke, the rotational joint velocities also increase. The motor speeds must increase to keep up with the expanding leg. Because of the torque-speed relationship of a DC motor, the motor output torque drops with this increase in joint speed through the power stroke. The saturated torque model fails to capture these dynamic characteristics of the actual hardware.

A new motor model was created based on the torque-speed relationship of the DC motors to capture the system dynamics in a simplified analytical form. However, since the motor and joint velocities are not part of the analysis, the motor speed is related to the virtual leg length, which is the minimum distance between the hip axis and the foot. As the leg expands during the power stroke and the virtual leg length increases, the joint and motor velocities also increase comparatively. The motor torque is assumed to be maximum at the initial virtual leg length and to linearly decrease to zero at the takeoff virtual leg length, similar to the trend of a torque-speed curve.

The simple linear relationship between virtual leg length and motor torque was not enough to capture the entire motor dynamics, so the model was modified slightly. The motor torques decreased too rapidly from the initiation of the jump, drastically reducing the maximum jumping height of the leg. The motor torque is assumed to be saturated for a percentage of the virtual leg length and then to decrease linearly to zero at the takeoff virtual leg length. Figure 3.3 shows a generic torque/leg-length curve used for

each motor in the analysis. The virtual leg length l_v at each leg position throughout the power stroke is calculated by

$$l_v = \sqrt{x^2 + y^2}. \tag{3.14}$$

The initial leg length l_i is found using Equation 3.14 and the initial foot position. The determination of takeoff leg length l_t is discussed in detail in Section 3.5. The cutoff leg length l_c is the leg length at which the saturation shelf ends,

$$l_c = n_c(l_t - l_i) + l_i, \tag{3.15}$$

where n_c is the percentage of torque saturation. The resulting relationship for the maximum torque τ_{max} available at the joints is a piecewise linear function

$$\tau_{max} = \begin{cases} \tau_{sat} & , \ l_i \le l_v \le l_c \\ \dfrac{\tau_{sat}}{l_t - l_s}(l_t - l_v) & , \ l_c < l_v \le l_t \end{cases}. \tag{3.16}$$

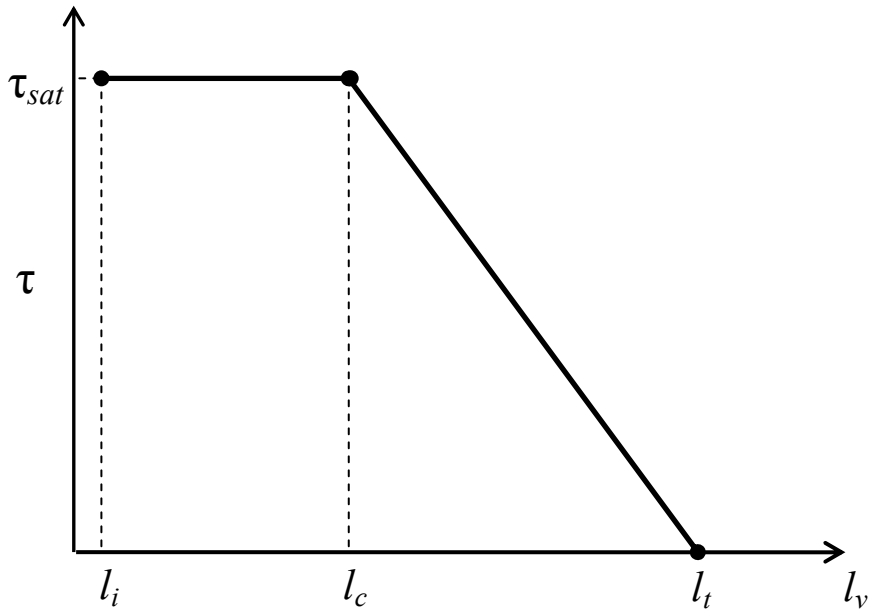

Figure 3.3: Generic Torque/Leg-Length Curve

The torque/leg-length curves are calculated automatically in the code for each initial foot position used in the analysis. The best torque saturation percentage n_c was determined for each motor by comparing the results of the analysis to the results of Simon Curran's dynamic simulation. More detail on the results is presented in Chapter 4.

3.3.3 Gravitational Torque Penalty

A gravitational torque penalty was used in the model to account for the input energy required to move the leg masses through the power stroke. The leg is assumed to be jumping upward against gravity, so a portion of the maximum available torque τ_{max} at the joints is used to counter the weight of the leg links. This gravitational torque penalty τ_g is the torque required at each joint to keep the leg statically stable in a given position during the power stroke. Figure 3.4 shows the free body diagram of the leg in a general position used to derive the gravitational torque penalty. The force due to gravity is applied at the center of mass on each leg link, and the resulting torques at each joint are determined by

$$\begin{bmatrix} \tau_{g,hip} \\ \tau_{g,knee} \end{bmatrix} = \begin{bmatrix} m_t l_{ct} \cos\theta_h + m_s (r_2 \cos\theta_h + l_{cs} \cos\theta_k) \\ m_s l_{cs} \cos\theta_k \end{bmatrix} g. \tag{3.17}$$

The mass of the thigh and shank are denoted by m_t and m_s, and l_{ct} and l_{cs} represent the position of the center of mass for each link. The values used for the gravitational parameters are shown in Table 3.2. The actual torque τ_{act} available at each joint to produce upward movement is given by

$$\tau_{act} = \tau_{max} - \tau_g. \tag{3.18}$$

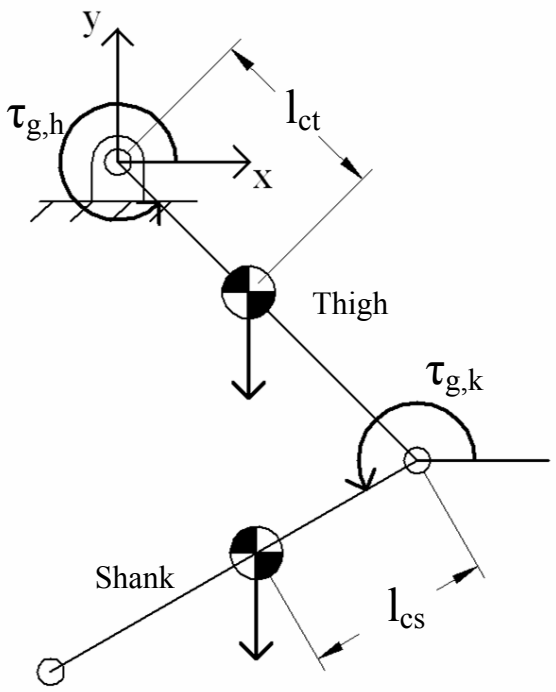

Figure 3.4: Free Body Diagram of Leg Links

The ground reaction forces in the static force analysis were calculated using the modified joint torque τ_{act}. The energy required to move the mass of the body upward during the power stroke was accounted for separately and is discussed in Section 3.6.

Table 3.2: Gravitational Torque Parameters

Parameter	Thigh	Shank
m	0.328 kg	0.431 kg
l_{cg}	0.0715 m	0.0303 m
$r_{2,3}$	0.1397 m	0.1397 m

3.4 Ground Reaction Force Determination

Determining the reaction forces acting on the foot during the power stroke was the central element in the static force analysis and the entire analytical model. The ground reaction forces were used to determine the energy input that contributed to upward movement of the leg and the total jumping height of the leg, which is discussed in Section 3.6. In general, the reaction forces were assumed to be due to the torques

applied at the hip and knee joints driving the foot into the ground. The actual reaction forces on the foot were calculated using three different methods to compare their effectiveness. The first method was a straight-forward force determination using the actual joint torques calculated previously. The second method used a concept called the manipulating force ellipse, and the third method attempted to find a torque profile that would produce only a vertical reaction force at the foot.

3.4.1 Maximum Torque

The first ground reaction force determination assumed that the maximum available torque was supplied to each joint. In relation to the actual hardware, this force analysis is comparable to providing full current to the motors without any type of altered current profile. The horizontal and vertical components F_x and F_y of the ground reaction forces are calculated using the Jacobian,

$$\begin{bmatrix} F_x \\ F_y \end{bmatrix} = \left(J^T\right)^{-1} \begin{bmatrix} \tau_{hip} \\ \tau_{knee} \end{bmatrix}. \tag{3.19}$$

The torques available at each joint, τ_{hip} and τ_{knee}, are either τ_{act} or τ_{sat} depending on whether the saturated motor model or the torque/leg-length motor model is being employed.

3.4.2 Manipulating Force Ellipse

A concept known as the manipulating force ellipse was utilized in the second method to determine the ground reaction forces at the foot. Yoshikawa developed the manipulability ellipse and manipulating force ellipse to determine the best posture for a robotic manipulator in the workspace [22]. This concept was expanded to determine the best joint torques for a given posture and applied force to the robotic manipulator. For a two-joint mechanism, such as the leg, the manipulating force ellipse provides a measure

of all the possible end-effecter forces such that the norm of the joint torques is less than or equal to one. Minimizing the joint torques provides a motivation to pursue the manipulating force ellipse because it increases the efficiency of the leg.

The manipulating force ellipse was used to develop joint torque profiles for the power stroke that provided the highest vertical jump. Figure 3.5 shows a general manipulating force ellipse as determined for the leg setup. The foot is considered the end-effecter for the leg, and the manipulating force ellipse is a measure of the possible ground reaction forces on the foot. Joint torques, τ_{hip} and τ_{knee}, are calculated from the ground reaction force F with the largest vertical component to provide the maximum vertical thrusting force for the leg.

The Jacobian is used to find the manipulating force ellipse. However, the Jacobian must be normalized by the maximum allowable torque for each joint to ensure

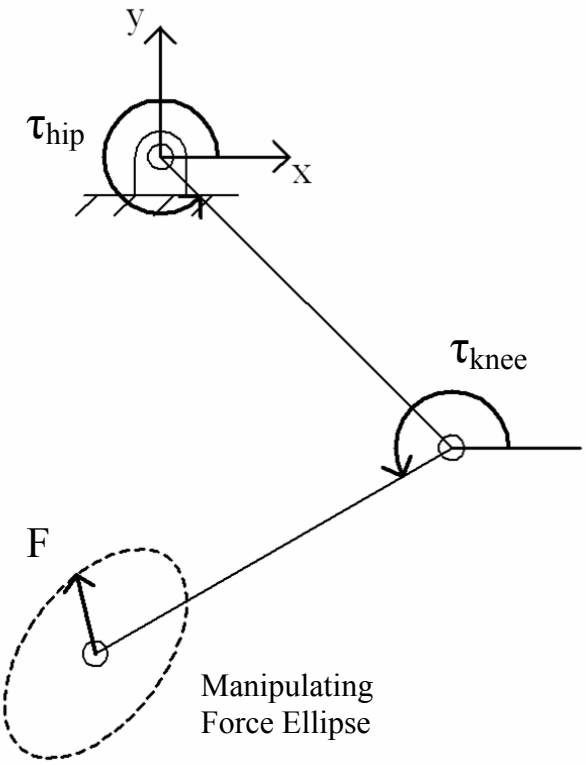

Figure 3.5: Manipulating Force Ellipse on the Leg

that no joint exceeds the torque limit of its motor. The normalized Jacobian $\hat{J}$ is given by

$$\hat{J}^T = \begin{bmatrix} \tau_{hip}^{-1} & 0 \\ 0 & \tau_{knee}^{-1} \end{bmatrix} J^T, \tag{3.20}$$

where τ_{hip} and τ_{knee} are either τ_{act} or τ_{sat} depending on the motor model. The eigenvalues of matrix $\hat{J}^T\hat{J}$ are related to the principal axes of the manipulating force ellipse, and the eigenvectors give the direction of the principal axes. The general equation of an ellipse is

$$1 = \frac{X^2}{a^2} + \frac{Y^2}{b^2}. \tag{3.21}$$

The variables *a* and *b* are half the length of the principal axes and are related to the eigenvalues by

$$a = \sqrt{D_{11}} \tag{3.22}$$

and

$$b = \sqrt{D_{22}}, \tag{3.23}$$

where *D* is a two-by-two matrix of the eigenvalues.

The ground reaction force with the largest vertical component corresponds to a force vector from the center of the ellipse to a point on the ellipse at which the tangent is a horizontal line. Figure 3.6 shows a diagram of the manipulating force ellipse oriented at an angle ϕ from the x-axis. The orientation angle ϕ is given by

$$\tan\phi = \frac{V_{21}}{V_{11}}, \tag{3.24}$$

where *V* is a two-by-two matrix of the eigenvectors. The point P corresponds to the point on the ellipse at which the ellipse is tangent to the horizontal in the x-y coordinate frame. However, P must be found in the X-Y coordinate frame because Equation 3.21 is

specified in this frame. The coordinates of the point P can be found by equating the slope of a line at an angle $-\phi$ from the X-axis to the slope of the ellipse at P. Differentiating Equation 3.21 gives the slope of the ellipse as

$$\frac{dX}{dY} = \frac{-b^2 P_X}{a_2 P_Y} = \tan(-\phi). \tag{3.25}$$

The coordinates P_X and P_Y are found by combining Equations 3.21 and 3.25,

$$P_X = \frac{a^2 \tan\phi}{\sqrt{a^2 \tan\phi + b^2}} \tag{3.26}$$

and

$$P_Y = \frac{b^2}{\sqrt{a^2 \tan\phi + b^2}}. \tag{3.27}$$

The coordinates of P are transposed into the standard x-y coordinate frame of the analysis by

$$\begin{bmatrix} P_x \\ P_y \end{bmatrix} = \begin{bmatrix} \cos\phi & -\sin\phi \\ \sin\phi & \cos\phi \end{bmatrix} \begin{Bmatrix} P_X \\ P_Y \end{Bmatrix} + \begin{bmatrix} x \\ y \end{bmatrix}. \tag{3.28}$$

The ground reaction forces F_{xm} and F_{ym} are calculated from the transposed coordinates of point P as

$$\begin{bmatrix} F_{xm} \\ F_{ym} \end{bmatrix} = \begin{bmatrix} P_x - x \\ P_y - y \end{bmatrix}. \tag{3.29}$$

The joint torques τ_{hm} and τ_{km} required to produce the ground reaction forces are back calculated using the unscaled Jacobian matrix J and Equation 3.8. The ground reaction forces F_{xm} and F_{ym} are then used to determine the jumping height of the leg based on the torque profile for each joint given by τ_{hm} and τ_{km}.

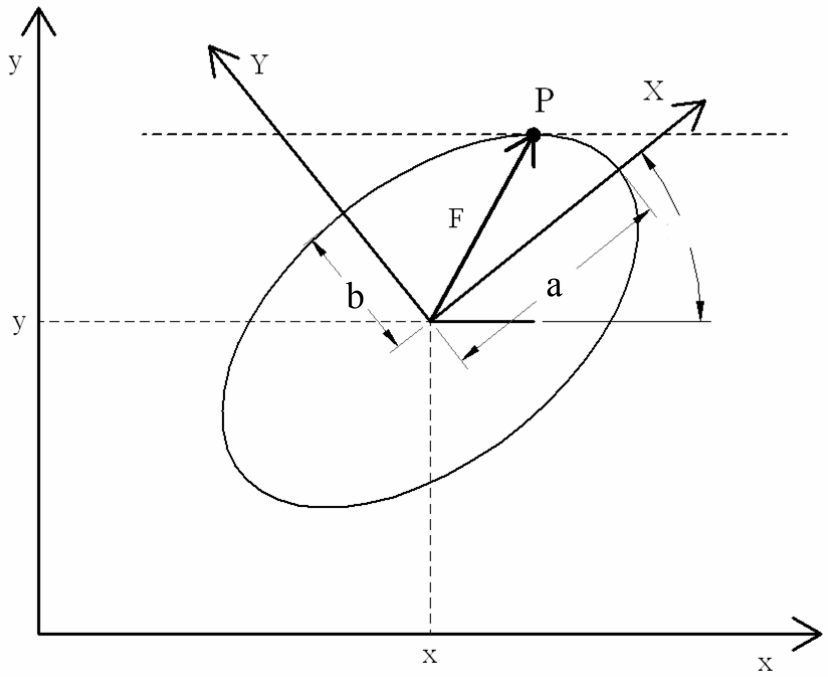

Figure 3.6: Force Determination from Manipulating Force Ellipse

3.4.3 Vertical – Only Force

The third force determination was used to develop a torque profile for each joint that would produce only a vertical reaction force at the foot throughout the entire power stroke. The horizontal component of the reaction force drives the body of the leg into the supporting rails. By eliminating the horizontal reaction force, the sliding friction in the rails can be significantly reduced, possibly yielding a higher jump.

To begin deriving the torque profiles for each joint, Equation 3.8 is expanded into its components

$$\tau_{hip} = J_{11}F_x + J_{21}F_y \tag{3.30}$$

and

$$\tau_{knee} = J_{12}F_x + J_{22}F_y. \tag{3.31}$$

The horizontal force F_x goes to zero, and Equations 1.30 and 1.31 can be simplified and combined into

$$K_T = \frac{\tau_{hip}}{\tau_{knee}} = \frac{J_{21}}{J_{22}} = \frac{r_2 \cos\theta_h}{r_3 \cos\theta_k}. \tag{3.32}$$

Equation 3.32 shows that for a given leg position, there is a specific joint torque ratio that will produce only a vertical reaction force at the foot. This ratio of the hip torque to the knee torque is defined as K_T.

A simple algorithm was created to determine the actual joint torques from K_T without exceeding the allowable motor torques. The knee torque τ_{kr} is set equal to the maximum allowable joint torque, either τ_{act} or τ_{sat} depending on the motor model. The hip torque τ_{hr} is calculated by

$$\tau_{hr} = K_T \tau_{kr}. \tag{3.33}$$

The resulting hip torque τ_{hr} is compared to the maximum allowable joint torque for the hip based on the motor model. If τ_{hr} exceeds the allowable joint torque, τ_{hr} is set equal to the maximum allowable joint torque. The new knee torque τ_{kr} is then calculated by

$$\tau_{kr} = \frac{\tau_{hr}}{K_T}. \tag{3.34}$$

The vertical reaction force F_y at the foot is then solved for using either Equation 3.30 or 3.31.

3.5 Takeoff Determination

A parameter for quantifying the end of the power stroke had to be created for the analytical model to accurately represent the physical system. The takeoff point was considered the point when the foot left the ground, thereby ending the power stroke and

energy input to the leg. An accurate takeoff parameter was important because stopping the power stroke short would reduce the total energy input to the leg and result in an underestimate of the jumping height. Conversely, if the power stroke was longer than in the physical system, the model would predict an overestimate of the leg's jumping height. The initial takeoff parameter used was a constant force criterion. The takeoff parameter was eventually invalidated by comparison to a dynamic simulation of the leg and ultimately changed to a constant leg length criterion.

3.5.1 Constant Force Takeoff

The initial parameter used for determining the leg's takeoff point was a constant force criterion. The leg was considered to have lifted off the ground once the vertical reaction force on the foot exceeded a constant threshold regardless of the foot's position. The criterion was based on the assumption that the acceleration of the foot at liftoff was equal to the acceleration due to gravity in the upward direction. Initially, the force threshold was twice the weight of the leg, 39 N, which would result in an upward acceleration of the body equal to that of gravity when the body was placed in a gravitational field. This initial takeoff force, however, was lower than the ground reaction forces for all of the force determination methods, erroneously implying that the leg had lifted off almost instantaneously. This result indicated that there was a fundamental error with the constant force takeoff criterion.

3.5.2 Simulation Comparison

A dynamic simulation of the leg was used to investigate the constant force takeoff criterion and to compare it to other possible takeoff parameters. The simulation was developed by Simon Curran, and a modified version of the code can be found in

Appendix B. The goal of the simulation investigation was to compare several takeoff parameters and find the most consistent parameter over a range of foot positions. The three possible takeoff parameters were the body velocity relative to the foot at takeoff, the vertical ground reaction force at takeoff, and the virtual leg length at takeoff. The parameters were chosen because they could be incorporated into the existing model.

The exact instant of liftoff in the simulation was ambiguous, mainly because of the tradeoff between a reasonable integration step and the accuracy of the simulation. Also, the spring-damper ground contact model utilized by the simulation created additional ambiguities because the spring and damping constants for the actual system were not known. Four different takeoff instances were compared for each takeoff parameter.

The first takeoff instant was when the body's kinetic energy was maximum, which indicating that the motors were no longer supplying energy to the leg and the power stroke had ended. The second takeoff instant occurred when the foot acceleration exceeded gravitational acceleration, which comes from the constant force criterion. The third takeoff instant occurred when the foot velocity equaled zero, which indicated that the foot had reversed direction on the ground spring and was beginning to travel upward. The last takeoff instant was when the ground reaction force went to zero, which indicated the foot was no longer in contact with the ground spring.

The average, maximum, and minimum values of the three possible takeoff parameter values were recorded from the simulation at all four takeoff instances over a range of 20 foot positions. To quantify which parameter was most consistent, the minimum and maximum percent deviation from the average value were computed by

$$\%_{dev} = \frac{\left| x_{max,min} - x_{avg} \right|}{x_{avg}} * 100. \tag{3.35}$$

The standard deviation was also calculated for each takeoff parameter. Table 3.3 shows the results for the body velocity takeoff parameter. Table 3.4 shows the results for the ground reaction force takeoff parameter, and Table 3.5 shows the results for the virtual leg length takeoff parameter. Based on these results, the virtual leg length parameter proved the most consistent, specifically for the takeoff instant when the foot force went to zero. The largest deviation was only 1.23% from the average leg length of 0.272m, and the standard deviation of the results was only 0.473% of the average. The deviations were by far the lowest for all the takeoff parameters, prompting the adoption of the virtual leg length parameter as the new takeoff criterion.

Table 3.3: Body Velocity Takeoff Parameter

Takeoff Instant	Max Body Energy	Foot Accel = g	Foot Vel = 0	Foot Force = 0
Average Velocity (m/s)	1.63	1.71	1.61	1.37
Max Deviation %	18.8 %	16.6 %	11.2 %	18.8 %
Min Deviation %	8.16 %	7.28 %	5.95 %	8.35 %
Std Deviation %	8.37 %	7.53 %	4.60 %	8.02 %

Table 3.4: Ground Reaction Force Takeoff Parameter

Takeoff Instant	Max Body Energy	Foot Accel = g	Foot Vel = 0	Foot Force = 0
Average Force (N)	61.1	119	132	-0.688
Max Deviation %	17.7 %	2.09 %	9.59 %	165 %
Min Deviation %	23.2 %	4.28 %	10.4 %	98.7 %
Std Deviation %	11.4 %	1.54 %	6.28 %	65.3 %

Table 3.5: Virtual Leg Length Takeoff Parameter

Takeoff Instant	Max Body Energy	Foot Accel = g	Foot Vel = 0	Foot Force = 0
Average Leg Length (m)	0.265	0.246	0.233	0.272
Max Deviation %	1.06 %	1.95 %	5.56 %	0.533 %
Min Deviation %	2.53 %	3.67 %	9.41 %	1.23 %
Std Deviation %	0.938 %	1.59 %	4.36 %	0.473 %

The ambiguity of the takeoff instant in the simulation caused concern about the accuracy of the previous results. Simon Curran developed a new, simplified simulation that does not include a spring-damper ground model and, thus, has one specific takeoff instant. The same three takeoff parameters were investigated using this newer model in the same manner as before, and the modified simulation code is available in Appendix B. Table 3.6 shows the results from the new takeoff parameter investigation. The results confirm the findings from the previous simulation, with the virtual leg length being the most consistent parameter to indicate takeoff. The largest deviation of the virtual leg length at takeoff was 0.268% from the average value of 0.274 m.

As the leg approaches singularity, large changes in joint angles are needed to produce a small change in the virtual leg length. The motor speeds cannot keep up with the increasing joint velocities of the expanding leg, so the leg takes off from the ground. This instant likely occurs at approximately the same virtual leg length near singularity regardless of the orientation of the leg with respect to the ground plane, which is why the virtual leg length parameter is a good takeoff prediction parameter. The virtual leg length was implemented as the takeoff parameter in the model by limiting the extension of the leg to the average value recorded from the simulation.

Table 3.6: Updated Simulation Takeoff Parameters

	Virtual Leg Length (m)	Ground Reaction Force (N)	Body Velocity (m/s)
Average Value	0.274	193	2.76
Max Deviation %	0.268 %	5.82 %	8.04 %
Min Deviation %	0.199 %	13.8 %	20.4 %
Std Deviation %	0.171 %	5.38 %	9.71 %

3.6 Jumping Height Analysis

The overall goal of the analytical model was to determine the jumping height of the leg for any given foot position and starting height. The model was set up in two distinct programming loops separated into individual Matlab functions. The Jumping Loop is the base function that iterates through one power stroke of the leg and outputs the maximum height reached for the jump. The Foot Offset Loop calls the Jumping Loop function over a range of foot positions and a constant starting height. Both script files can be found in Appendix B. The Jumping Loop function is named LegAnyl.m, and the Foot Offset Loop is named Sim_Loop.m.

3.6.1 Jumping Loop

The Jumping Loop increments the leg through the power stroke to determine the maximum height reached for a single jump. The initial starting height of the leg and the foot position are passed from the Foot Offset Loop to the Jumping Loop. The joint angles and the Jacobian are calculated from the kinematic model, and the joint torques are calculated from the motor models. From there, the ground reaction forces are determined according to the three specified models. The leg's height is incremented by 1.0mm, and all the model parameters are calculated again until the leg's virtual leg length reaches the takeoff leg length.

The jumping height for each ground reaction force determination is calculated using an energy method. All of the energy contributing to vertical motion is assumed to result from the vertical reaction force F_y at the foot acting over the distance of the jumping height y. The maximum kinetic energy of the leg E_{max} occurs at the takeoff instant and is

$$E_{max} = \int F_y dy. \tag{3.36}$$

The trapezoidal numerical integration method was used to compute E_{max}. The actual kinetic energy of the leg E_{act} at the takeoff instant is less than E_{max} because a penalty for moving the leg's body upward through a gravitational field is applied. The actual available kinetic energy of the leg for vertical motion is given by

$$E_{act} = E_{\max} - m_b g(y_t - y_i). \tag{3.37}$$

The maximum jumping height y_{max} is assumed to be the point where all of the leg's kinetic energy has converted to potential energy,

$$y_{max} = \frac{E_{act}}{(m_b + m_t + m_s)g} + y_t. \tag{3.38}$$

The maximum jumping heights are calculated for all three ground reaction force determinations and passed back to the Foot Offset Loop.

3.6.2 Foot Offset Loop

The Foot Offset Loop is used to determine the maximum jumping height of the leg for an initial starting height and a range of foot positions. The initial starting height y_i and the foot offset position x are passed to the Jumping Loop function. Two different methods were used to select the initial starting height. The first method assumes that the vertical height of the hip axis is the same for each foot position, or that y_i is constant. The second method assumes that the initial virtual leg length is constant, which results in varying y_i. The loop iterates over a range of foot offset positions, most commonly from -10cm to +10cm away from the center position under the hip axis. The maximum jumping height of the leg is then sent back to the Foot Offset Loop for data collection.

The initial height calculation for the constant initial virtual leg length must be representative of the physical system. The virtual leg length cannot remain constant over the entire range of foot positions, as seen in Figure 3.7. If the foot is a large distance behind the center position, the knee drops below the ground plane. If the foot is a large distance in front of the center position, the thigh exceeds the hard stop limits on the hip axis.

As shown in Figure 3.8, the initial height calculation was split into three spans: the backward span, the forward span, and the intermediate span. The initial virtual leg length is defined by θ_i, the angle of the shank relative to the thigh. The leg is in the backward span when the foot position is far enough behind the hip axis to cause the shank to become horizontal. The condition for this span is

$$x < r_2 \cos\theta_i - r_3. \tag{3.39}$$

The shank remains horizontal for all foot positions within this span, and the initial height is

$$y_i = \sqrt{r_2^2 - (r_3 + x)^2}. \tag{3.40}$$

The leg is considered to be in the forward span when the foot position is far enough in

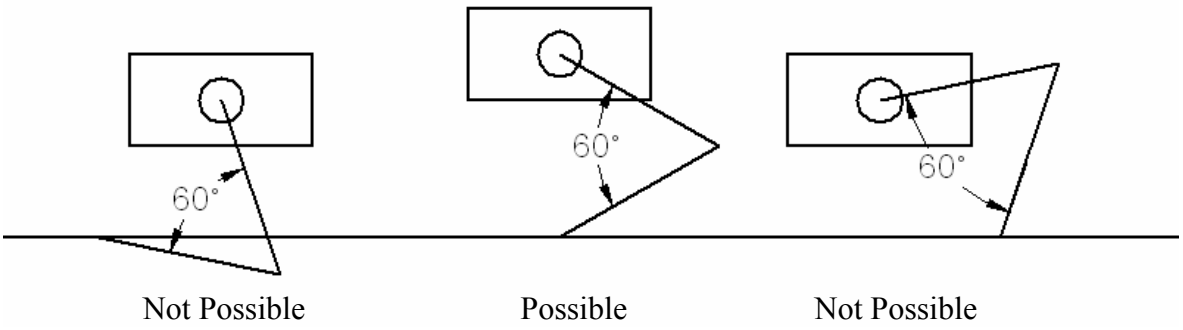

Figure 3.7: Physical Limitations for Leg Orientation

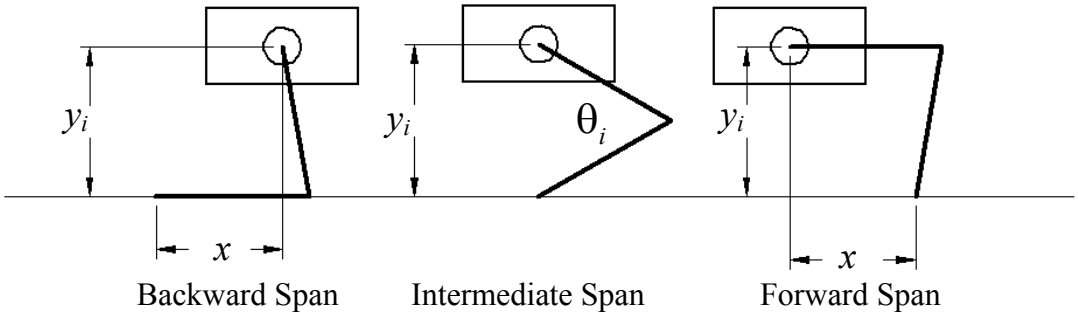

Figure 3.8: Initial Height Calculation Leg Spans

front of the hip axis to cause the thigh to become horizontal. The condition for this span is

$$x > r_2 - r_3 \cos\theta_i. \tag{3.41}$$

The thigh remains horizontal for all foot positions within this span, and the initial height is

$$y_i = \sqrt{r_3^2 - (r_2 - x)^2}. \tag{3.42}$$

The intermediate span lies in between the backward and forward spans. The virtual leg length remains constant throughout this span, and the initial height is

$$y_i = \sqrt{r_2^2 + r_3^2 - 2r_2 r_3 \cos\theta_i - x^2}. \tag{3.43}$$

3.7 Summary

This chapter presents a simplified analytical model of the leg that provides several distinct advantages over a more complex dynamic simulation. The work focuses on modeling the leg during the power stroke to determine the maximum jumping height for a given foot position and starting height. A kinematic model was derived for the leg, and the joint torques were determined from a simplified torque/leg-length motor model. A static force analysis was performed to compute the ground reaction forces at the foot

using three different methods, including the saturated torque method, the manipulating force ellipse method, and the vertical-only force method. The maximum jumping height was found using energy principles from the ground reaction forces. The analytical model can provide a fundamental understanding of the leg's operation that a dynamic simulation is not able to offer. In addition, the lack of time-based numeric integration inherent in a dynamic simulation makes the analytical model computationally simpler than a dynamic simulation.

CHAPTER 4

ANALYTICAL MODEL RESULTS

4.1 Introduction

This chapter presents the results generated by the analytical model formulated in Chapter 3. The analytical model was first validated against the dynamic simulation. The analytical motor models were tuned so the jumping height profiles closely matched the simulation, and these results are presented in Section 4.2. Section 4.3 presents a comparison between the jumping height profiles of the analytical model and the simulation to investigate the accuracy of the torque/leg-length motor model for various initial starting heights. Using the validated analytical model, the jumping height profiles for the three different force determination methods are investigated in Section 4.4. The manipulating force ellipse and the vertical-only force determination methods generated joint torque profiles for the individual jumping analyses. Several of these profiles are presented in Section 4.5. Finally, a summary concludes the chapter in Section 4.6.

4.2 Motor Model Validation

Simon Curran's dynamic simulation was used to tune and validate the two motor models presented in Section 3.3. The simulation has been used as a tool to predict the performance of the actual leg hardware. For the analytical model to be a useful simplified tool, the validation was necessary to ensure that the analytical model closely matched the simulation results. Jumping height profiles from the analytical model were compared to the simulation to determine how accurate the model predicted the simulation

results. A jumping height profile is a profile of the maximum jumping height the leg reached for a range of foot positions. The similarity in the shape of the curve and the maximum height predicted were considered the two key metrics of comparison.

The first motor model investigated was the saturated motor torque model presented in Section 3.3.1. Figure 4.1 shows the jumping height profile compared to the simulation for an initial body height y_i of 0.14m. This height was chosen for the comparison case because it was approximately the starting height typically used in the actual hardware. Figure 4.1a shows the actual height data from the simulation and the analytical model. The model predicted significantly higher jumps across the entire foot position range, which indicates the saturated motor model does not accurately reflect the actual motor dynamics. Figure 4.1b shows the height data normalized to its maximum value, which makes the curve shape comparison easier. The model profile drops off steeper than the simulation as the foot position increases in the positive direction. However, the foot position that yields the maximum jumping height is the same for both profiles, around -0.05m.

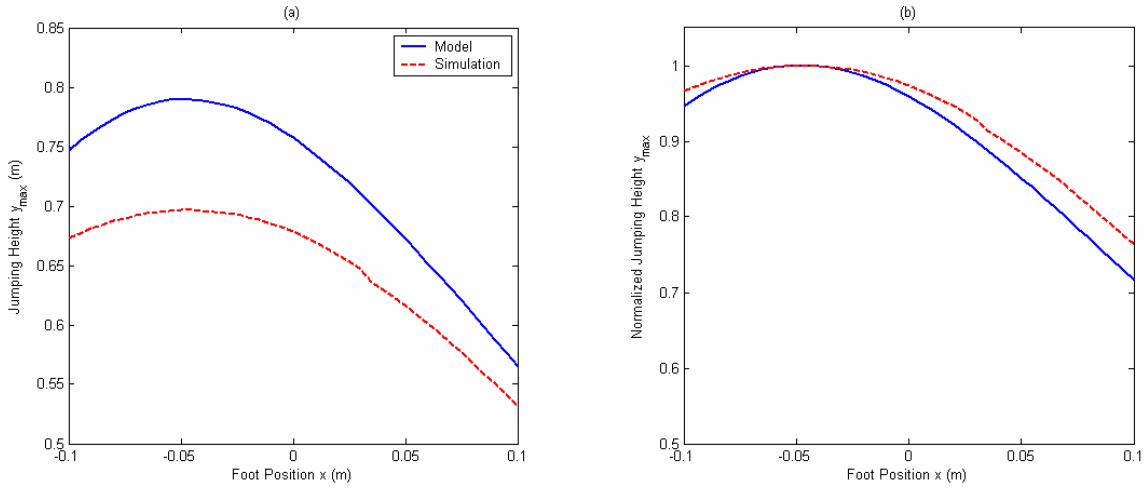

Figure 4.1: Jumping height profile for the saturated motor model and the simulation with an initial body height y_i of 0.14m. (a) Actual height data. (b) Normalized height data.

The torque/leg-length motor model was used to improve the accuracy of the analytical model. The first torque/leg-length motor model was tuned to produce the same maximum jumping height as the simulation, approximately 0.70m, as seen in Figure 4.2a. The hip motor saturation was 95%, and the knee motor saturation was 80%. However, the location of the maximum jumping height shifted 0.01m to the left of the simulation, which can be seen in Figure 4.2b. Also, the model profile still drops off sharper than the simulation. Regardless, this first motor model accurately predicts the jumping height of the leg in comparison to the simulation.

A second torque/leg-length motor model was tuned to try and improve the similarity in the shape of the profiles. The hip motor saturation was tuned to 70%, and the knee motor saturation was tuned to 0%. Figure 4.3a shows a large height disparity between the simulation and the model because the knee motor torque starts decreasing right from the initiation of the jump. Despite this disparity, Figure 4.3b shows that the profile shapes closely agree with each other. Because of the profile shape similarity, this second motor model is potentially more useful that the first to accurately predict how the

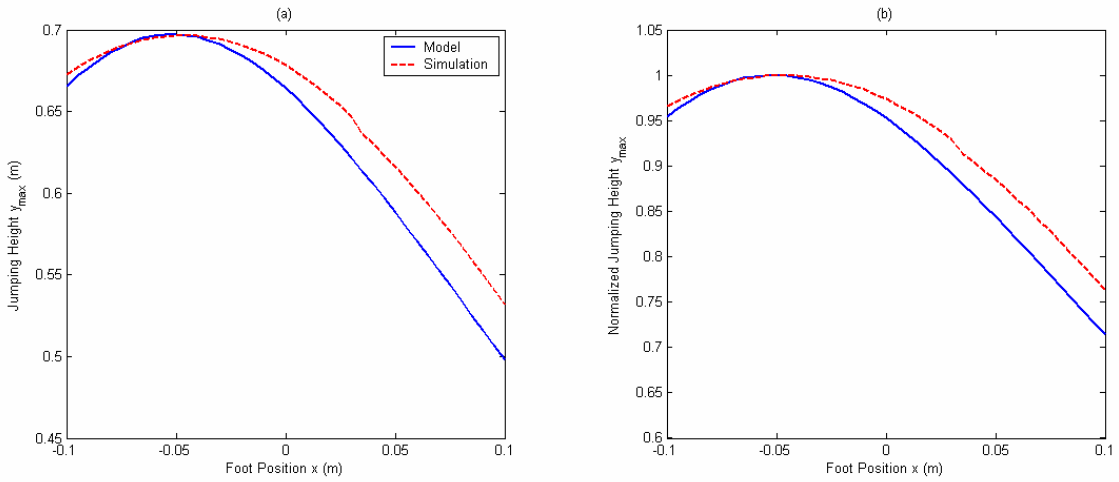

Figure 4.2: Jumping height profile for the first torque/leg-length motor model and the simulation with an initial body height y_i of 0.14m. Hip motor saturation is 95% and knee motor saturation is 80%. (a) Actual height data. (b) Normalized height data.

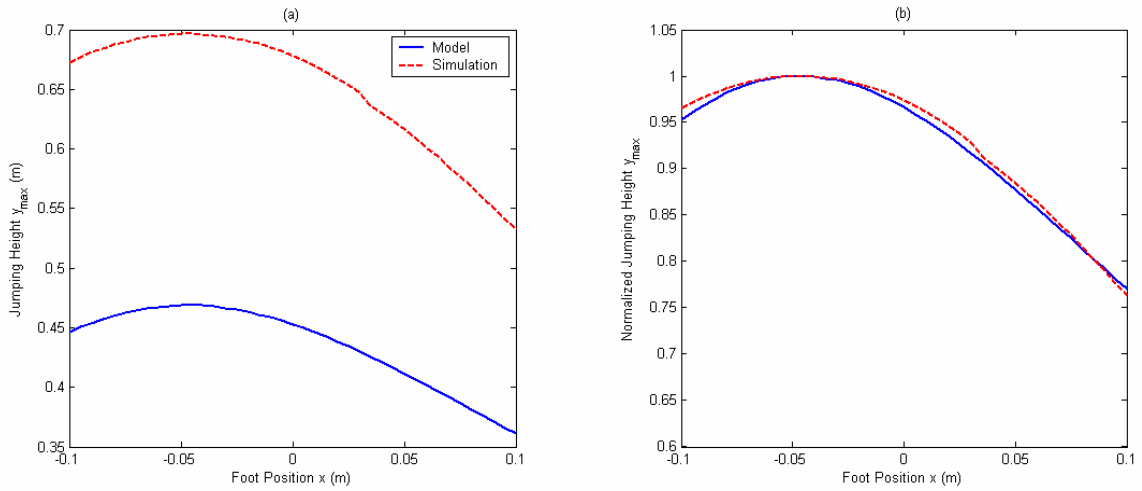

Figure 4.3: Jumping height profile for the second torque/leg-length motor model and the simulation with an initial body height y_i of 0.14m. Hip motor saturation is 70%, and knee motor saturation is 0%. (a) Actual height data. (b) Normalized height data.

leg will behave across the entire foot position range.

4.3 Simulation Comparison

Both torque/leg-length motor models were only validated for one initial starting height. The models were compared to the simulation results to investigate their accuracy over a range of initial starting heights. Two starting height comparison metrics were used in the investigation. First, the initial starting height y_i was a constant over the range of foot positions. Second, the initial virtual leg-length was constant over the range of foot positions as described in Section 3.6.

4.3.1 Constant Initial Height

The first torque/leg-length motor model comparision for a constant initial starting height y_i is shown in Figure 4.4. The three starting heights investigated were 0.11m, 0.14m, and 0.17m. The starting height of 0.11m was close to the lower limit that the hardware could achieve, and 0.17m was an equally spaced value from the median starting

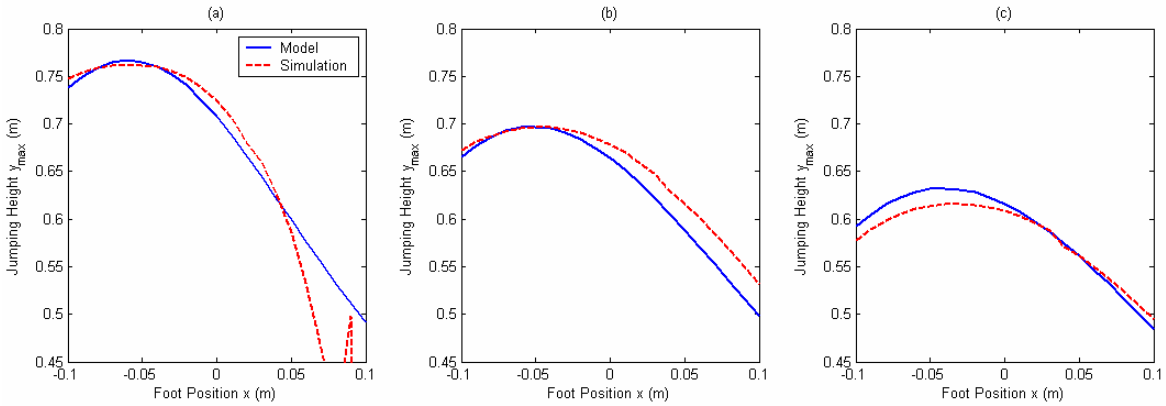

Figure 4.4: Jumping height profile comparison using the first torque/leg-length motor model at three separate initial starting heights y_i. (a) y_i = 0.11m (b) y_i = 0.14m. (c) y_i = 0.17m

height of 0.14m. The results indicate that the model can closely predict the height of the leg, but the shapes of the curves do not coincide exactly. The foot position predicted by the model that yields the maximum height of the leg is not exactly the same as that of the simulation. These results echo the motor validation findings for the first motor model.

The second torque/leg-length motor model comparison is shown in Figure 4.5. These results used the same initial starting heights as the first motor model comparison. The results are normalized because of the large disparity between the simulation height and the analytical model height. The shapes of the curves closely match the simulation in cases b and c, but there is a noticeable deviation from the simulation in case a. Despite

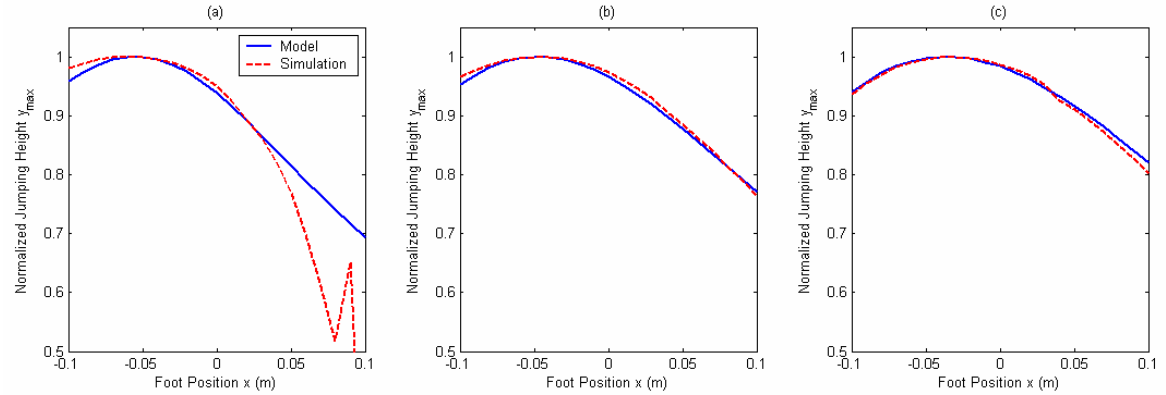

Figure 4.5: Normalized jumping height profile comparison using the second torque/leg-length motor model at three separate initial starting heights y_i. (a) y_i = 0.11m (b) y_i = 0.14m. (c) y_i = 0.17m

the ability to match the curve shapes, the first motor model is a better approximation of the simulation dynamics than the second motor model. The discontinuities seen in the dynamic simulation jumping height profile in Figure 4.4a and 4.5a are likely computational artifacts, and the investigation of their origins are beyond the scope of this research work.

4.3.2 Constant Initial Virtual Leg-Length

The two motor models were also compared to the simulation using a constant initial virtual leg-length to determine the starting height. Three initial knee angles θ_i, 50°, 60°, and 70°, were used in the comparison. A knee angle of 50° was the minimum angle possible in the hardware because of physical hard stops. Figure 4.6 shows how the constant initial knee angles translate into a starting height for the leg. The notches in the curves represent the transition between the three leg spans described in Section 3.6.2. The center arch is the intermediate span. The backward span is to the left of the first notch, and the forward span is to the right of the second notch.

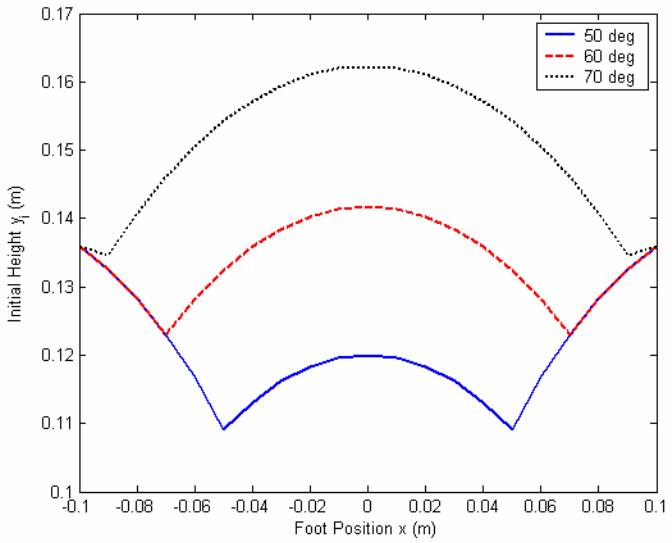

Figure 4.6: Initial starting height profiles.

Figure 4.7 shows the comparison for the first torque/leg-length motor model, and Figure 4.8 shows the comparison for the second motor model. Once again, the first motor model accurately predicts the maximum jumping height of the leg for all three initial knee angle cases. The second motor model results are once again normalized for comparison purposes. The curves produced by the second motor model are not noticeably closer in shape to the simulation than those produced by the first motor model. This further supports the claim that the first motor model more accurately predicts the simulation results over a broad range of input variables.

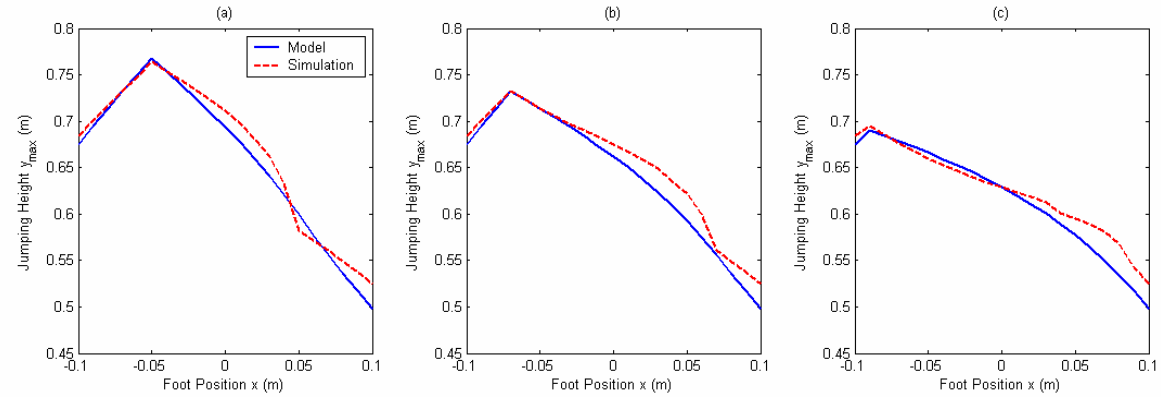

Figure 4.7: Jumping height profile comparison using the first torque/leg-length motor model at three separate initial knee angles θ_i. (a) $\theta_i = 50°$ (b) $\theta_i = 60°$ (c) $\theta_i = 70°$

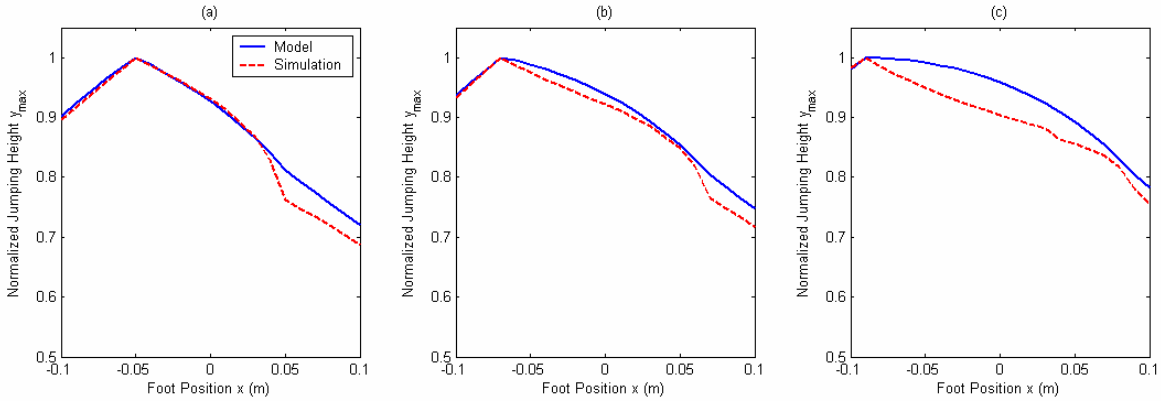

Figure 4.8: Normalized jumping height profile comparison using the second torque/leg-length motor model at three separate initial knee angles θ_i. (a) $\theta_i = 50°$ (b) $\theta_i = 60°$ (c) $\theta_i = 70°$

4.4 Comparison of Force Determination Methods

As presented in Section 3.4, three different methods were used to determine the ground reaction forces on the leg's foot – the maximum torque method, the manipulating force ellipse method, and the vertical-only force method. The two torque/leg-length motor models were used to generate jumping height profiles for the three force determination methods. The force determination methods were compared based on the constant initial starting height metric and the constant initial virtual leg-length metric.

4.4.1 Constant Initial Height

The three constant initial starting heights investigated for the force determination method comparison were 0.11m, 0.14m, and 0.17m. Figure 4.9 shows the three force determination jumping height profiles generated from the first torque/leg-length motor model, and Figure 4.10 shows those profiles generated from the second motor model. There are several similar trends for each motor model. The maximum force method produced the highest maximum jump out of the three force determination methods. The foot position for the highest jump is situated well behind the center of the leg, around -0.05m. The shank is nearly horizontal in this foot location, allowing the large knee motor to transfer most of its torque into a vertical force, thereby increasing the input energy contribution to vertical motion. Also, there is a relatively large difference in jumping height between the initial starting heights for the maximum force method.

Interestingly, the optimum foot position moves closer to the center of the leg as the initial starting height increases. The location of the optimum foot position is a tradeoff between the effect of the knee motor and the starting virtual leg length. A smaller virtual leg length will yield a higher jump because the power stroke is longer, but

the leg must be in an orientation to take advantage of the powerful knee motor. The knee motor contributes the most to vertical motion when the foot is positioned far behind the hip axis, but this position also has a larger initial virtual leg length that negatively impacts the jump. The position that maximizes both these effects likely corresponds to the optimum foot position. This position also moves closer to the hip axis as the initial starting height increases because the configuration of the leg changes and this might offer an explanation to why the optimum foot position changes with the initial starting height.

The other two force determination methods have a similar trend with the optimum foot position and the difference in jumping heights between the initial starting heights.

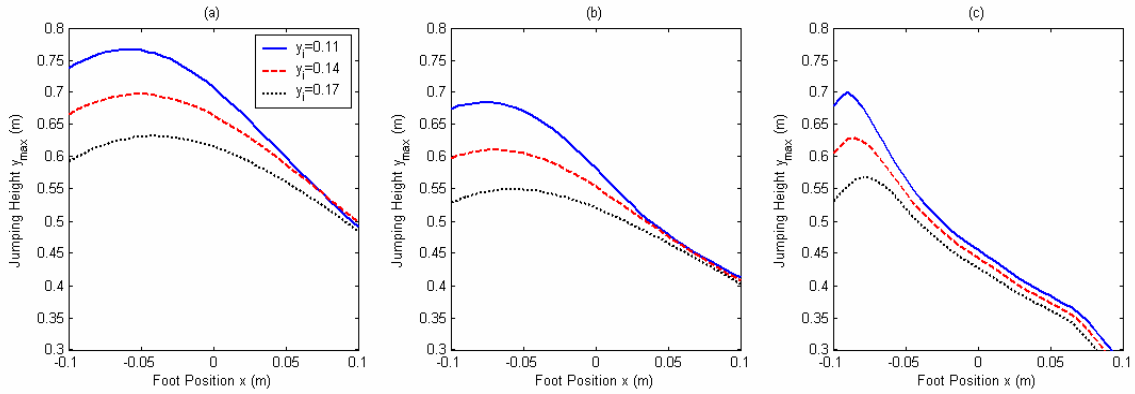

Figure 4.9: Jumping height profile comparison for the three ground force determination methods using the first torque/leg-length motor model at three separate initial starting heights y_i. (a) Maximum torque. (b) Manipulating force ellipse. (c) Vertical-only force.

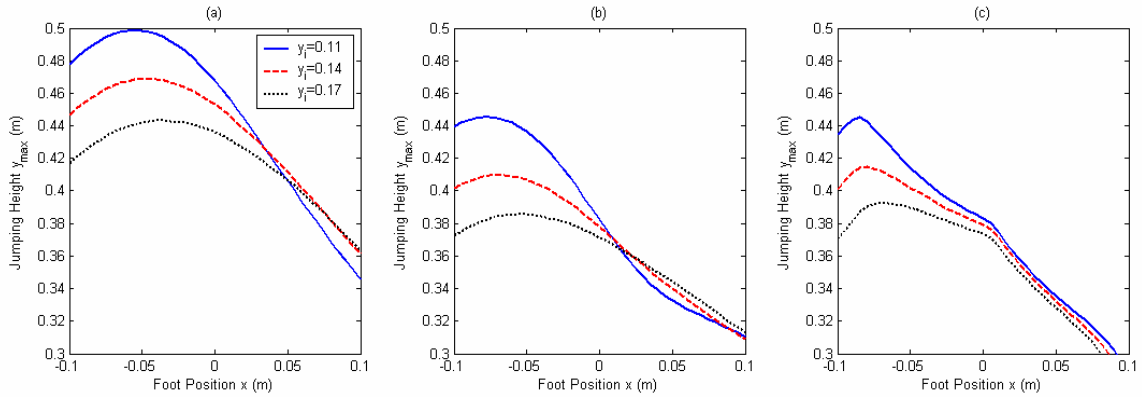

Figure 4.10: Jumping height profile comparison for the three ground force determination methods using the second torque/leg-length motor model at three separate initial starting heights y_i. (a) Maximum torque. (b) Manipulating force ellipse. (c) Vertical-only force.

However, the optimum foot position is located further behind the leg than in the maximum force method. This is particularly noticeable in the vertical-only force method. To create a vertical-only reaction force, the undersized hip motor must counter any horizontal forces produced by the knee motor. When the foot is positioned such that the shank is horizontal, the knee motor can produce a larger vertical force without increasing the horizontal force component. Interestingly, for these two force determination methods, the effect of the initial height on the jumping height is negligible outside the local region surrounding the optimum foot position. This is likely because the benefit of the larger knee motor is marginalized in these leg positions.

4.4.2 Constant Initial Virtual Leg-Length

The force determination methods were also compared using three constant initial knee angles θ_i of 50°, 60°, and 70°. Figure 4.11 shows the three force determination jumping height profiles generated from the first torque/leg-length motor model, and Figure 4.12 shows those profiles generated from the second motor model. The trends seen in the constant virtual leg-length comparison are almost identical to those

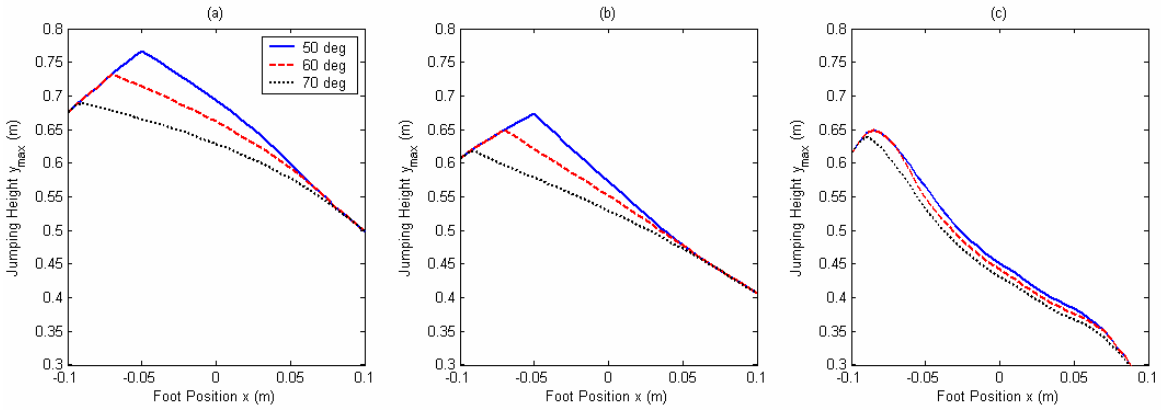

Figure 4.11: Jumping height profile comparison for the three ground force determination methods using the first torque/leg-length motor model at three separate initial knee angles θ_i. (a) Maximum torque. (b) Manipulating force ellipse. (c) Vertical-only force.

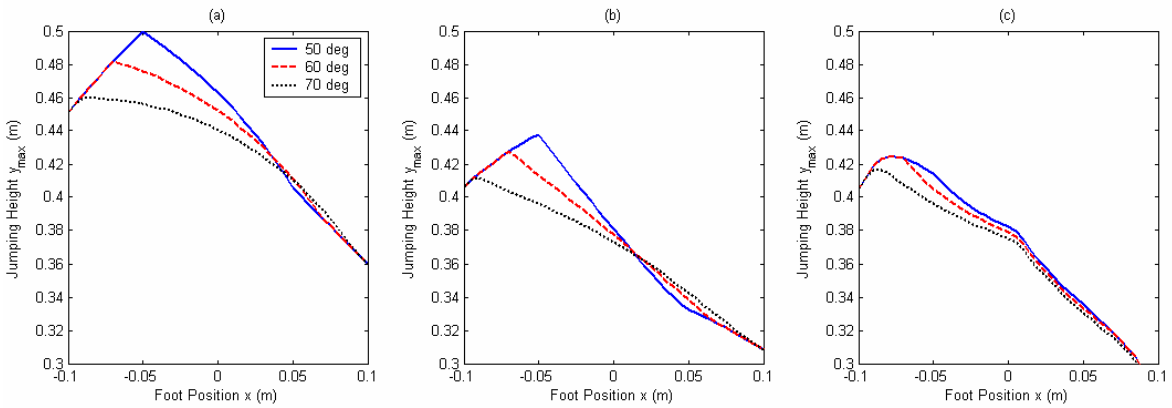

Figure 4.12: Jumping height profile comparison for the three ground force determination methods using the second torque/leg-length motor model at three separate initial knee angles θ_i. (a) Maximum torque. (b) Manipulating force ellipse. (c) Vertical-only force.

seen in the constant initial height comparison. The most noticeable difference, however, is that the initial knee angles have even less effect on the difference in jumping height in the vertical-only force method. The jumping height disparity is not even noticeable around the optimum foot position, as in the constant initial height comparison.

4.5 Calculated Joint Torque Profiles

Both the manipulating force ellipse and the vertical-only force determination methods generated joint torque profiles as discussed in Section 3.4. These profiles provide the necessary torques required over the power stroke to generate the desired ground reaction forces based on the force determination method. Figure 4.13 shows the torque profiles for the hip joint at three different foot positions, -0.05m, 0.0m, and 0.05m. The torque profiles for the manipulating force ellipse and the vertical-only force are compared to the saturated torque profile at each foot position. For this comparison, the first torque/leg-length motor model was used, so the saturated torque profile is simply the torque/leg-length curve for the joint. Figure 4.14 shows the knee torque profiles for the same set of conditions. The initial starting height for each jump was 0.14m.

The torque profiles can be useful to understand the contribution of each motor in a jump. For the manipulating force ellipse, the hip motor does not operate close to its torque limit, indicating that the knee motor generates nearly all the necessary energy for the jump. Looking at Figure 4.9, the average difference in jumping height between using saturated motor torque or the force ellipse is only around 0.05m. This suggests that the hip motor's contribution to the jumping height is much less than the knee motor. A hip motor closer in size to the knee motor may greatly increase the jumping height of the leg. Also, the joint torque profiles for the vertical-only force determination confirm the conclusions drawn in Section 4.4. As the position of the shank becomes more vertical with the forward foot position, the torque output of the knee motor must be cut drastically to reduce the horizontal components of the reaction force. If the hip motor was sized similarly to the knee motor, the torque decrease would not likely be necessary. The leg would then produce a more uniform jumping height profile for a vertical-only force jump.

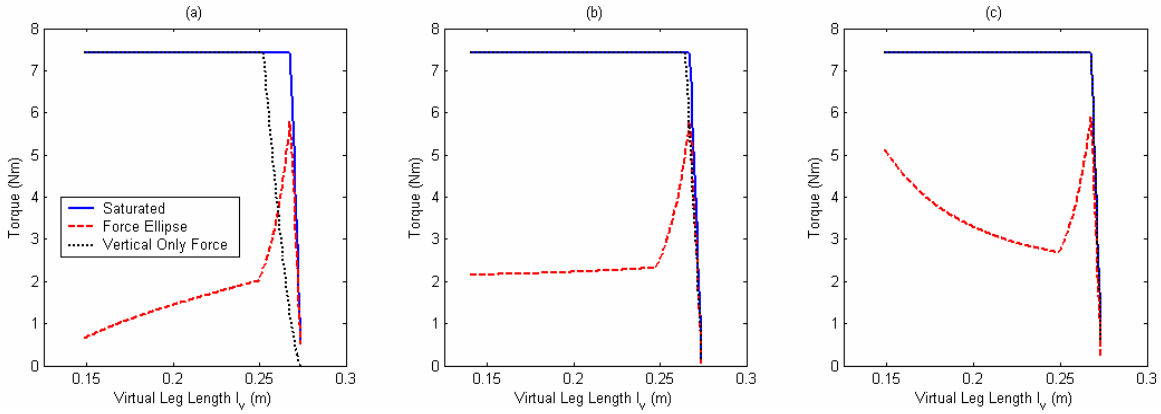

Figure 4.13: Hip torque profile comparison for the three ground force determination methods using the first torque/leg-length motor model at an initial starting height of y_i = 0.14m. (a) x = -0.05m (b) x = 0.0m (c) x = 0.05m

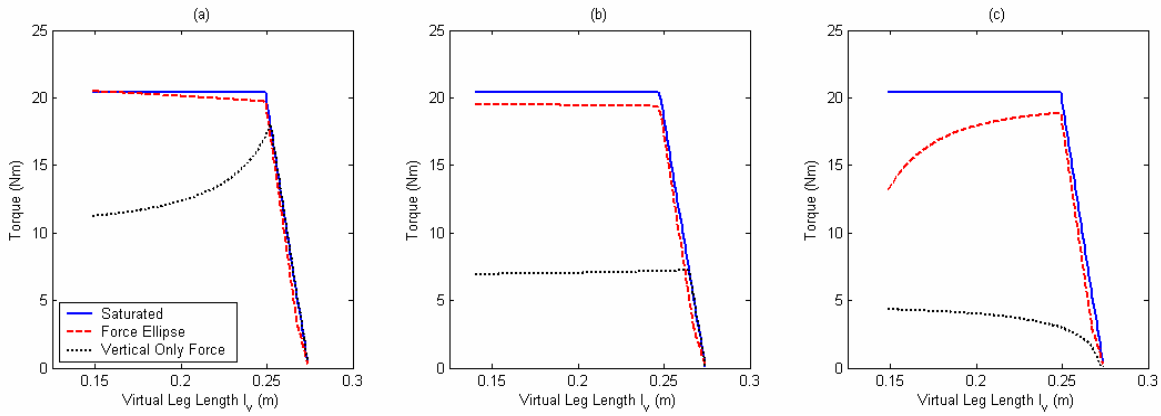

Figure 4.14: Knee torque profile comparison for the three ground force determination methods using the first torque/leg-length motor model at an initial starting height of y_i = 0.14m. (a) x = -0.05m (b) x = 0.0m (c) x = 0.05m

4.6 Summary

The results presented in this chapter were used to validate the analytical model developed in Chapter 3 and draw some fundamental conclusions about the leg's operation. By comparing the model results to the dynamic simulation, two specific torque/leg-length motor models were created. The first motor model proved to be better than the second. The motor model accurately predicted the jumping height profiles and optimum foot positions generated by the simulation over a range of initial conditions. The second motor model failed to predict the jumping heights, but the shapes of the jumping height profiles were almost identical to the simulation curves. Both motor models were used in the three force determination methods to generate jumping height profiles. The optimum foot positions for the maximum jump were found for each force determination method from these profiles, and they were all generally located -0.05m behind the hip axis. The asymmetrical jumping height profiles also illustrated the effects of having a mismatched hip and knee motor. Since the knee motor is more powerful than the hip motor, the optimum jumping positions are concentrated in the region that allows

the knee motor torque to contribute primarily to vertical motion of the leg. Sizing the hip motor similar to the knee motor may yield a more uniform jumping height profile.

CHAPTER 5

SUMMARY AND FUTURE WORK

5.1 Summary

For legged robots to interact with realistic environments, they must be capable of performing fluid dynamic maneuvers. These maneuvers would allow a robot, particularly a biped, to take full advantage of its legged mobility and adapt naturally to its surroundings. However, the ability to generate complex dynamic maneuvers in biped robots, such as a running jump or a high speed turn, is not well understood. Only a handful of biped robots to date have succeeded in executing some simple dynamic manuevers [5, 6, 18], and no robot has performed a truly complex dynamic maneuver.

The focus of this work was to investigate the requirements necessary to execute dynamic maneuvers in a prototype robotic hopping leg. The preexisting prototype leg was a 2-DOF, series compliant mechanism that was constrained to a vertical hopping motion in an experimental setup, and the hip and knee joints were each electrically actuated with a brushless DC motor. Emphasis was placed on evaluating the leg's mechanical design to ensure the system's reliability when performing dynamic maneuvers, specifically continuous jumping and fast limb cycling. Also, the leg's jumping performance was analyzed using a simplified analytical model with the goal to maximize the jumping height for the existing hardware system.

To improve the leg's robustness and reliability, several design modifications were made to the hardware based on experimental observations. Dynamic maneuvers require

accurate and reliable position control at high speeds, and several of the design modifications were made to improve the leg's control accuracy. The drive cable attachments to the drive pulleys were modified to eliminate slipping problems, and a position potentiometer was added to the knee axis so accurate shank positions could be sensed. Also, a new hard stop system was added to the torsion spring in the knee, which reduced slop in the joint and allowed the shank to consistently return to the same position.

The three remaining design modifications improved the system's mechanical robustness. A new cable tensioning system alleviated mechanical failures resulting from the leg's assembly process and greatly simplified servicing the leg's hardware components. The carbon fiber tubes on the thigh were replaced several times after they fractured. Finally, the hip motor was replaced twice due to mechanical failures. The first incident was a bent drive shaft caused by the previous leg assembly methods without a tensioning system, and the second incident was the result of the motor amplifier overheating the motor windings.

The simplified analytical model based on the hardware system was developed to investigate the leg's jumping performance. A simplified analytical model could provide significant advantages over a more complex dynamic simulation and possibly lead to a fundamental understanding of the leg's operation. The leg was analyzed during the power stroke to determine the maximum jumping height based on the foot position and initial starting height. A static force analysis was incrementally performed over the power stroke to calculate the ground reaction forces on the foot, and the three force determination methods used were the saturated motor torque method, the manipulating

force ellipse method, and the vertical-only force method. A simplified motor model was created to capture the dynamic characteristics of the electric actuators and determine the input joint torques for the static force analysis. The motor model, called the torque/leg-length model, related the motor output torque to the virtual leg-length of the leg during a jump. The jumping height was determined from the total energy input to the leg that contributed to vertical motion.

A dynamic simulation was used to validate the analytical model and calibrate the simplified motor model. The analytical model was then used to find the optimum foot position that yielded the highest overall jump. For the all three force determination methods, the optimum foot locations were approximately -0.05m behind the hip axis. The jumping height profiles were largely asymmetric, showing that the leg could attain a significantly higher jump when the foot was placed behind the hip axis as compared to in front of the hip axis. A mismatch in motor power between the hip and knee motors mostly contributed to the asymmetry, and a more evenly matched motor pair would likely result in a more uniform jumping height profile.

The work accomplished with the hardware modifications and the analytical model proved to be exceptionally valuable in understanding the operation of the prototype hopping leg. The knowledge gained through this thesis work helped dramatically improve the performance of the hardware system and enabled the system to be capable of limited dynamic maneuvers, including repeated jumping and accurate, high-speed positioning. However, more work is needed to achieve truly complex dynamic maneuvers in a robotic system. The next section presents several recommendations for future work involving the prototype leg and beyond.

5.2 Future Work

Several additional hardware modifications could further increase the jumping height and performance of the prototype leg. Based on the results from the analytical model, the replacement of the hip motor with one comparable in size to the knee motor could provide significant benefits. First, the jumping height profiles would likely be more uniform across the range of foot positions. A precise foot position might not be needed to achieve comparable jumping heights. Second, the higher torque rating of the new hip motor would increase the power available to the leg and the overall jumping height.

The new motor can be easily integrated into the existing hardware. The design of the cable tensioning system allows for the motor to be replaced without significant alterations to the hardware. A new tensioning plate would have to be machined to fit the size of the large motor, and a new drive pulley that fits the larger motor shaft would also have to be made. Appendix A shows mechanical drawings for the two new pieces, and both pieces can be made and inserted without disassembling the existing hardware. Actually, a new tensioning plate and drive pulley have already been machined to fit a second knee motor, but the parts have not yet been used on the hardware because of ongoing experimental testing with the current configuration.

Current research results produced by Simon Curran suggest two additional hardware modifications involving compliant elements in the leg. One possibility is to add a series-compliant element to the hip axis drive train similar to the knee drive train. A spring on the hip axis will allow for energy storage at the joint, which may be transferred to the leg during jumping and possibly lead to a higher jumping height. However, a

significant redesign of the entire body of the leg would likely be necessary to fit a similar torsion spring to the knee on the hip. Another possibility is to replace the current knee spring with a non-linear spring, which could also improve the jumping height of the leg. An actual non-linear spring would be difficult to manufacture, so an alternative would be to design a mechanism at the knee that uses a linear spring to create an effective non-linear spring constant. This mechanism would also pose a significant design challenge to fit the system within the space constraints of the knee while minimizing the overall weight.

The analytical model can also be improved by implementing more realistic modeling methods. Currently, the manipulating force ellipse used in the analytical model only takes into account the static forces on the leg. Yoshikawa introduced a dynamic manipulability ellipse that accounts for the dynamic forces on the manipulator links based on their moments of inertia [23]. The model would have to be slightly reconfigured to account for the limbs' moments of inertia as well as the effect that the body mass has on the limb dynamics. Also, a model of friction in the rails could be added to the analytical model. Jeff Wensink began this work as an undergraduate summer intern. However, the friction model not yet been implemented into the current model because the dynamic simulation used for validation neglected friction. A friction model could be used to optimize the joint torques at a given foot position to achieve the maximum jumping height.

The analytical model should be validated against the actual hardware system. This can be accomplished through experimental tests that are similar to the foot offset loop in the analytical model. Multiple jump tests can be conducted at several foot

positions across the physical range of the leg. The height data from the experiments can then be compared to the analytical model to verify the accuracy of the current torque/leg-length motor model. Another experimental validation would be to generate torque/leg-length curves for the hardware actuators based on the measured speed and torque-speed curve of each motor. New motor saturation percentages may need to be chosen so that the analytical motor model accurately reflects the hardware's performance.

Eventually the proven design of the prototype leg can be incorporated into a full planar biped robot. Successful integration of the design poses several significant challenges, especially if the biped robot is to be larger than the prototype leg. The leg's design will have to be scaled effectively to ensure that the system will produce the necessary power to jump while minimizing weight and maintaining structural integrity. Component placement in the full biped will also be a key concern. Currently the leg motors face opposite directions, but in a biped they should likely face the same direction for a compact design, which will significantly change the structure of the prototype leg's body. Also, the location of the center of mass of the biped plays a crucial role in stability control and is dictated solely by the mechanical design of the system.

Despite these future challenges, the results accomplished from this thesis work have significantly progressed the understanding of the requirements for dynamic maneuvers in legged robots and may one day lead to a biped robot capable of complex dynamic maneuvers.

APPENDIX A

HARDWARE MODIFICATION MECHANICAL DRAWINGS

Table A.1: List of Mechanical Drawings

Name	Page
Potentiometer Bracket	83
Potentiometer Shaft Coupler	84
Shank Fork Spring Retainer 1	85
Shank Fork Spring Retainer 2	86
Knee Pulley Spring Retainer 1	87
Knee Pulley Spring Retainer 2	88
Moveable Hard Stop	89
Hard Stop Holder	90
Shank Fork Modifications	91
Knee Side Plate	92
Knee Tensioning Plate	93
Hip Side Plate	94
Hip Tensioning Plate	95
Clamping Plate	96
Moving Plate Modifications	97
Modified Knee Motor Pulley	98
Knee Motor Pulley Cover	99

REVISION HISTORY			
REV	DESCRIPTION	DATE	APPROVED

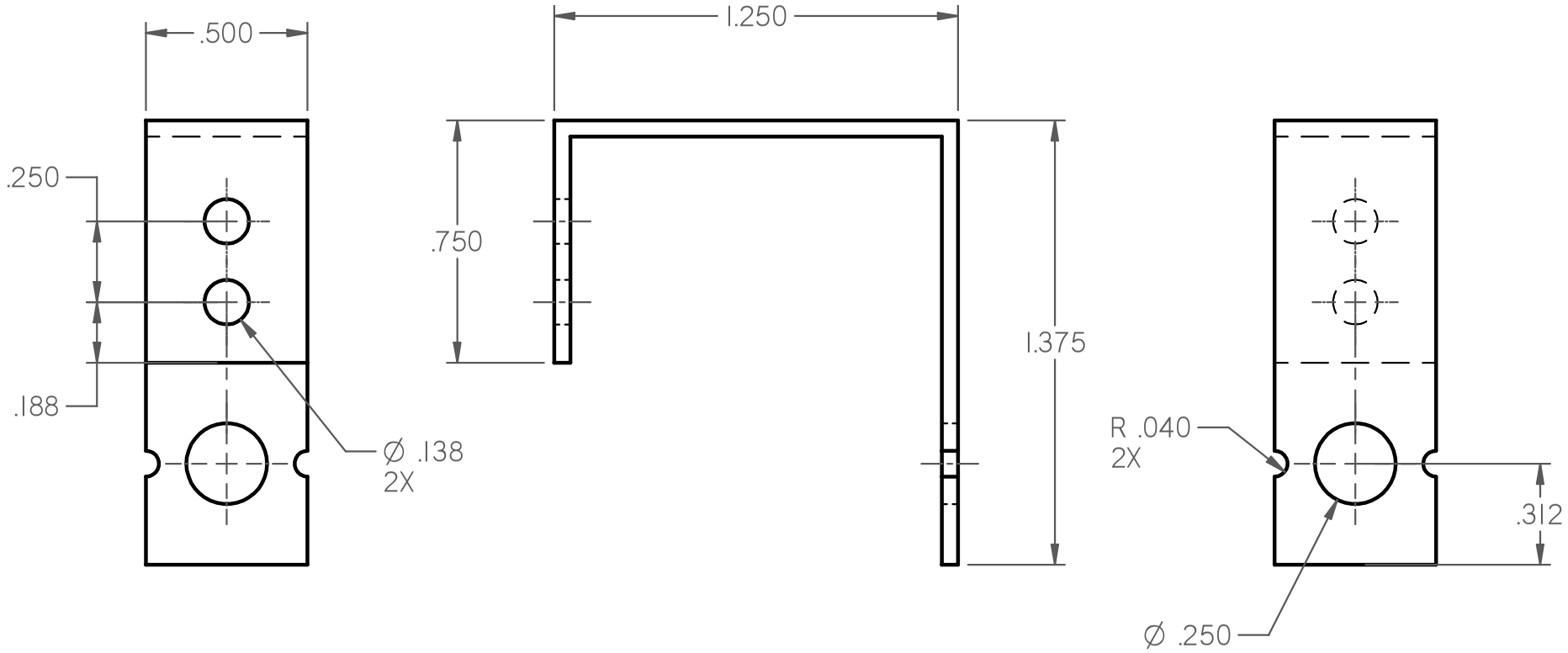

NOTES:
1. Material - 0.05" Sheet Aluminum
2. All holes on center.

	NAME	DATE
DRAWN	Brian	10/03/06
CHECKED		
ENG APPR		
MGR APPR		

UNLESS OTHERWISE SPECIFIED
DIMENSIONS ARE IN INCHES
ANGLES ±X.X°
2 PL ±X.XX 3 PL ±X.XXX

SOLID EDGE
UGS - The PLM Company

TITLE: Potentiometer Bracket

SIZE	DWG NO	REV
A		

FILE NAME: pot_bracket.dft

SCALE:	WEIGHT:	SHEET 1 OF 1

REVISION HISTORY			
REV	DESCRIPTION	DATE	APPROVED

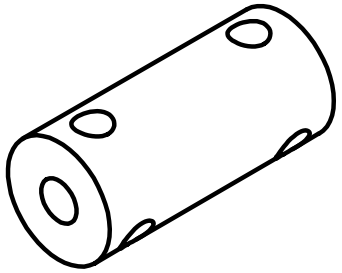

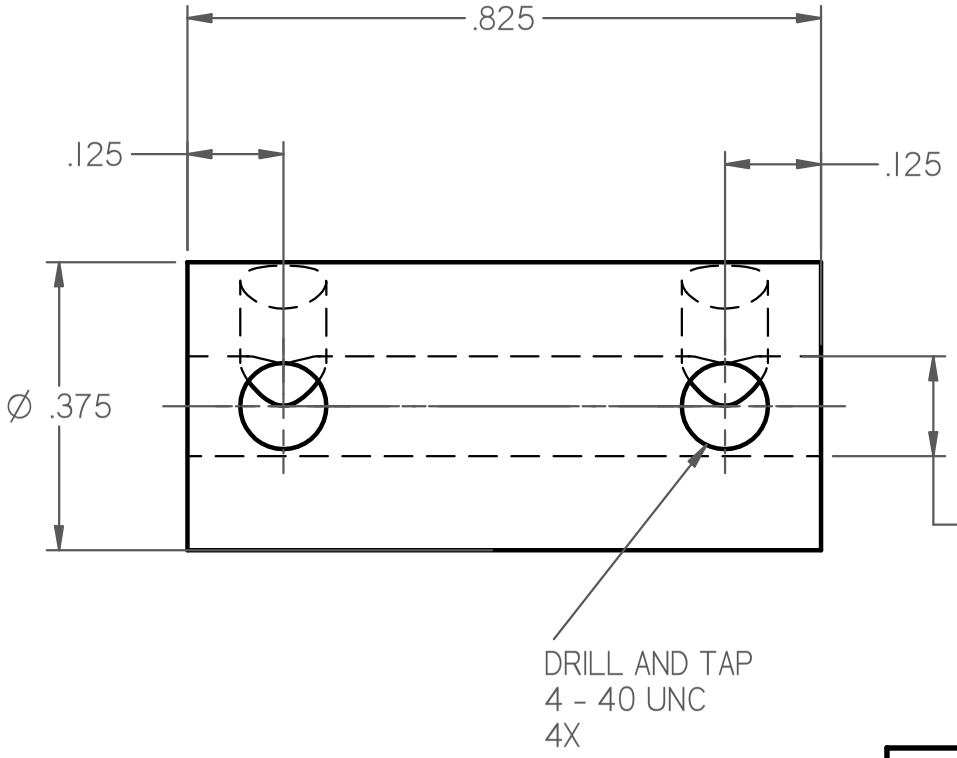

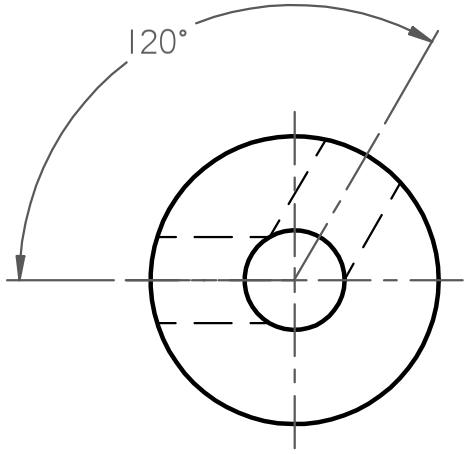

NOTES:
1. Material - Aluminum

	NAME	DATE
DRAWN	Brian	10/03/06
CHECKED		
ENG APPR		
MGR APPR		

UNLESS OTHERWISE SPECIFIED
DIMENSIONS ARE IN INCHES
ANGLES ±X.X°
2 PL ±X.XX 3 PL ±X.XXX

SOLID EDGE
UGS - The PLM Company

TITLE
Potentiometer Shaft Coupler

SIZE	DWG NO	REV
A		

FILE NAME: shaft_coupler.dft

SCALE:	WEIGHT:	SHEET 1 OF 1

REVISION HISTORY			
REV	DESCRIPTION	DATE	APPROVED

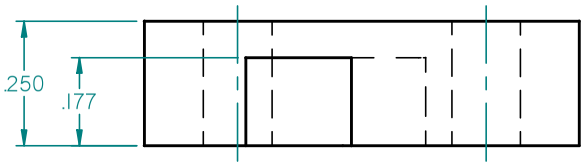

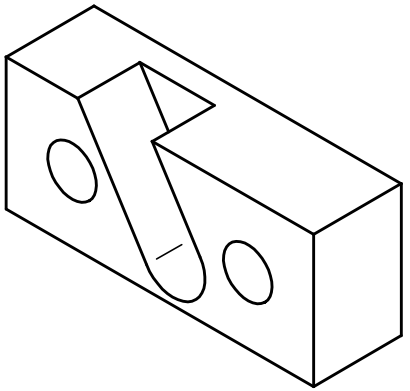

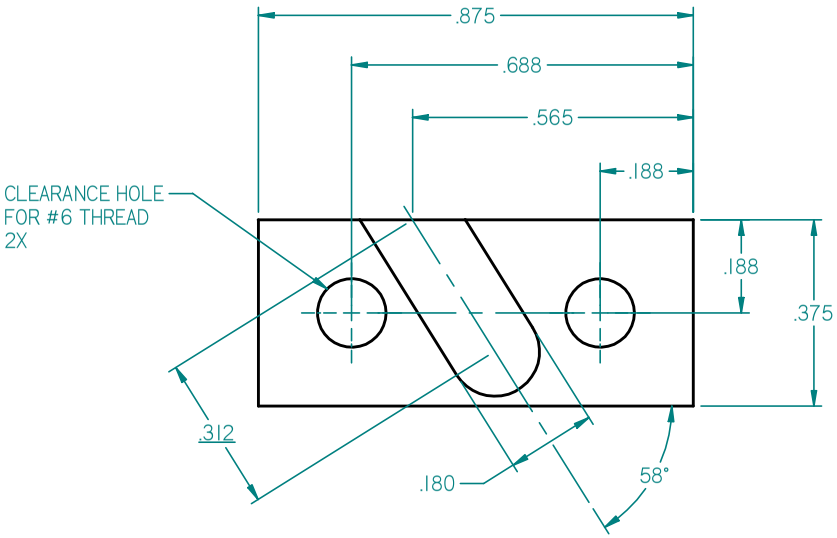

NOTES:
1. MATERIAL: STEEL

	NAME	DATE
DRAWN	Brian	11/29/06
CHECKED		
ENG APPR		
MGR APPR		

UNLESS OTHERWISE SPECIFIED
DIMENSIONS ARE IN INCHES
ANGLES ±X.X°
2 PL ±X.XX 3 PL ±X.XXX

SOLID EDGE
UGS - The PLM Company

TITLE
SHANK FORK SPRING RETAINER 1

SIZE	DWG NO	REV
B		

FILE NAME: spring_ret_1new.dft

SCALE:	WEIGHT:	SHEET 1 OF 1

REVISION HISTORY			
REV	DESCRIPTION	DATE	APPROVED

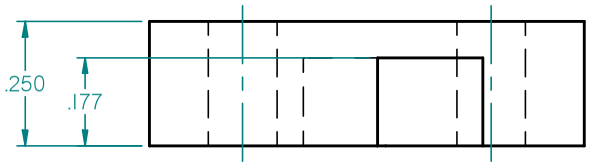

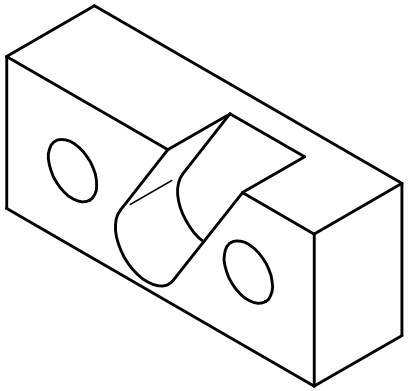

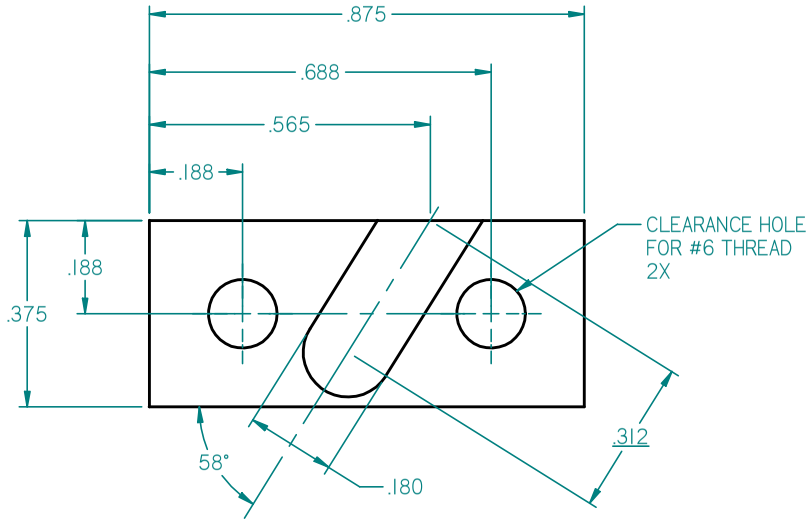

NOTES:
1. MATERIAL: STEEL

	NAME	DATE
DRAWN	Brian	11/29/06
CHECKED		
ENG APPR		
MGR APPR		

UNLESS OTHERWISE SPECIFIED
DIMENSIONS ARE IN INCHES
ANGLES ±X.X°
2 PL ±X.XX 3 PL ±X.XXX

SOLID EDGE
UGS - The PLM Company

TITLE
SHANK FORK SPRING RETAINER 2

SIZE	DWG NO	REV
B		

FILE NAME: spring_ret_2new.dft

SCALE:	WEIGHT:	SHEET 1 OF 1

REVISION HISTORY			
REV	DESCRIPTION	DATE	APPROVED
A	Changed Arc Length	01/22/07	

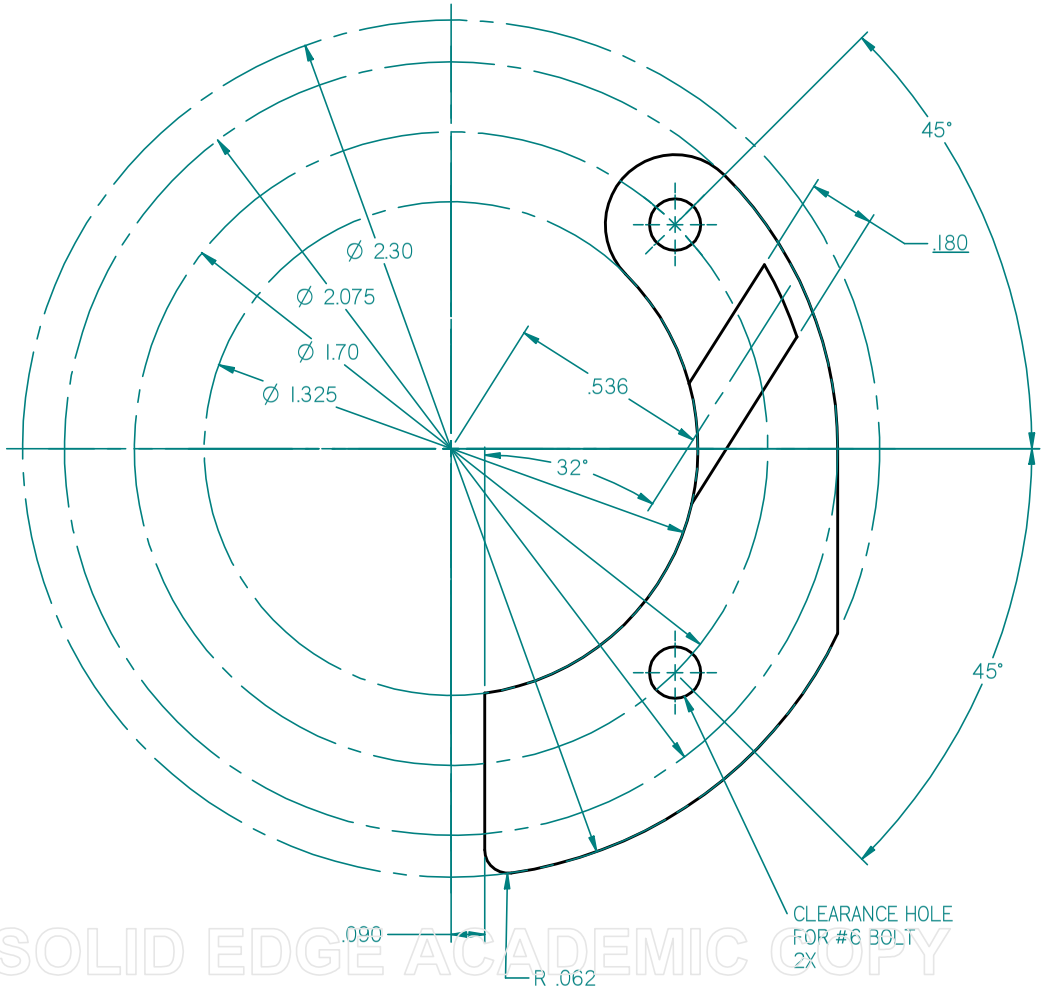

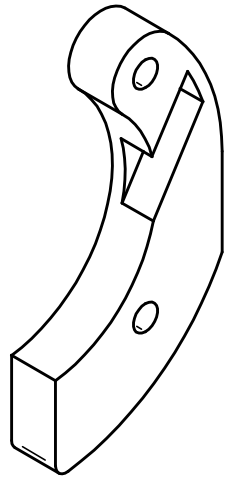

Notes:
1. Material - Steel
2. Spring Retainer 1 and 2 are mirror images of each other

	NAME	DATE
DRAWN	Brian	10/31/06
CHECKED		
ENG APPR		
MGR APPR		

UNLESS OTHERWISE SPECIFIED
DIMENSIONS ARE IN INCHES
ANGLES ±X.X°
2 PL ±X.XX 3 PL ±X.XXX

SOLID EDGE
UGS - The PLM Company

TITLE: Spring Retainer 1

SIZE	DWG NO	REV
B		1

FILE NAME: pulley_spring_ret_hardstop1.dft

SCALE:	WEIGHT:	SHEET 1 OF 1

REVISION HISTORY			
REV	DESCRIPTION	DATE	APPROVED
A	Changed Arc Length	01/22/07	

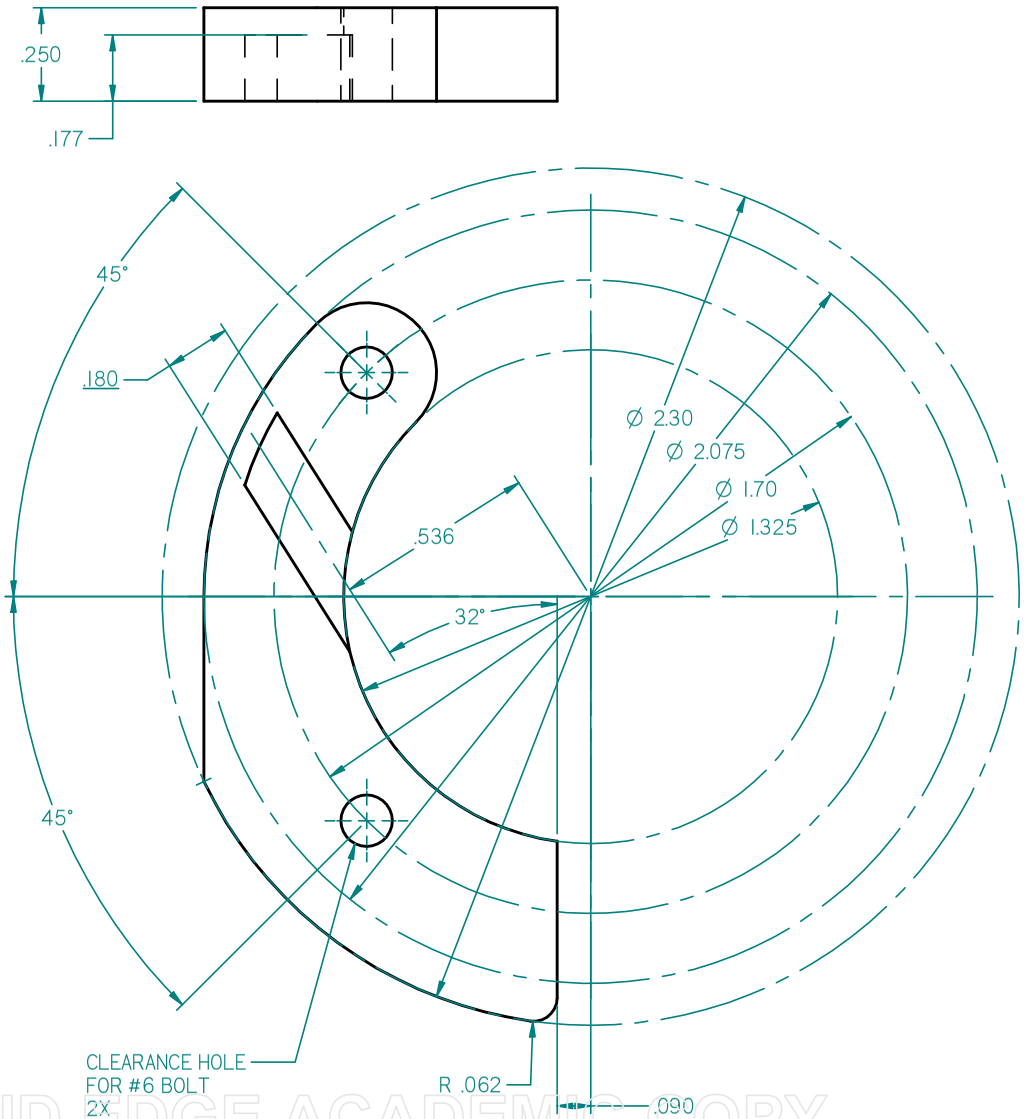

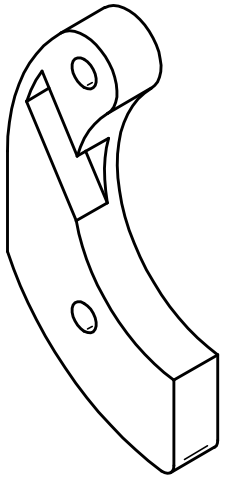

Notes:
1. Material - Steel
2. Spring Retainer 1 and 2 are mirror images of each other

	NAME	DATE
DRAWN	Brian	11/02/06
CHECKED		
ENG APPR		
MGR APPR		

UNLESS OTHERWISE SPECIFIED
DIMENSIONS ARE IN INCHES
ANGLES ±X.X°
2 PL ±X.XX 3 PL ±X.XXX

SOLID EDGE
UGS - The PLM Company

TITLE: Spring Retainer 2

SIZE B | DWG NO | REV

FILE NAME: pulley_spring_ret_hardstop2.dft

SCALE: | WEIGHT: | SHEET 1 OF 1

REVISION HISTORY			
REV	DESCRIPTION	DATE	APPROVED

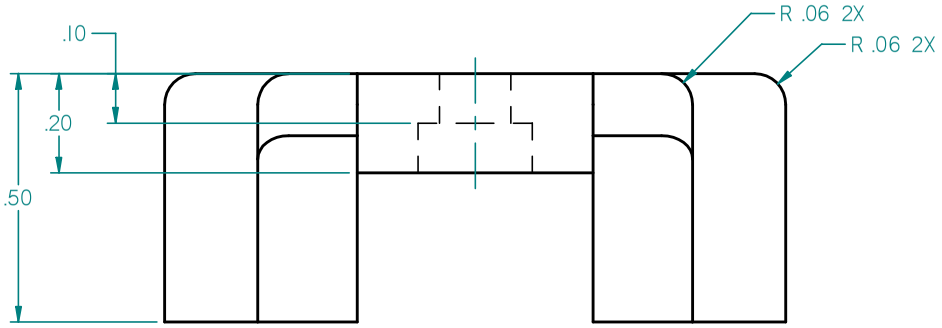

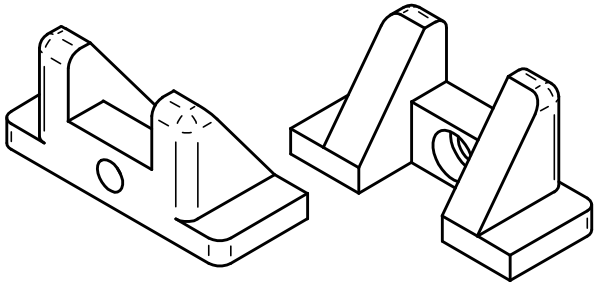

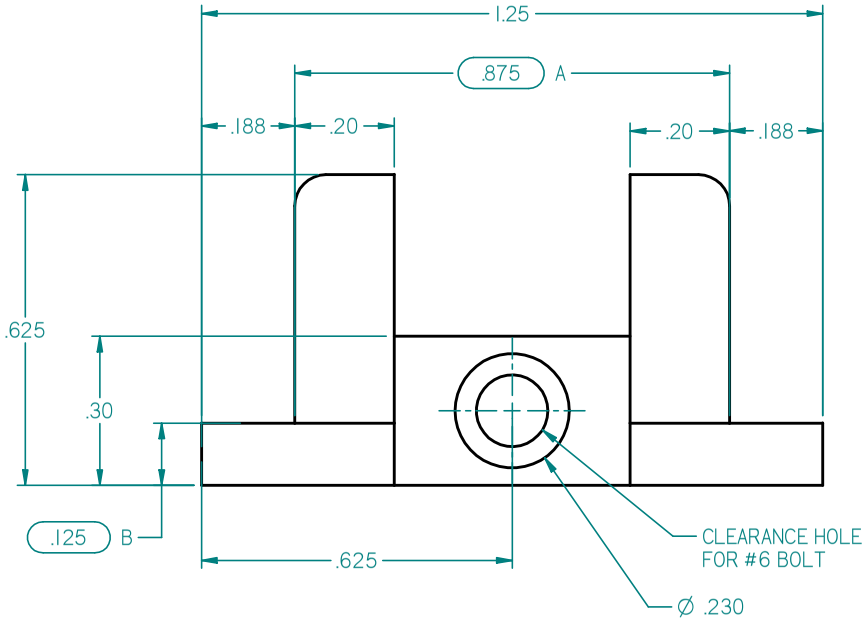

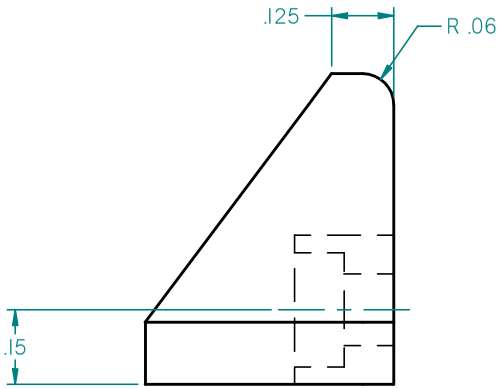

Notes:
1. Material - Aluminum
2. Dimension A must be clearance fit with Dimension A on Hardstop Holder part
3. Dimension B must be interfearnace fit with Dimension B on Harstop Holder part

	NAME	DATE
DRAWN	Brian	11/02/06
CHECKED		
ENG APPR		
MGR APPR		

UNLESS OTHERWISE SPECIFIED
DIMENSIONS ARE IN INCHES
ANGLES ±X.X°
2 PL ±X.XX 3 PL ±X.XXX

SOLID EDGE
UGS - The PLM Company

TITLE: Movable Hardstop

SIZE	DWG NO	REV
B		

FILE NAME: movable_stop.dft

SCALE:	WEIGHT:	SHEET 1 OF 1

REVISION HISTORY			
REV	DESCRIPTION	DATE	APPROVED

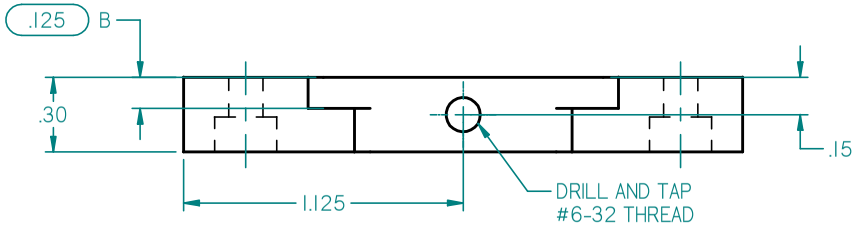

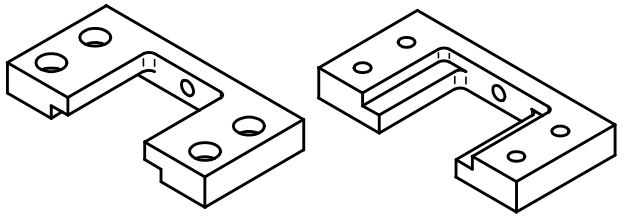

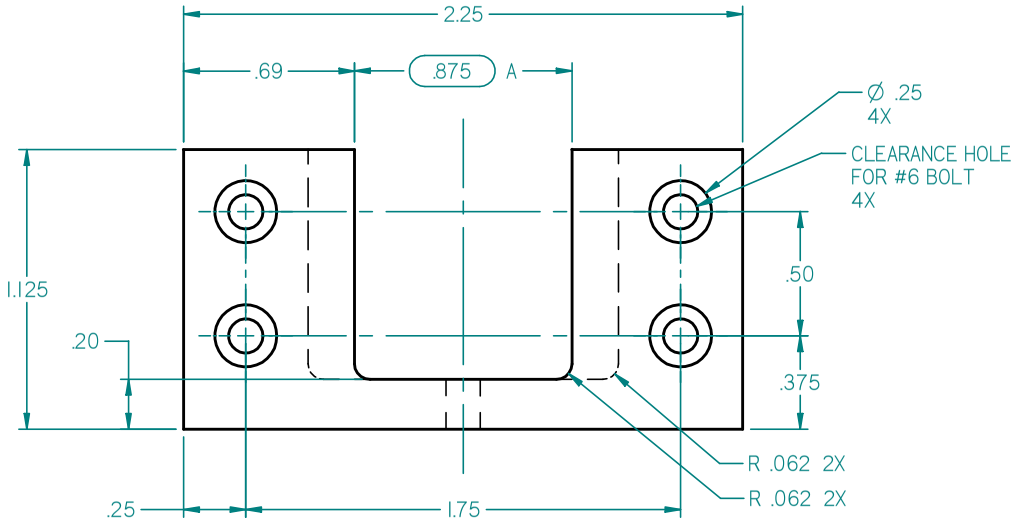

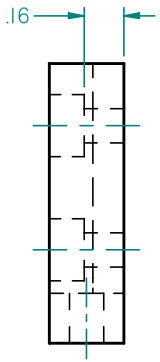

Notes:
1. Material - Aluminum
2. Dimension A must be clearance fit with Dimension A on Movable Hardstop part
3. Dimension B must be interfearnace fit with Dimension B on Movable Harstop part

	NAME	DATE
DRAWN	Brian	11/02/06
CHECKED		
ENG APPR		
MGR APPR		

UNLESS OTHERWISE SPECIFIED
DIMENSIONS ARE IN INCHES
ANGLES ±X.X°
2 PL ±X.XX 3 PL ±X.XXX

SOLID EDGE
UGS - The PLM Company

TITLE: Hardstop Holder

SIZE	DWG NO	REV
B		

FILE NAME: stop_holder.dft

SCALE:	WEIGHT:	SHEET 1 OF 1

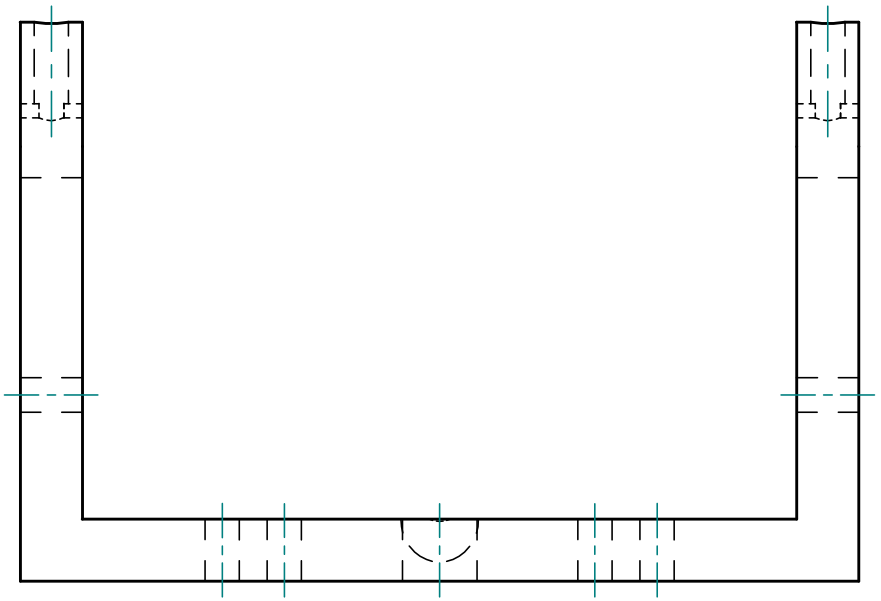

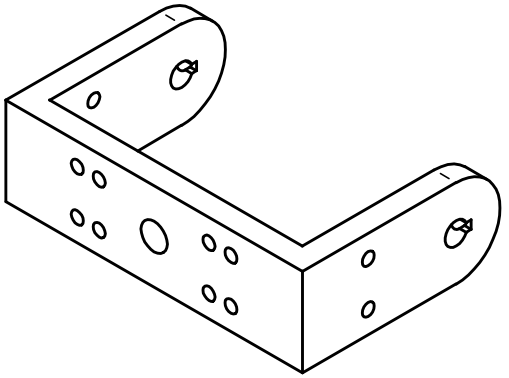

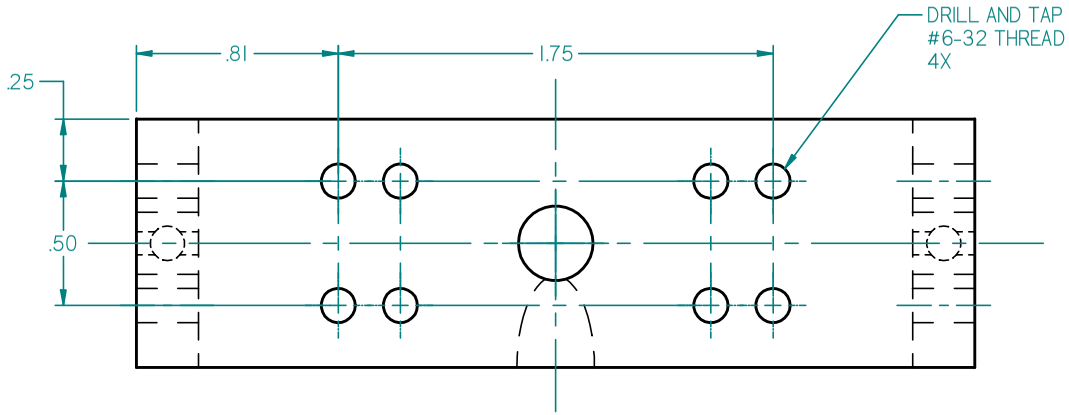

REVISION HISTORY			
REV	DESCRIPTION	DATE	APPROVED

Notes:
1. Holes are modifications to existing part.
2. Only 4 outside holes are new features.

	NAME	DATE
DRAWN	Brian	11/05/06
CHECKED		
ENG APPR		
MGR APPR		

UNLESS OTHERWISE SPECIFIED
DIMENSIONS ARE IN INCHES
ANGLES ±X.X°
2 PL ±X.XX 3 PL ±X.XXX

SOLID EDGE
UGS - The PLM Company

TITLE: Shank Fork Modification

SIZE	DWG NO	REV
B		

FILE NAME: shank_fork_mod.dft

SCALE:	WEIGHT:	SHEET 1 OF 1

REVISION HISTORY			
REV	DESCRIPTION	DATE	APPROVED

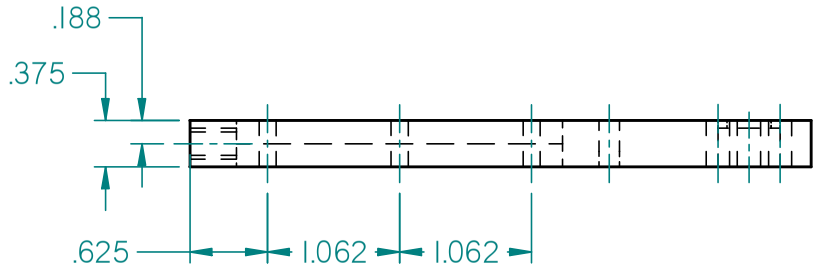

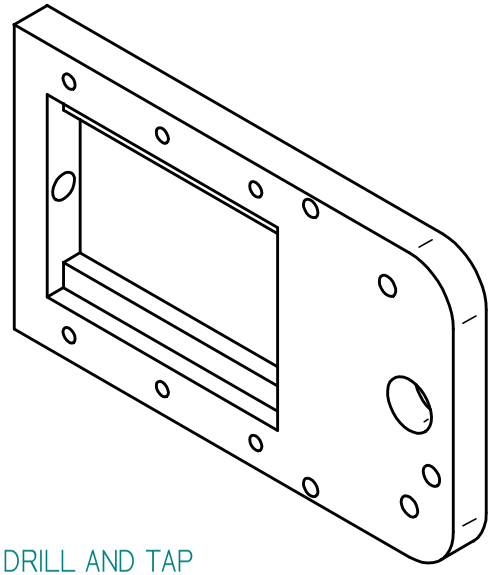

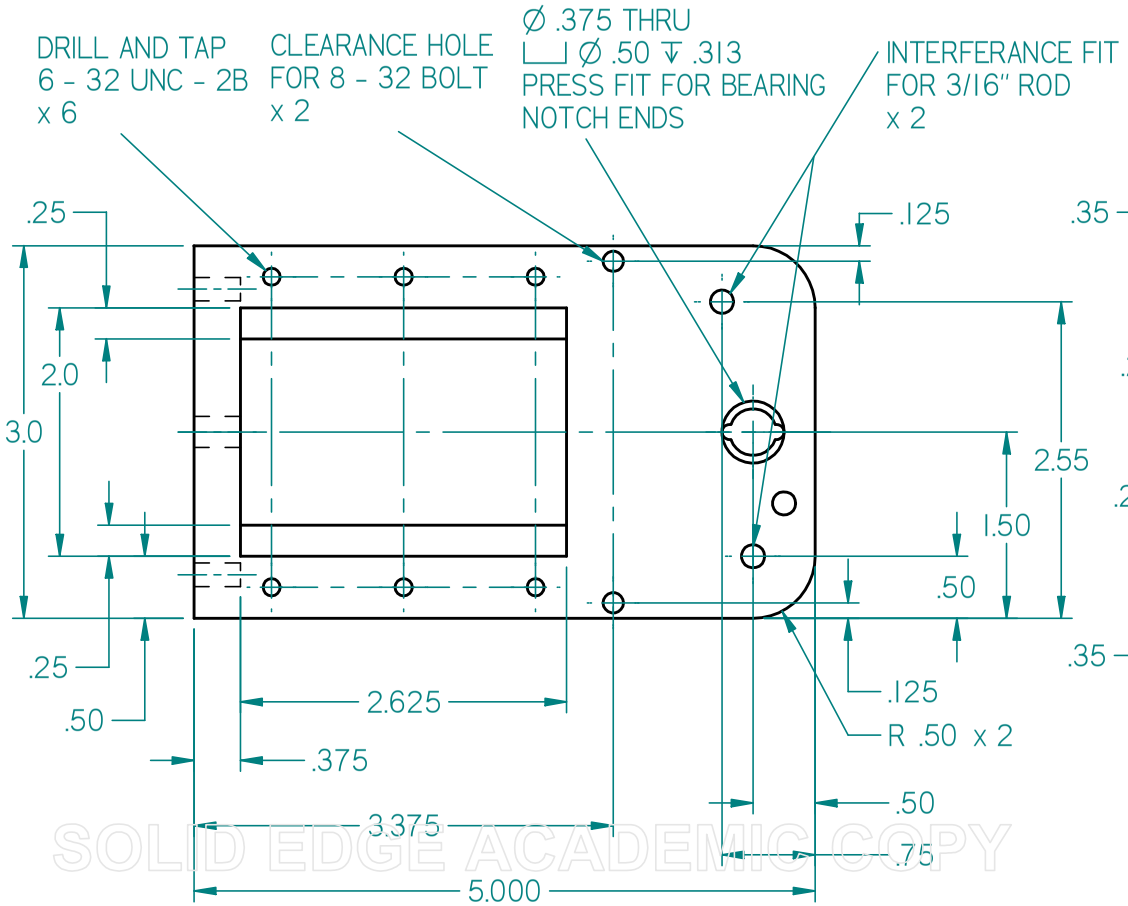

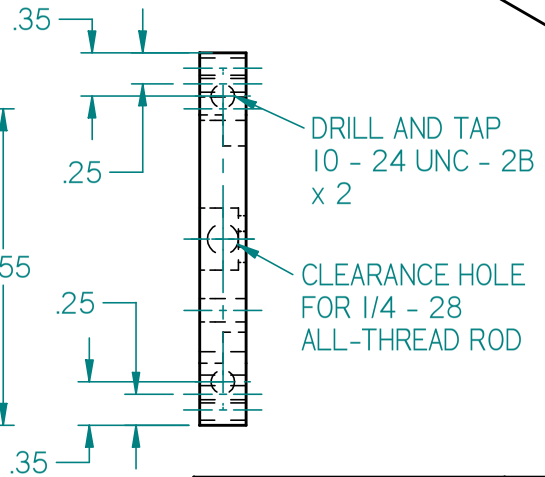

Note:
- Material: Aluminum
- Quantity: 1

	NAME	DATE
DRAWN	Brian	09/26/06
CHECKED		
ENG APPR		
MGR APPR		

UNLESS OTHERWISE SPECIFIED
DIMENSIONS ARE IN INCHES
ANGLES ±X.X°
2 PL ±X.XX 3 PL ±X.XXX

SOLID EDGE
UGS - The PLM Company

TITLE: KNEE SIDE PLATE

SIZE	DWG NO	REV
B		

FILE NAME: knee_plate.dft

SCALE:	WEIGHT:	SHEET 1 OF 1

REVISION HISTORY			
REV	DESCRIPTION	DATE	APPROVED

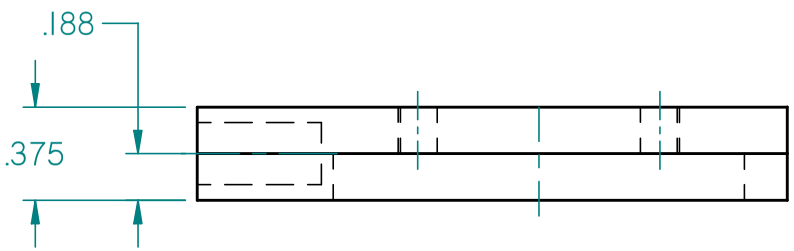

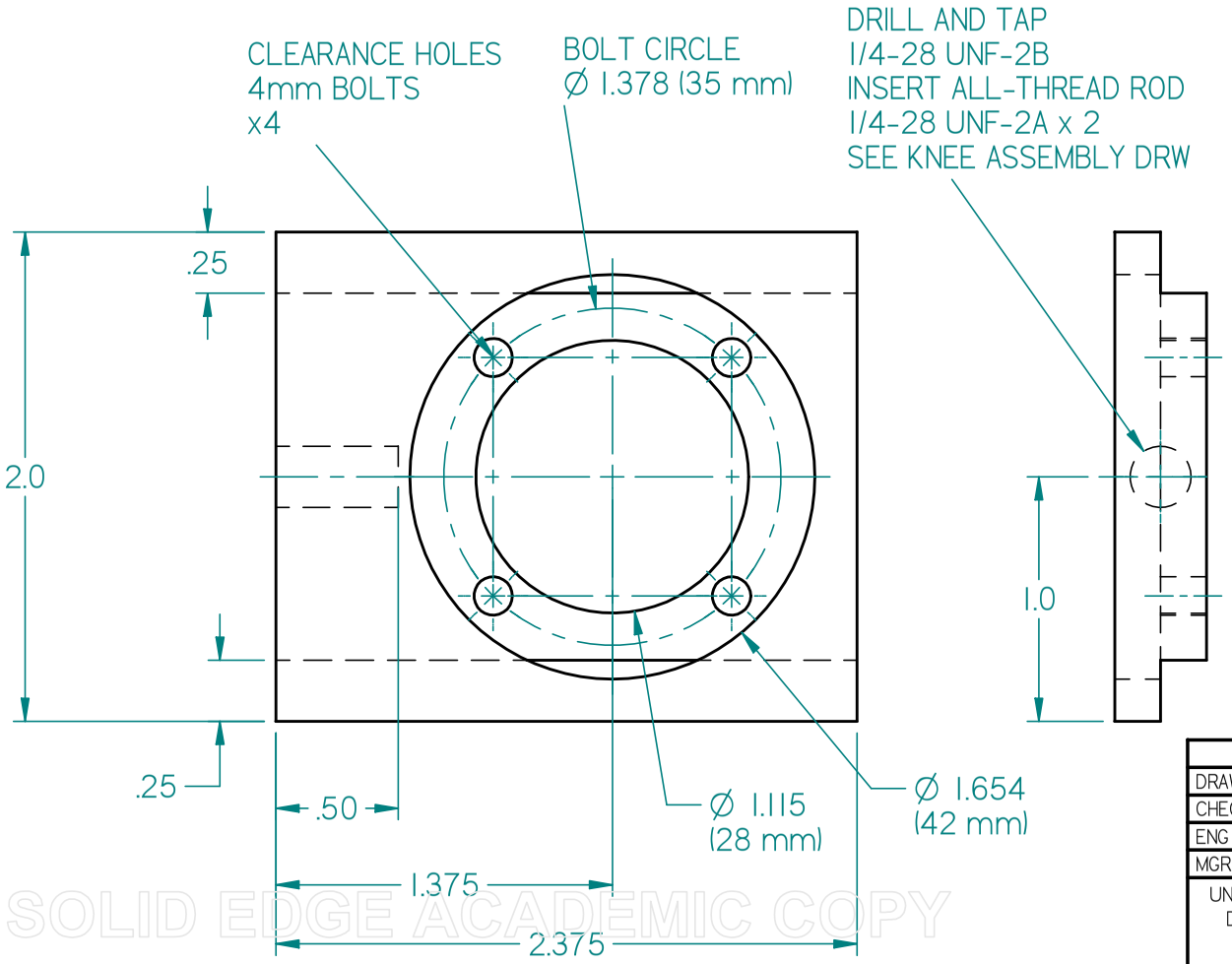

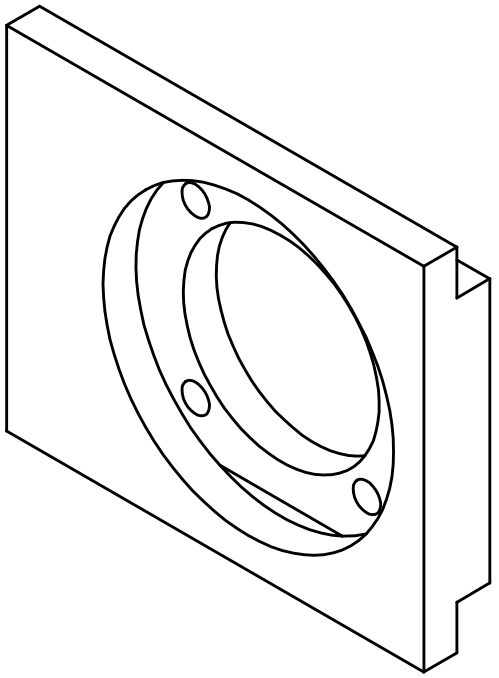

Note:
- Material: Aluminum
- Quantity: 1

	NAME	DATE
DRAWN	Brian	09/26/06
CHECKED		
ENG APPR		
MGR APPR		

UNLESS OTHERWISE SPECIFIED
DIMENSIONS ARE IN INCHES
ANGLES ±X.X°
2 PL ±X.XX 3 PL ±X.XXX

SOLID EDGE
UGS - The PLM Company

TITLE
KNEE TENSIONER PLATE

SIZE	DWG NO	REV
B		

FILE NAME: knee_tensioner.dft

SCALE:	WEIGHT:	SHEET 1 OF 1

REVISION HISTORY			
REV	DESCRIPTION	DATE	APPROVED

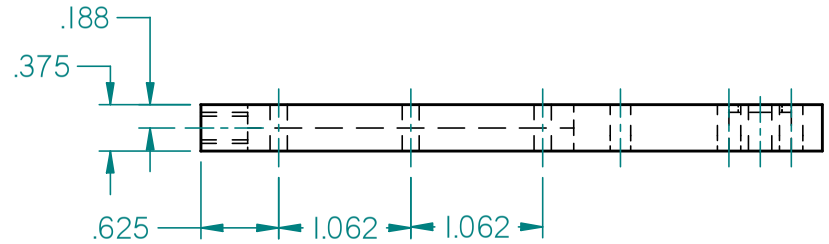

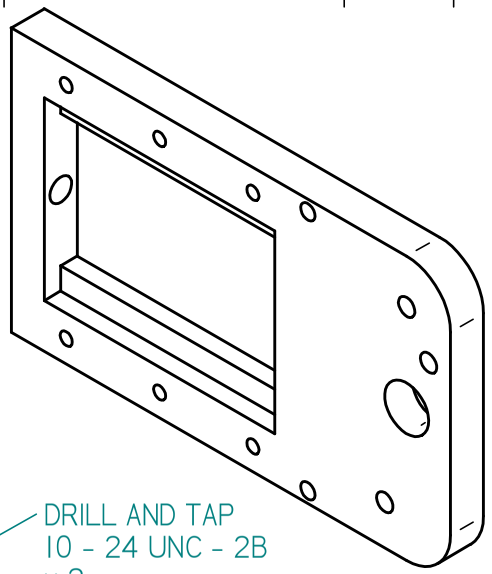

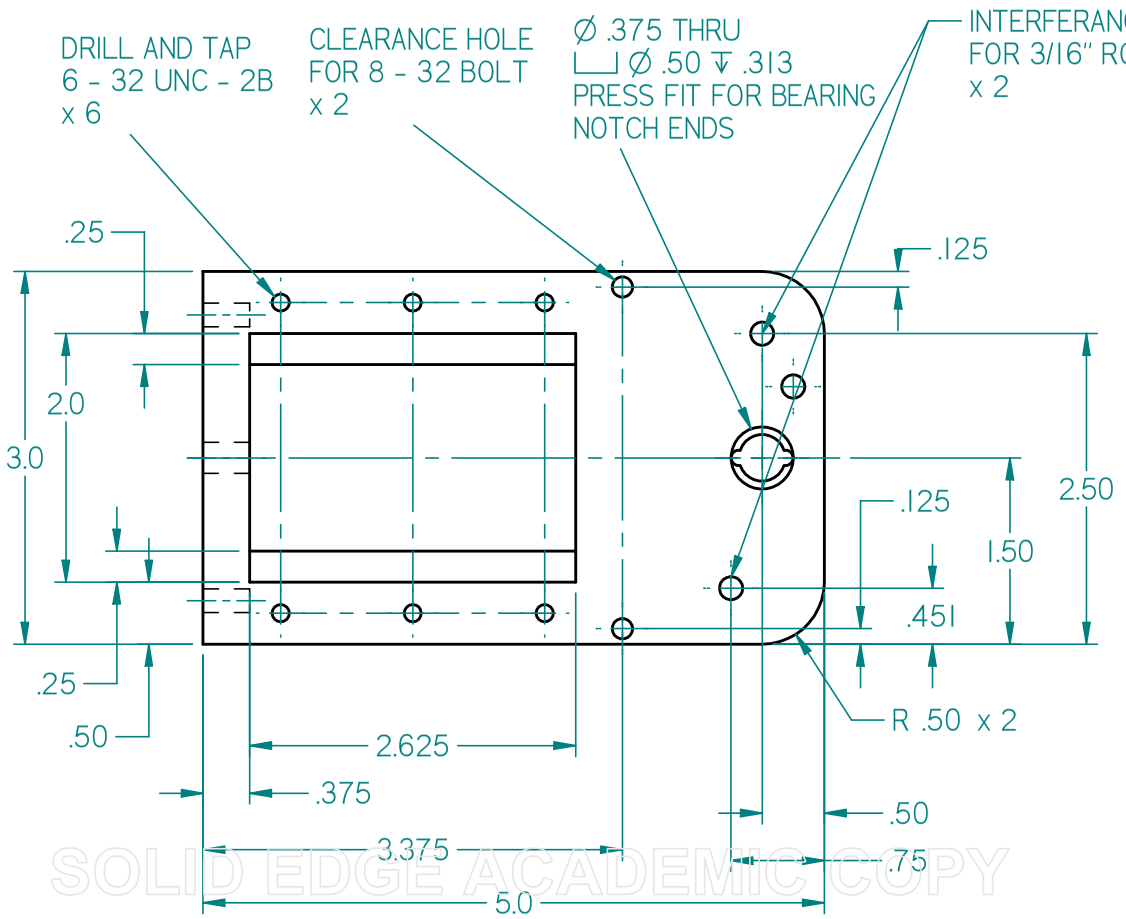

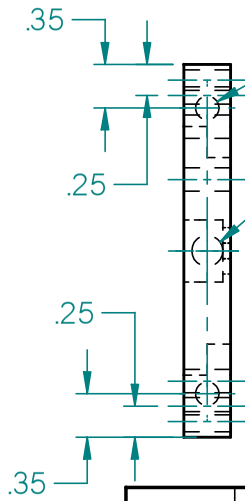

NOTE:
- Material: Aluminum
- Quantity: 1

	NAME	DATE
DRAWN	Brian	09/26/06
CHECKED		
ENG APPR		
MGR APPR		

UNLESS OTHERWISE SPECIFIED
DIMENSIONS ARE IN INCHES
ANGLES ±X.X°
2 PL ±X.XX 3 PL ±X.XXX

SOLID EDGE
UGS - The PLM Company

TITLE: THIGH SIDE PLATE

SIZE	DWG NO	REV
B		

FILE NAME: thigh_plate.dft

SCALE:	WEIGHT:	SHEET 1 OF 1

REVISION HISTORY			
REV	DESCRIPTION	DATE	APPROVED

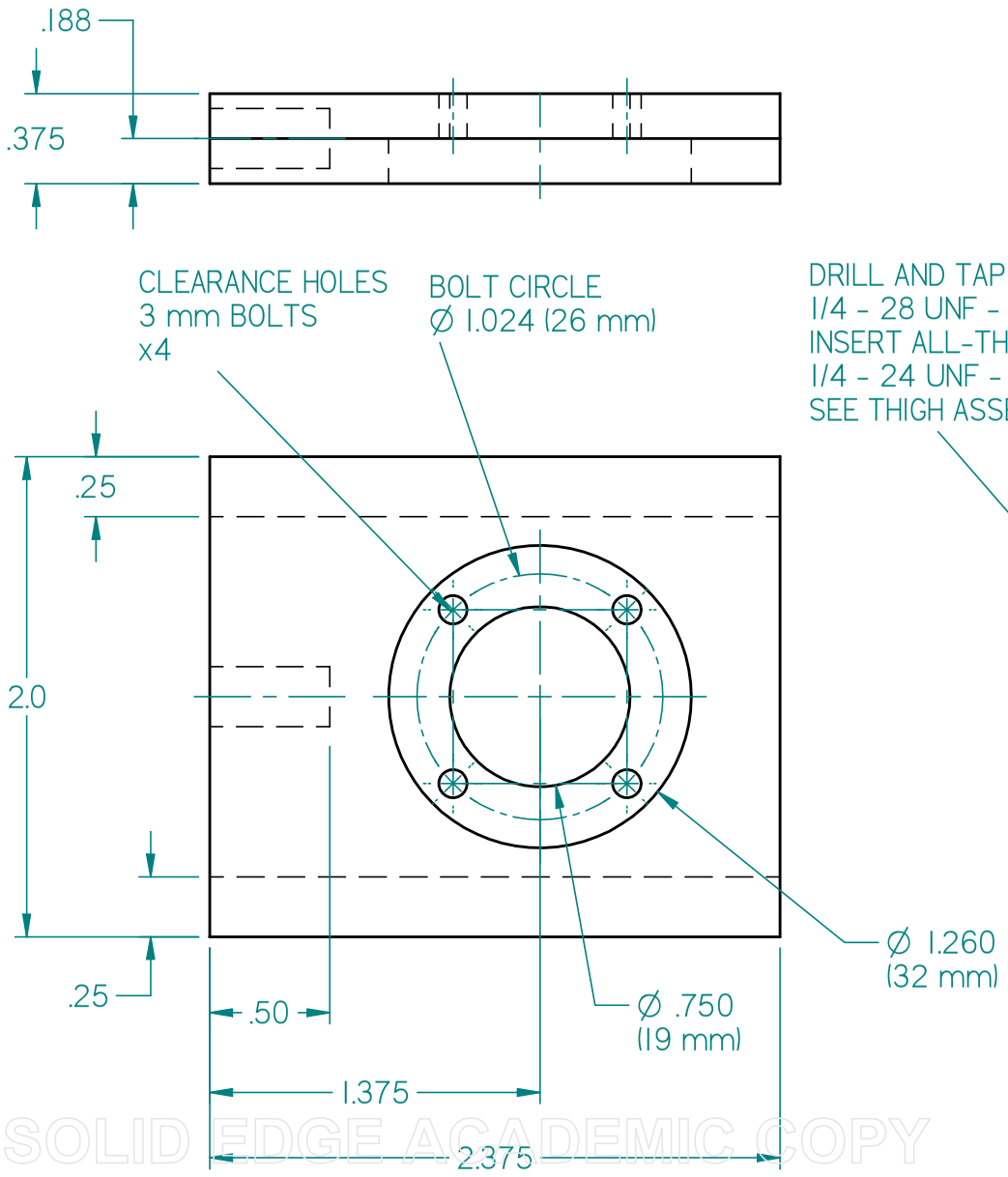

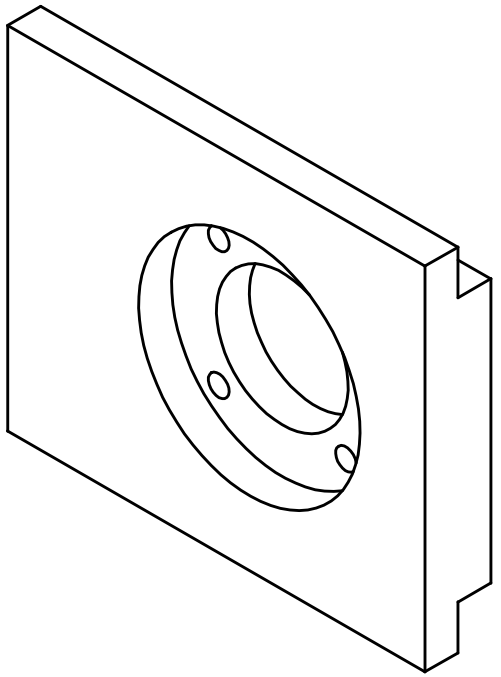

Note:
- Material: Aluminum
- Quantity: 1

	NAME	DATE
DRAWN	Brian	09/26/06
CHECKED		
ENG APPR		
MGR APPR		

UNLESS OTHERWISE SPECIFIED
DIMENSIONS ARE IN INCHES
ANGLES ±X.X°
2 PL ±X.XX 3 PL ±X.XXX

SOLID EDGE
UGS - The PLM Company

TITLE: THIGH TENSIONER PLATE

SIZE	DWG NO	REV
B		

FILE NAME: thigh_tensioner.dft

SCALE:	WEIGHT:	SHEET 1 OF 1

REVISION HISTORY			
REV	DESCRIPTION	DATE	APPROVED

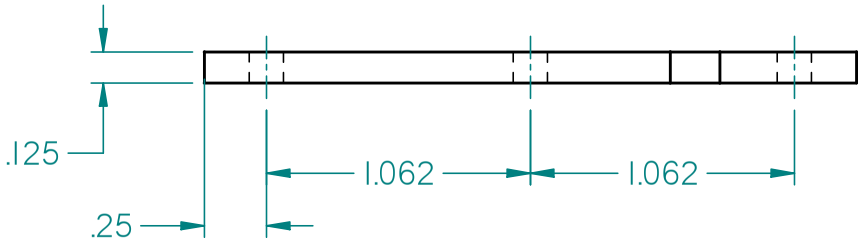

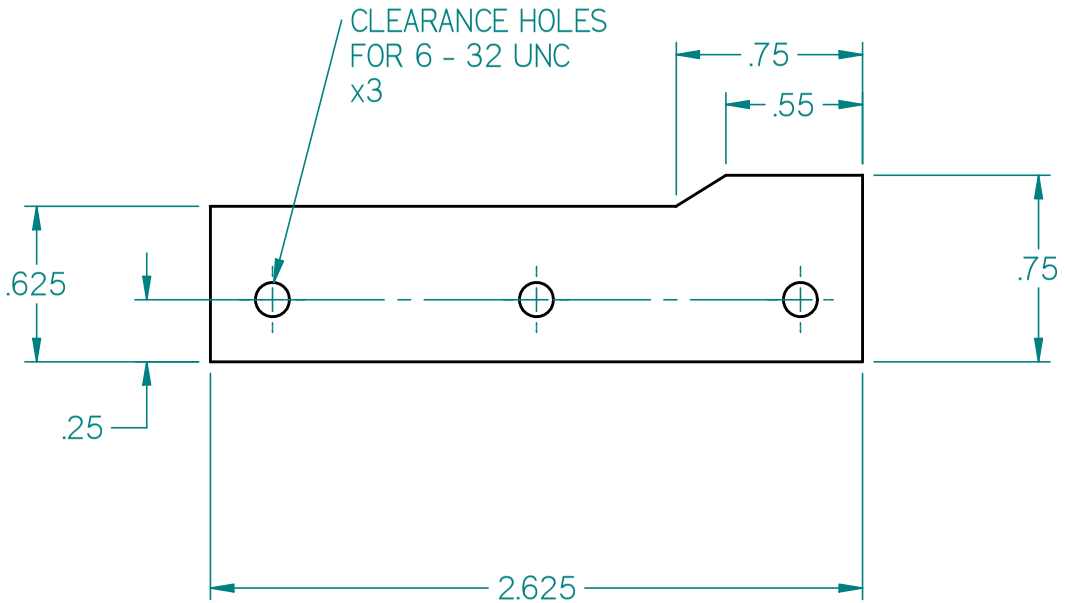

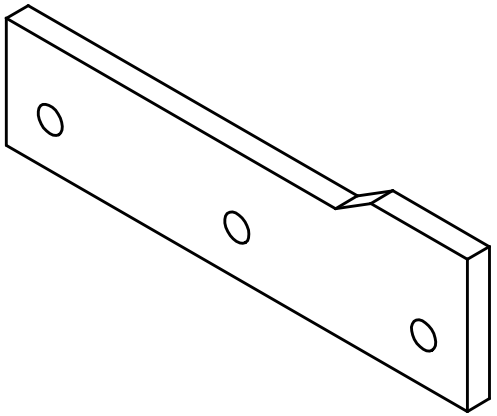

Note::
- Material: Aluminum
- Quantity: 4

	NAME	DATE
DRAWN	Brian	09/26/06
CHECKED		
ENG APPR		
MGR APPR		

UNLESS OTHERWISE SPECIFIED
DIMENSIONS ARE IN INCHES
ANGLES ±X.X°
2 PL ±X.XX 3 PL ±X.XXX

SOLID EDGE
UGS - The PLM Company

TITLE: Clamping Plate

SIZE	DWG NO	REV
B		

FILE NAME: rail.dft

SCALE:	WEIGHT:	SHEET 1 OF 1

REVISION HISTORY			
REV	DESCRIPTION	DATE	APPROVED

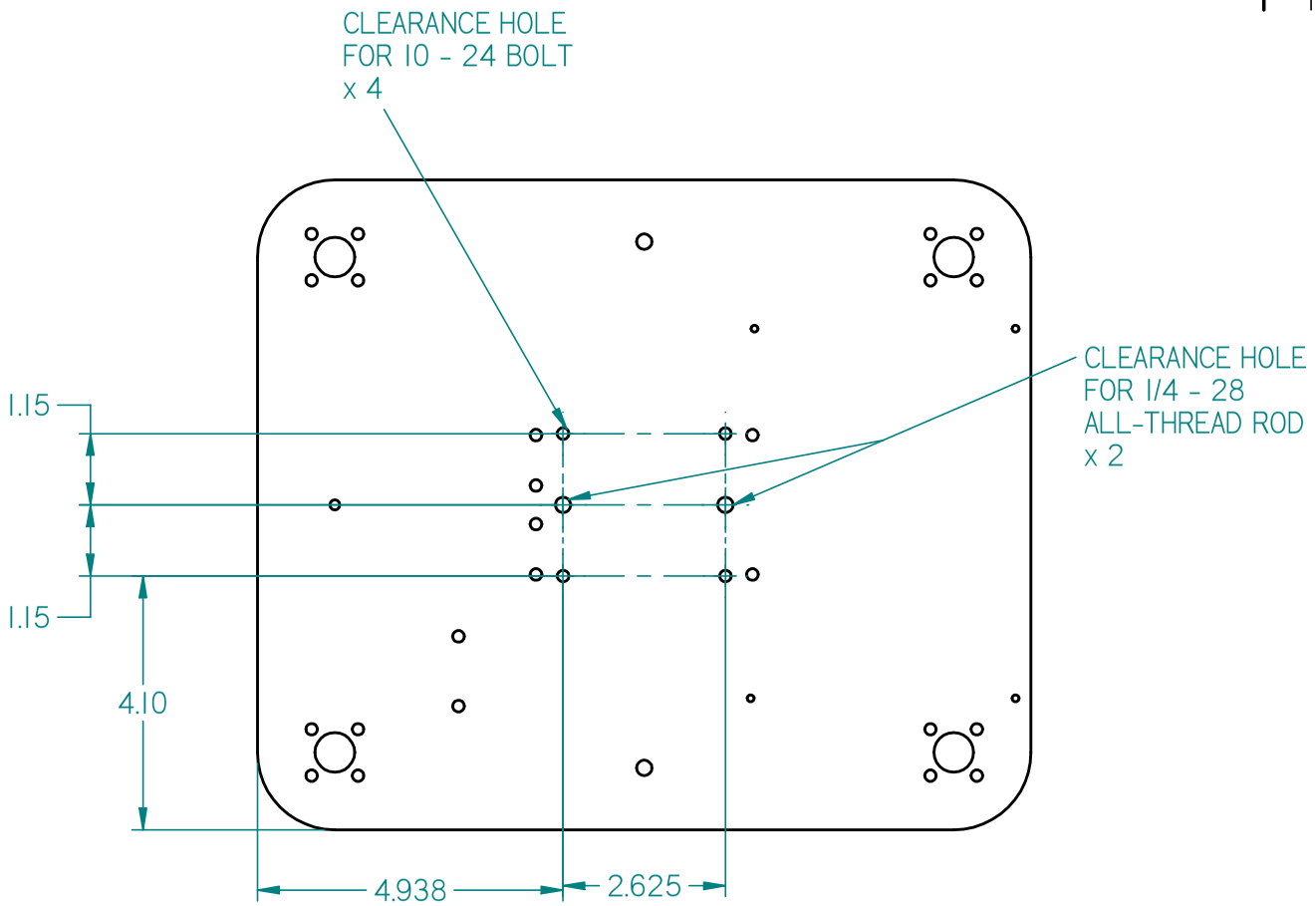

Note:
- Machine from Existing Part

	NAME	DATE
DRAWN	Brian	09/26/06
CHECKED		
ENG APPR		
MGR APPR		

UNLESS OTHERWISE SPECIFIED
DIMENSIONS ARE IN INCHES
ANGLES ±X.X°
2 PL ±X.XX 3 PL ±X.XXX

SOLID EDGE
UGS - The PLM Company

TITLE: MOVING PLATE

SIZE	DWG NO	REV
B		

FILE NAME: moving_plate.dft

SCALE:	WEIGHT:	SHEET 1 OF 1

REVISION HISTORY			
REV	DESCRIPTION	DATE	APPROVED

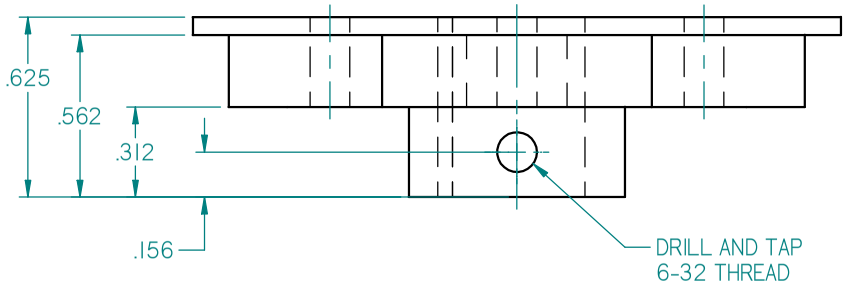

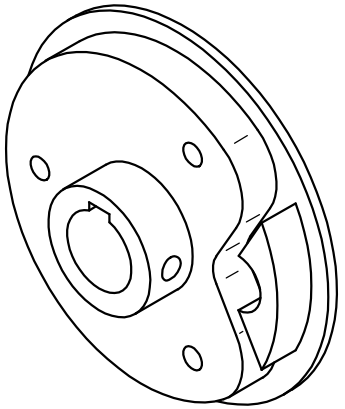

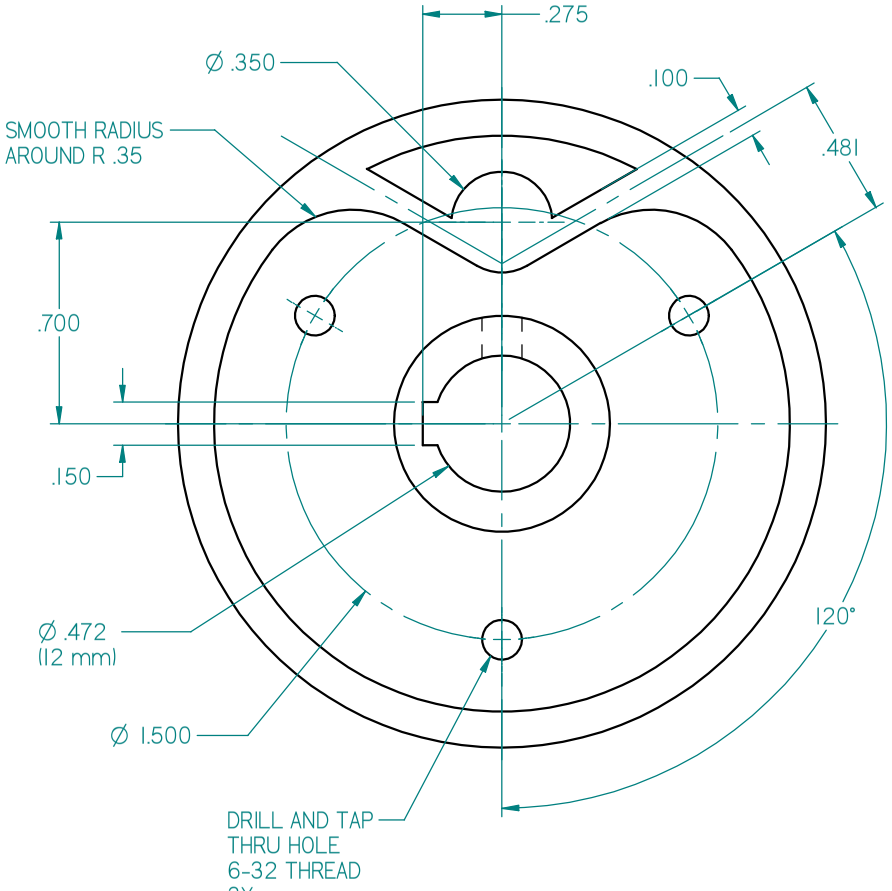

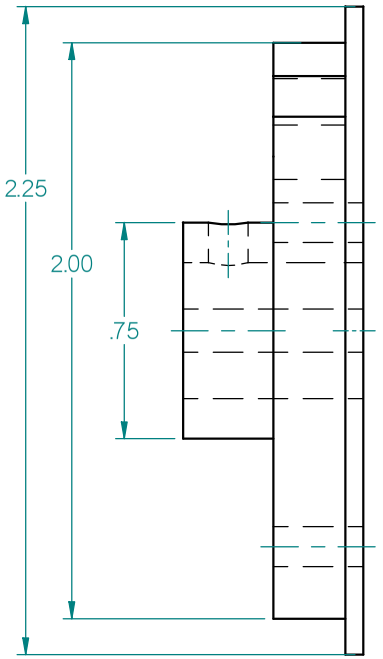

NOTES:
1) MATERIAL: ALUMINUM

	NAME	DATE
DRAWN	Brian	03/15/07
CHECKED		
ENG APPR		
MGR APPR		

UNLESS OTHERWISE SPECIFIED
DIMENSIONS ARE IN INCHES
ANGLES ±X.X°
2 PL ±X.XX 3 PL ±X.XXX

SOLID EDGE
UGS - The PLM Company

TITLE: KNEE MOTOR PULLEY

SIZE	DWG NO	REV
C		

FILE NAME: knee_motor_pulley_new.dft

SCALE:	WEIGHT:	SHEET 1 OF 1

REVISION HISTORY			
REV	DESCRIPTION	DATE	APPROVED

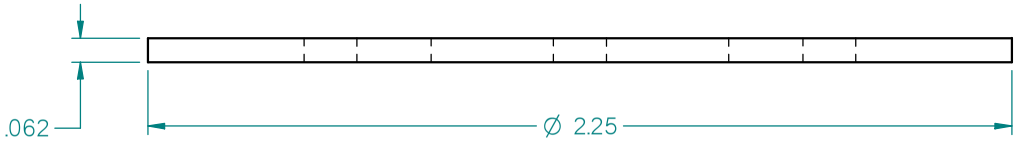

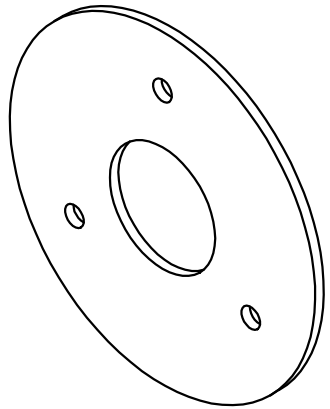

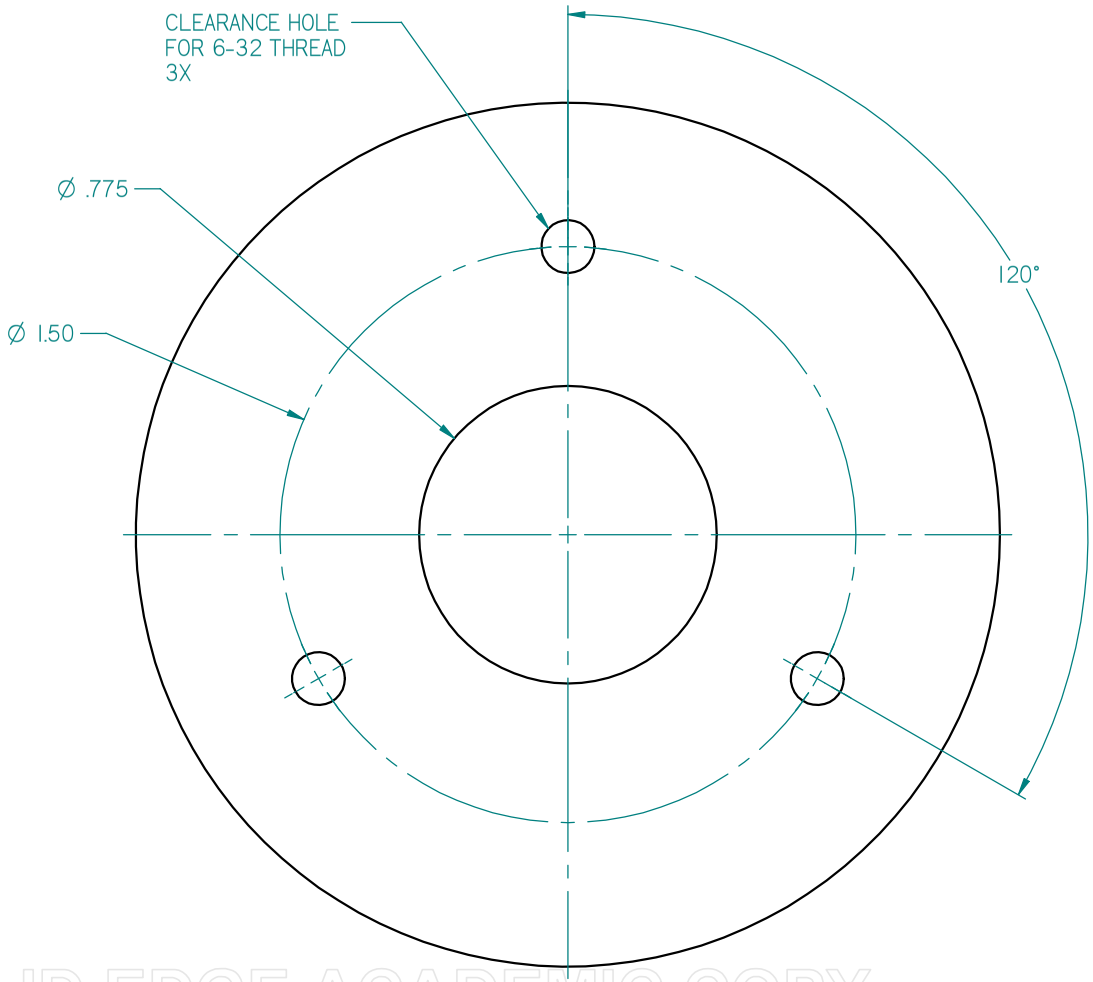

NOTES:
1) MATERIAL: ALUMINUM

	NAME	DATE
DRAWN	Brian	03/15/07
CHECKED		
ENG APPR		
MGR APPR		

UNLESS OTHERWISE SPECIFIED
DIMENSIONS ARE IN INCHES
ANGLES ±X.X°
2 PL ±X.XX 3 PL ±X.XXX

SOLID EDGE
UGS - The PLM Company

TITLE: KNEE MOTOR PULLEY COVER

SIZE	DWG NO	REV
C		

FILE NAME: knee_motor_pulley_cover.dft

SCALE:	WEIGHT:	SHEET 1 OF 1

APPENDIX B

MATLAB CODE FOR ANALYTICAL JUMPING MODEL

Table B.1: List of MATLAB Code Files

Name	Page
List of Variables Used in Analytical Code	101
Foot Offset Loop Code (Sim_loop.m)	103
Analytical Jumping Model (LegAnyl.m)	105
Dynamic Simulation (LegSim1.m)	109
Simulation Inverse Kinematics Function (InverseKinematics.m)	114
Simulation Current Limit Function (currentlimits.m)	115

Table B.2: List of Model Variables by Order of Appearance

Parameter	Thesis Variable	MATLAB Variable
Hip Angle	θ_h	hip_angle
Knee Angle	θ_k	knee_angle
Thigh Length	r_2	l_t
Shank Length	r_3	l_s
Foot Position X	x	X
Foot Position Y	y	Y
Jacobian	J	J
Max Hip Motor Torque	τ_{sat}	T_hmax
Max Knee Motor Torque	τ_{sat}	T_kmax
Hip Motor Current	I_m	hip_current
Knee Motor Current	I_m	knee_current
Hip Motor Torque Constant	k_T	hip_TC
Knee Motor Torque Constant	k_T	knee_TC
Hip Gear Box Ratio	n_g	hip_GR
Knee Gear Box Ratio	n_g	knee_GR
Hip Gear Box Efficiency	e_g	hip_GB_E
Knee Gear Box Efficiency	e_g	knee_GB_E
Virtual Leg Length	l_v	leg_length
Initial Leg Length	l_i	L_i
Takeoff Leg Length	l_t	takeoff_l
Hip Cutoff Leg Length	l_c	Lh_i
Knee Cutoff Leg Length	l_c	Lk_i
Hip Saturated Percentage	n_c	L_THsat
Knee Saturated Percentage	n_c	L_TKsat
Max Hip Joint Torque	τ_{max}	Th_i
Max Knee Joint Torque	τ_{max}	Tk_i
Body Mass	m_b	m_b
Thigh Mass	m_t	m_t
Shank Mass	m_s	m_s
Thigh CM Location	l_{ct}	lg_t
Shank CM Location	l_{cs}	lg_s
Actual Hip Joint Torque	τ_{act}	Tg_hmax
Actual Knee Joint Torque	τ_{act}	Tg_kmax
Horizontal Foot Force	F_x	H_sat
Vertical Foot Force	F_y	V_sat
Normalized Jacobian	$\hat{J}$	J_hat
Eigenvalues	D	D
Eigenvectors	V	V
Ellipse x-axis length	a	a
Ellipse y-axis length	b	b

Ellipse Orientation Angle	ϕ	e_angle
P Relative X Coordinate	P_X	x
P Relative Y Coordinate	P_Y	y
P Absolute x Coordinate	P_x	tan_coord
P Absolute y Coordinate	P_y	tan_coord
Ellipse Horizontal Foot Force	F_{xm}	H_force
Ellipse Vertical Foot Force	F_{ym}	V_force
Ellipse Hip Torque	τ_{hm}	T_hip
Ellipse Knee Torque	τ_{km}	T_knee
VOF Ratio	K_T	T_rat
VOF Horizontal Foot Force	F_x	H_rat
VOF Vertical Foot Force	F_y	V_rat
VOF Hip Torque	τ_{hr}	Th_rat
VOF Knee Torque	τ_{kr}	Tk_rat
Ellipse Max Energy	E_{max}	E_vert
Ellipse Act Energy	E_{act}	E_takeoff
Ellipse Max Height	y_{max}	h_jump_MEA
Saturated Torque Max Energy	E_{max}	E_vert_sat
Saturated Torque Act Energy	E_{act}	E_takeoff_sat
Saturated Torque Max Height	y_{max}	h_jump_sat
VOF Max Energy	E_{max}	E_vert_vfo
VOF Act Energy	E_{act}	E_takeoff_vfo
VOF Max Height	y_{max}	h_jump_vfo
Initial Starting Height	y_i	y_hip_IC
Foot Position Range	x	x_foot
Initial Knee Angle	θ_i	knee_min_angle

```
%Foot Offset Loop
%Runs Analytical Code and Dynamic Simulation for a range of foot positions

clear
clc

x_foot = -.1:.01:.1; %Foot Position Range
knee_min_angle=50;
L_link = 0.1397;

Thigh_Current = -7.5; %Hip motor current for simulation
Knee_Current = 10; %Knee motor current for simulation
hip_sat = .95; %Hip motor saturation %
knee_sat = .80; %Knee motor saturation %

for x_loop = 1:length(x_foot)

    if x_foot(x_loop) < -L_link + L_link * cos(knee_min_angle*pi/180)
        y_hip_IC(x_loop) = sqrt(L_link^2 - (L_link + x_foot(x_loop))^2)+.002;
    elseif x_foot(x_loop) > L_link - L_link * cos(knee_min_angle*pi/180)
        y_hip_IC(x_loop) = sqrt(L_link ^2 - (L_link - x_foot(x_loop))^2) + .002;
    else
        l_e2 = L_link^2 + L_link^2 - 2*L_link*L_link*cos(knee_min_angle*pi/180);
        y_hip_IC(x_loop) = sqrt(l_e2 - x_foot(x_loop)^2) + .002;
    end
    y_hip_IC(x_loop) = 0.13;


    %Run Simulation
    FP = [x_foot(x_loop) y_hip_IC(x_loop) Thigh_Current Knee_Current];
    [h_sim(x_loop), y_takeoff, TO_vel(x_loop), TO_force(x_loop)] = LegSim1(FP);
    takeoff_LL(x_loop) = sqrt(x_foot(x_loop)^2 + y_takeoff^2);

    %Run Analytical Code
    [h_sat(x_loop), h_MEA(x_loop), h_vfo(x_loop), h_sat_S] = LegAnyl(x_foot(x_loop), y_hi ↙
p_IC(x_loop), hip_sat, knee_sat);

    done = x_loop/length(x_foot)
end

clc
LL_AVG = mean(takeoff_LL);
LL_RNG = [max(takeoff_LL), min(takeoff_LL)];
LL_PER = abs(LL_RNG-LL_AVG)./LL_AVG.*100;
LL_STD = std(takeoff_LL)./LL_AVG.*100;

F_AVG = mean(TO_force);
F_RNG = [max(TO_force), min(TO_force)];
F_PER = abs(F_RNG-F_AVG)./F_AVG.*100;
F_STD = std(TO_force)./F_AVG.*100;

V_AVG = mean(TO_vel);
V_RNG = [max(TO_vel), min(TO_vel)];
V_PER = abs(V_RNG-V_AVG)./V_AVG.*100;
V_STD = std(TO_vel)./V_AVG.*100;

results = [LL_AVG F_AVG V_AVG; LL_PER(1) F_PER(1) V_PER(1); LL_PER(2) F_PER(2) V_PER(2);  ↙
LL_STD F_STD V_STD]
```

```
%Find normalized error between simulation and analytical code
h_sim_N = h_sim./max(h_sim);
h_sat_N = h_sat./max(h_sat);
error = (h_sim_N-h_sat_N)./h_sim_N;


figure(1)
subplot(1,2,1)
plot(x_foot, h_sat,'b-','linewidth',2)
hold on
plot(x_foot, h_sim,'r--','linewidth',2)
xlabel('Foot Position x (m)')
ylabel('Jumping Height y_m_a_x (m)')
legend('Model', 'Simulation')

subplot(1,2,2)
plot(x_foot, h_sim_N,'r--','linewidth',2)
hold on
plot(x_foot, h_sat_N,'b-','linewidth',2)
xlabel('Foot Position x (m)')
ylabel('Jumping Height y_m_a_x (m)')
axis([-.1,.1,.6,1.05])
```

```
function [h_jump_sat, h_jump_MEA, h_jump_vfo, KA_deg] = LegAnyl(x_foot, y_hip, hip_motor_ ↙
sat, knee_motor_sat)

%Analytical Jumping Loop Code

%%%%%%%%%%SYSTEM PARAMETERS%%%%%%%%%%%%%%
%Length, Mass, Inertia Parameters
l_t = .1397; %Thigh Length
lg_t = .07148; %Thigh CG Length
m_t = .328; %Thigh Mass
Izz_t = .0011432; %Thigh CG Inertia

l_s = .1397; %Shank Length
lg_s = .03029; %Shank CG Length
m_s = .431; %Shank Mass
Izz_s = .00092924; %Shank CG Inertia

m_b = 3.26; %Body Mass
g = 9.81; %Gravity Acceleration
rail_friction = 0; %Rail Friction Force
takeoff_l = .274; %Takeoff Leg Length


%Motor Parameters
hip_current = 7.5; %Hip Motor Current
hip_TC = 0.04; %Hip Motor Torque Constant
hip_GR = 33; %Hip Gearbox Gear Ratio
hip_GB_E = 0.75; %Hip Gearbox Efficiency
T_hmax = hip_current*hip_TC*hip_GR*hip_GB_E; %Max Hip Motor Torque
L_THsat = hip_motor_sat; %Hip Torque Saturation Percentage

knee_current = 10; %Knee Motor Current
knee_TC = 0.043; %Knee Motor Torque Constant
knee_GR = 66; %Knee Gearbox Gear Ratio
knee_GB_E = .72; %Knee Gearbox Efficiency
T_kmax = knee_current*knee_TC*knee_GR*knee_GB_E; %Max Knee Motor Torque
L_TKsat = knee_motor_sat; %Knee Torque Saturation Percentage

n=0;m=0;nm=0;mn=0;
X = x_foot;
Y_i = -y_hip;

% Jumping Motion Loop - Loop for specific foot position

% Jumping Loop Parameters
    dY = 0.001; %Jumping Loop Step Size
    max_Y = -sqrt((takeoff_l)^2-X^2); %Takeoff Body Height
    Y = Y_i:-dY:max_Y;

    %Create Torque-Leg Length Curves For Specific Foot Position
    L_i = sqrt(Y_i^2 + X^2);
    Lk_i = (takeoff_l - L_i)*L_TKsat + L_i;
    Lh_i = (takeoff_l - L_i)*L_THsat + L_i;

    Lh = [Lh_i, takeoff_l];
    Th = [T_hmax, 0];
    Hh = polyfit(Lh, Th, 1);
```

```
    Lk = [Lk_i, takeoff_l];
    Tk = [T_kmax, 0];
    Hk = polyfit(Lk, Tk, 1);

    for i = 1:length(Y)

        leg_length(i) = sqrt(Y(i).^2 + X.^2);

        %Inverse Kinematics (Determination of Leg Angles)
        A = -2*X*l_t;
        B = -2*Y(i)*l_t;
        C = X^2+l_t^2+Y(i)^2-l_s^2;
        t = (-B+sqrt(B^2-C^2+A^2))/(C-A);
        hip_angle = 2*atan2((-B+sqrt(B^2-C^2+A^2)),(C-A));
        Y_knee = l_t*sin(hip_angle);
        X_knee = l_t*cos(hip_angle);
        knee_angle = atan2((Y(i)-Y_knee),(X-X_knee));
        KA_deg(i) = knee_angle*180/pi;
        HA_deg(i) = hip_angle*180/pi;
        theta1 = 5*pi/2 - hip_angle;
        theta2 = hip_angle - knee_angle;

        %Torque Limits (w/ Gravity)
        if leg_length(i) <= Lh_i
            Th_i(i) = T_hmax;
        else
            Th_i(i) = polyval(Hh, leg_length(i));
        end
        if leg_length(i) <= Lk_i
            Tk_i(i) = T_kmax;
        else
            Tk_i(i) = polyval(Hk, leg_length(i));
        end
        Tgh = (m_t*lg_t*cos(hip_angle)+m_s*(l_t*cos(hip_angle)+lg_s*cos(knee_angle)))*g;
        Tgk = m_s*lg_s*cos(knee_angle)*g;
        %Tg_hmax = T_hmax - Tgh;
        %Tg_kmax = T_kmax - Tgk;
        Tg_hmax = Th_i(i) - Tgh; %TLL Curve
        Tg_kmax = Tk_i(i) - Tgk; %TLL Curve
        T_limit = [1/Tg_hmax 0; 0 1/Tg_kmax];

        %Inertia Matrix, Used only with Dynamic Manipulability
        theta_2 = hip_angle - knee_angle;
        M11(i) = Izz_t + Izz_s + m_t*(lg_t^2) + m_s*(l_t^2+lg_s^2 + 2*l_t*lg_s*cos(theta_ ↙
2));
        M12(i) = Izz_s + m_s*(lg_s^2+l_t*lg_s*cos(theta_2));
        M21(i) = M12(i);
        M22(i) = Izz_s + m_s*lg_s^2;
        M = [M11(i) M12(i); M21(i) M22(i)];

        %Jacobian Matrix J(theta)
        J = [-l_t*sin(hip_angle), -l_s*sin(knee_angle); l_t*cos(hip_angle), l_s*cos(knee_ ↙
angle)];
        J_hat = (T_limit*J')';
        [V,D] = eig((J_hat*J_hat')^-1); %Uncomment for Manipulability
        %[V,D] = eig((J_hat * ((M'*M)^-1) *J_hat')^-1); %Uncomment for Dynamic Manipulabi ↙
lity
```

```
        %Determination of Horizontal Tangent Points for the Force Ellipse
        a = sqrt(D(1,1));
        b = sqrt(D(2,2));
        e_angle = atan(V(2,1)/V(1,1));
        y = (b^2)/(sqrt(a^2*tan(e_angle)^2+b^2));
        x = (a^2*tan(e_angle))/(sqrt(a^2*tan(e_angle)^2+b^2));
        tan_coord = [cos(e_angle) -sin(e_angle); sin(e_angle) cos(e_angle)]*[x;y]+[X;Y(i) ↙
];
        max_FA = atan((tan_coord(2,1)-Y(i))/(tan_coord(1,1)-X));
        max_FA_deg(i) = max_FA*180/pi;
        max_V_force(i) = tan_coord(2,1)-Y(i);
        max_H_force(i) = tan_coord(1,1)-X;


        %Determination of Torque Curves for Manipulability Ellipse
        F_foot = [max_H_force(i); max_V_force(i)];
        T = J_hat' * F_foot;
        check(i) = sqrt(T(1,1)^2 + T(2,1)^2);
        T_actual = J'*F_foot;
        T_hip(i) = T_actual(1,:) + Tgh; %MEA Hip Torque
        T_knee(i) = T_actual(2,:) + Tgk; %MEA Knee Torque
        V_force(i) = max_V_force(i);%MEA Vertical Force
        H_force(i) = max_H_force(i); %MEA Horizontal Force

        %Maximum Torque Forces
        T_sat = [Tg_hmax; -Tg_kmax];
        F_sat = ((J')^-1)*T_sat;
        V_sat(i) = F_sat(2,1); %SAT Vertical Force
        H_sat(i) = F_sat(1,1); %SAT Horizontal Force

        %Vertical Force Only Analysis (Fx = 0)
        T_rat(i) = J(2,1)/J(2,2);
        Tk_rat(i) = -Tg_kmax;
        if knee_angle > 3*pi/2
            Tk_rat(i) = Tg_kmax;
        end
        Th_rat(i) = Tk_rat(i) *T_rat(i);
        if abs(Th_rat(i)) > abs(Tg_hmax)
            if Th_rat(i) > 0
                Th_rat(i) = Tg_hmax;
            else
                Th_rat(i) = -Tg_hmax;
            end
            Tk_rat(i) = Th_rat(i)/T_rat(i);
        end
        Tt_rat = [Th_rat(i); Tk_rat(i)];
        F_rat = ((J')^-1)*Tt_rat;
        V_rat(i) = F_rat(2,1); %VOF Vertical Force
        H_rat(i) = F_rat(1,1); %VOF Horizontal Force (should be = 0)
    end

    % Calculate the Energy Input into the leg during power stroke
    % and the maximum height achieved

    %MEA Torque Energy
    E_vert = trapz(-Y(1:i), V_force(1:i));
    E_takeoff = E_vert - ((m_b)*g + rail_friction)*(Y_i-Y(i));
    h_flight = E_takeoff/((m_t+m_s+m_b)*g+rail_friction);
```

```
    h_jump_MEA = h_flight-Y(i);

    %Saturated Torque Energy
    E_vert_sat = trapz(-Y(1:i), V_sat(1:i));
    E_takeoff_sat = E_vert_sat - ((m_b)*g + rail_friction)*(Y_i-Y(i));
    h_flight_sat = E_takeoff_sat/((m_t+m_s+m_b)*g + rail_friction);
    h_jump_sat = h_flight_sat-Y(i);

    %Vertical Only Force Energy
    E_vert_vfo = trapz(-Y(1:i), V_rat(1:i));
    E_takeoff_vfo = E_vert_vfo - ((m_b)*g + rail_friction)*(Y_i-Y(i));
    h_flight_vfo = E_takeoff_vfo/((m_t+m_s+m_b)*g+rail_friction);
    h_jump_vfo = h_flight_vfo-Y(i);
```

```
function [h, y, to_v, to_f] = LegSim1(FP)
%FP = [Foot-x Plate-y Thigh_Current(-7.5 7.7) Knee_Current(-10 10)]

%Jumping Dynamic Simulation

close all;

int_step = 1E-04;
max_time = 1;  %SIMULATION TIME

%series elastic actuation for articulated leg,
%torsional spring and damper, and a motor in
%series with the spring.
%Body params

%P = PLATE
%T = THIGH
%S = SHANK

g = 9.81;
mp = 3.25992;
mt = 0.328;
ms = 0.431;

L = 0.1397;
lh = 0.0108;
Kinematic_Params = [L L lh];

Ks=16.54; bs=0;%0.01;           %knee spring and damper
backDrvEff=0.65;
%Amplifier params
current_control = 1;
maxVoltage = 48.0;
V = maxVoltage;
%hip motor model params
%EC32, GP32C
Ra_t=4.44;          %Armature resistance (low val: no-load spd/cur, hig val:phase-to-phas ↙
e)
k_tau_t=0.04;               %torque constant
k_b_t=k_tau_t;              %back-emf constant
B_tm=5.1e-06;               %Total motor-side damping
T_f_t = 0.0;                %Friction torque

%Current limits (hip limited < 10A, by powersupply. Knee +10A)
Imax_t=7.5;                 %max current limit for amplifier
Imin_t=-7.5;                %min current limit for amplifier
%Get gearbox specs
n_tm = 33.0;                  %Gear ratio
eta_f_t = 0.70;             %Gear box forward efficiency
eta_r_t = 0.60;             %Gear box reverse efficiency NEED TO IMPLEMENT
J_tm = 2.0e-6;             %total motor/gearbox inertia

%knee motor model params
%EC40/GP42C
Ra_km=1.21;%1.69;           %Armature resistance  (low val: no-load spd/cur, hig val:phas ↙
e-to-phase)
k_tau_km=0.043;                 %torque constant
k_b_km=k_tau_km;                %back-emf constant
```

```
B_km=8.6e-06;                %Total motor-side damping
T_f_s=0.0;                   %Friction torque
n_km=66.0;                   %Gear ratio
%Current limits
Imax_km=10.0;                %max current limit for amplifier
Imin_km=-10.0;               %min current limit for amplifier
%Get knee gearbox specs
eta_f_k = 0.72;              %Gear box forward efficiency
eta_b_k = 0.65;              %Gear box reverse efficiency
J_km=9.4400e-006;       %Total motor-side inertia for knee

% Y = FOOT POSITION
% Z = PLATE HEIGHT

%--------------------------------------------------------------------------
%--------------------------------------------------------------------------
x = FP(1);
y = FP(2);
m_amps = [FP(3) FP(4)];
ia_t = m_amps(1);
ia_km = m_amps(2);
%--------------------------------------------------------------------------
%--------------------------------------------------------------------------
xic = x;
yic = y;
qic = InverseKinematics(x, y, Kinematic_Params);

%setup initial values for state variables
theta_t = qic(2);
theta_tic = theta_t;
theta_s = qic(2)+qic(3);
theta_sic = theta_s;
theta_km = (qic(2)+qic(3))*n_km; %initially coincident with shank angle
theta_kmic = theta_km;
theta_kmdot = 0;
alpha = (cos(theta_s)/(L*sin(theta_s-theta_t)));
beta = -(cos(theta_t)/(L*sin(theta_s-theta_t)));
beta_ic = beta;
alpha_ic = alpha;
y = y;
y_dot = 0;
theta_tdot = (y_dot*alpha);
theta_sdot = (y_dot*beta);

%FLAGS
stop_sim = 0;
sim_t = 0;
i = 1;
jumptime = 0;
qjump = [0 0];
flag1 = 0;
flag2 = 0;
flag3 = 0;
flag4 = 0;
mgforce = 0;
temptime1 = 0;
y_dotdot = -0.00001;
h = 0;
```

```
% [a,b] = size(FP_min);
% for w = 1:b
%     if ((FP(w) < FP_min(w))||(FP(w) > FP_max(w)))
%         stop_sim = 1;
%     end
% end

while (((i*int_step) <= max_time) && (stop_sim~=1))
    if (~flag1 && y_dotdot > 0)
        flag1 = 1;
        sim_t;
    end
    if ((flag1 && ~flag2) && y_dotdot <= -g)
        flag2 = 1;
        sim_t;
    end

    if (~flag1 || ~flag2)
        %Linear and Non-linear terms for calculating vertical accel (y_dotdot)
        alpha = (cos(theta_s)/(L*sin(theta_s-theta_t)));
        beta = -(cos(theta_t)/(L*sin(theta_s-theta_t)));
        tempj = beta^-1;
        theta_tdot = (y_dot*alpha);
        theta_sdot = (y_dot*beta);
        tau_s = Ks*(theta_km/n_km - theta_s) - bs*(theta_kmdot/n_km - theta_sdot);

        ia_t = currentlimits(maxVoltage, Imax_t, Imin_t, Ra_t, k_b_t, m_amps(1), theta_td ↙
ot*n_tm);
        tau_t = eta_f_t*n_tm*(k_tau_t*ia_t-n_tm*B_tm*theta_tdot-n_tm*J_tm*(y_dotdot*alpha ↙
-cos(theta_t-theta_s)/sin(theta_t-theta_s)*theta_tdot^2-theta_sdot^2/sin(theta_t-theta_s) ↙
));
        if(tau_t * theta_tdot < 0)
            eta_f_t = eta_r_t;
            ia_t = currentlimits(maxVoltage, Imax_t, Imin_t, Ra_t, k_b_t, m_amps(1), thet ↙
a_tdot*n_tm);
        else
            eta_f_t = 0.70;
        end

        term1 = eta_f_t*alpha*n_tm*k_tau_t*ia_t;
        term2 = eta_f_t*alpha*n_tm^2*B_tm*theta_tdot;
        term3 = (eta_f_t*alpha*n_tm^2*J_tm*cos(theta_s-theta_t)*theta_tdot^2)/(sin(theta_ ↙
s-theta_t));
        term4 = (eta_f_t*alpha*n_tm^2*J_tm*theta_sdot^2)/(sin(theta_s-theta_t));
        term5 = beta*tau_s;
        term6 = (mp+mt+ms)*g;
        num = term1 - term2 - term3 - term4 + term5 - term6;
        term7 = (mp+mt+ms);
        term8 = alpha^2*n_tm^2*J_tm*eta_f_t;
        den = term7 + term8;
        y_dotdot = num / den;

        ia_km = currentlimits(maxVoltage, Imax_km, Imin_km, Ra_km, k_b_km, m_amps(2), the ↙
ta_kmdot);
        if(sign(ia_km) ~= sign(theta_kmdot))
            eta_k = eta_b_k;
        else
```

```
            eta_k = eta_f_k;
        end
        km_term1 = (k_tau_km/J_km)*ia_km;
        km_term2 = -B_km/J_km*theta_kmdot;
        km_term3 = -(tau_s/(n_km*J_km*eta_k));
        km_term4 = 0;
        km_term5 = 0;
        km_term6 = 0;

        theta_kmdotdot = km_term1 + km_term2 + km_term3;
        km_tau = eta_k*n_km*(k_tau_km*ia_km-B_km*theta_kmdot-J_km*theta_kmdotdot);

        y = y_dot * int_step + y;
        y_dot = y_dotdot * int_step + y_dot;

        theta_km = theta_kmdot * int_step + theta_km;
        theta_kmdot = theta_kmdotdot * int_step + theta_kmdot;

        q = InverseKinematics(x, y, Kinematic_Params);
        theta_t = q(2);
        theta_s = q(2)+q(3);
        %Data Collection

        theta_spr = theta_km/n_km - theta_s;
        qy(i) = y;
        qy_dot(i) = y_dot;
        qtheta_s(i) = theta_s;
        qtheta_t(i) = theta_t;
        qtheta_km(i) = theta_km;
        qtheta_kmdot(i) = theta_kmdot;
        qia_t(i) = ia_t;
        qia_km(i) = ia_km;
        qtau_s(i) = tau_s;
        qkm_tau(i) = km_tau; %next state...fix
        qtau_t(i) = tau_t;
        qtheta_tdot(i) = theta_tdot;
        qtheta_spr(i) = theta_spr;
        b_h(i) = y;
        b_v(i) = y_dot;
        b_a(i) = y_dotdot;
        time(i) = i*int_step;
        Fx(i) = (-sin(theta_s)/(L*sin(theta_s-theta_t)))*tau_t+(sin(theta_t)/(L*sin(theta ↙
_s-theta_t)))*tau_s;
        Fy(i) = alpha*tau_t + beta*tau_s;

        i = i + 1;
        sim_t = sim_t + int_step;

    else
        theta_s_max = max(abs(qtheta_spr));
        KE_smax = .5*Ks*(theta_s_max^2);
        KE_sTO = .5*Ks*(theta_s_max^2 - theta_spr^2);

        KE = sign(y_dot)*.5*(mp+ms+mt)*y_dot^2;
        h = (KE/((mp+ms+mt)*g)+y);
        stop_sim = 1;
    end
end
```

```
to_v = max(b_v);
to_f = max(Fy);
```

```
function [q_out]=InverseKinematics(x, z, kinematic_params)
%Returns the generalized coordinate's (joint angles and displacement)
%cooresponding to the initial conditions of foot position and plate
%position.

    ls = kinematic_params(1);
    lt = kinematic_params(2);
    lh = kinematic_params(3);
    r = 0; %radius of curvature of foot (not needed)
    t_2p = 0;
    t_2n = 0;

    temp1 = (x^2+(z-r)^2-lt^2-ls^2)/(2*ls*lt);

    if ((1-temp1^2) > 0)
        t_2p = atan2(sqrt(1-temp1^2),temp1);
        t_2n = -atan2(sqrt(1-temp1^2),temp1);
    end

    if (t_2p > 0 && t_2p < pi)
        theta_k = t_2p;
        t_2 = t_2p;
    else
        theta_k = t_2n;
        t_2 = t_2n;
    end

    %find hip angle
    aprime = z-r;
    bprime = x;
    cprime = ls*sin(t_2);
    dprime = ls*cos(t_2)+lt;
    t_1 = 0.0;

    t_1 = atan2(aprime*dprime-bprime*cprime, aprime*cprime+bprime*dprime);

    theta_h = t_1 - pi/2;

    q_out = [-(lt+ls-z) -theta_h -theta_k];
```

```
%Simon Curran

function current = currentlimits(maxVoltage, I_max, I_min, Ra, k_b, u, theta_m_dot)
%function returns the actual motor current for the motor with the
%associated parameters, Ra, k_b, Imax, Imin, and maxVoltage.
%calculations and procedure flow are outlined in the thesis

currentCtrl = 1;  %flag, not sure if I'm going to use this
%apply knee motor current limits
if currentCtrl
    i_a = u;
    u_c=i_a*Ra+k_b*theta_m_dot;
    maxVolt=abs(maxVoltage);
    recalcFlag=0;
    if ((sign(u) == 1) && (u_c >= maxVolt))
        u_c = maxVolt;
        recalcFlag=1;
    elseif ((sign(u) == -1)&&(u_c <= -maxVolt));
        u_c = -maxVolt;
        recalcFlag=1;
    end

    if recalcFlag
        i_a=(sign(u)*maxVolt-k_b*theta_m_dot)/Ra;
%         if ((i_a <= 0) && (sign(u) == 1))
%             i_a = 0;
%         elseif ((i_a >= 0) && (sign(u) == -1))
%             i_a = 0;
%         end
    end

end

if i_a >= I_max
   i_a = I_max;
elseif i_a <= I_min
   i_a=I_min;
end
recalcFlag = 0;
current = i_a;
```

BIBLIOGRAPHY

[1] M. H. Raibert, *Legged Robots that Balance.* MIT Press, Cambridge, 1986.

[2] M. J. French, *Invention and Evolution: Design in Nature and Engineering.* Cambridge University Press, Cambridge, 1988.

[3] A. Spiessbach, B. M. Gothard, D. G. Morgenthaler, K. J. Waldron, R. S. Price, J. E. Bares, W. H. Chun, F. L. Garrett, and B. Stout. *Final report for Mars Rover Sample Return (MRSR) rover mobility and surface rendezvous studies.* Technical report, Martin Marietta Space Systems Company, Denver, 1989.

[4] S. Hirose and K. Kato. "Study on quadruped walking robot in Tokyo Institute of Technology: Past, present, and future," in *Proceedings of the IEEE International Conference on Robotics and Automation*, pages 414–419, Piscataway, NJ, 2000. IEEE.

[5] Y. Sakagami, R. Watanabe, C. Aoyama, S. Matsunaga, N. Higaki, and K. Fujimura. "The intelligent ASIMO: system overview and integration," in *Proceedings of the IEEE/RSJ International Conference on Intelligent Robots and Systems,* pages 2478–2483, Lausanne, Switzerland, 2002. IEEE.

[6] K. Nagasaka, Y. Kuroki, S. Suzuki, Y. Itoh, and J. Yamaguchi. "Integrated motion control for walking, jumping and running on a small bipedal entertainment robot," in *Proceedings of the IEEE International Conference on Robotics and Automation*, pages 3189-3194, New Orleans, LA, 2004. IEEE.

[7] D. P. Krasny, *Evolving Dynamic Maneuvers in a Quadruped Robot*. Ph.D. dissertation, The Ohio State University, Columbus, Ohio, 2005.

[8] E. Lucas, *Huitieme Recreation - La Machine a Marcher.* Recreat, Math. 4, 1894, pages 198-204.

[9] A. A. Frank. *Automatic Control Systems for Legged Locomotion.* Technical Report USCEE Report No. 273, University of Southern California, Los Angeles, 1968.

[10] R. B. McGhee. "Finite state control of quadruped locomotion," in *Proceedings of the Second International Symposium on External Control of Human Extremities*, Dubrovnik, Yugoslavia, 1966.

[11] I. Kato and H. Tsuiki. "The hydraulically powered biped walking machine with a high carrying capacity," in *Proceedings of the Fourth International Symposium on External Control of Human Extremities* Dubrovnik,Yugoslavia, pages 410–421, 1972.

[12] A. Takanishi, M. Ishida, Y. Yamazaki, and I. Kato. “The realization of dynamic walking by the biped walking robot WL-10RD,” in *Proceedings of the International Conference on Advanced Robotics*, pages 459–466, 1985.

[13] J. Furusho and A. Sano. “Sensor-based control of a nine-link biped.” *International Journal of Robotics Research*, 9(2):83–98, 1990.

[14] F. Yamasaki, T. Matsui, T. Miyashita, and H. Kitano. “Pino the humanoid: a basic architecture.” *RoboCup 2000*, pages 269–278, 2001.

[15] K. Matsuoka. “A mechanical model of repetitive hopping movements”. *Biomechanisms*, 5: 251-58, 1980.

[16] H. Miura and I. Shimoyama. “Dynamic walk of a biped.” *International Journal of Robotics Research*, 3(2):60–74, 1984.

[17] J.E. Pratt, M.C. Chee, A. Torres, P. Dilworth, and G.A. Pratt. “Virtual model control: an intuitive approach for bipedal locomotion.” *International Journal of Robotics Research*, 20(2):129–143, 2001.

[18] C. Chevallereau, E.R. Westervelt, and J.W. Grizzle. “Asymptotically stable running for a five-link, fouractuator, planar bipedal robot.” *International Journal of Robotics Research* (to appear).

[19] J. Remic, *Prototype Leg Design for a Quadruped Robot Application*. Masters thesis, The Ohio State University, Columbus, Ohio, 2005.

[20] *LOCTITE Hysol 9460 Datasheet.* Technical Data Sheet, Henkel Loctite Americas, Inc., December 2006.

[21] K. J. Waldron and G. L. Kinzel, *Kinematics, Dynamics, and Design of Machinery.* John Wiley & Sons, Inc., pages 192-193, 2004.

[22] T. Yoshikawa. “Manipulability and Redundancy Control of Robotic Mechanisms,” in *Proceedings of the International Conference on Robotics and Automation*, vol. 2, pages 1004-1009, 1895.

[23] T. Yoshikawa. “Dynamic Manipulability of Robot Manipulators,” in *Proceedings of the International Conference on Robotics and Automation*, vol. 2, pages 1033-1038, 1895.